PhD thesis

Numerical Simulation of Sediment Transport at the Agulhas Drift on the South African Gateway in relation to its Geodynamic Development

Xin Li

Zusammenfassung

Das Südafrikanische Tor ist eine kritische Region für den Austausch von Wassermassen zwischen dem Atlantischen und dem Indischen Ozean. Die Variabilität dieses Austausches spielt eine wichtige Rolle für das globale Klima.

Während der FS Sonne Ausfahrt SO–182 im Jahr 2005 wurden im Transkei Becken hochauflösende seismische Daten gesammelt, die einen großen, ausgedehnten, hügelförmigen Kontourit zeigen. Es handelt sich dabei um die Agulhas Drift, die durch das östlich fließende Antarktische Bodenwasser (AABW) und das Nordatlantische Tiefenwasser (NADW) seit 3 Mio. Jahren ausgebildet wird.

Zum besseren Verständnis der Einflüsse der verschiedenen Strömungen auf die Sedimenttransportmuster in der Umgebung der Agulhas Drift wurde das Regional Oceanic Modeling System (ROMS) verwendet, um das zu Grunde liegende Strömungssystem und die Sedimenttransportprozesse zu simulieren.

Die Strömungssimulationen zeigen wiederkehrende, einzelne, zyklische Wirbel, die sich als Schlüssel für die hydrodynamischen Ereignisse im gesamten Transkei Becken erwiesen hat. Die Wirbel befinden sich im Zentrum des Transkei Beckens und erstrecken sich über die gesamte Wassersäule. Im nördlichen Segment der Wirbel ist Strömung ostwärts entlang der Südflanke der Agulhas Drift. Er scheint durch Störungen in der Subtropischen Konvergenzzone (STC) im Gebiet südlich von Afrika erzeugt zu werden, wenn sich planetarische Wellen entlang der STC verformen. Diese Störungen erhöhen zunächst die kinetische Energie an der Oberfläche des Wirbels im Transkei Becken. Die hohe kinetische Energie des Wirbels wird dann von der Oberfläche in tiefere Bereiche des Ozeans transferiert,

woraus die Bildung von weiteren Wirbeln in der Tiefe resultiert.

Auf Basis der Strömungssimulationen wurden Korngrößen–Experimente durchgeführt, um das Transportverhalten von 4 verschiedenen Silt–Korngrößenklassen zu untersuchen. Unsere Simulationen zeigen, dass das Sedimenttranportmuster im Transkei Becken stark durch den mesoskaligen Wirbel beeinflusst wird. Während der Wirbelereignisse wird Silt aller getesteten Korngrößenklassen entlang der nordöstlichen Flanke des Algulhas Plateau resuspendiert, wobei jedoch nicht Silt aller Größenklassen weiter in die Region der Agulhas Drift transportiert werden kann. Grober Silt kann nicht über lange Entfernungen transportiert werden und wird in der Umgebung des Resuspensionsgebietes wieder abgelagert. Mittlerer Silt kann nur dann in die Region der Agulhas Drift transportiert werden, wenn die Wirbelströmung stark genug ist. Feiner Silt kann hingegen leicht in die Driftregion befördert werden. Sehr feiner Silt wird sogar über die Agulhas Drift hinaus ins südliche Transkei Becken transportiert.

Abstract

The South African Gateway is a critical region for the water mass exchange between the Atlantic and the Indian Ocean. The variability in the interoceanic exchange is relevant to global climate change.

High resolution seismic reflection data were collected in the Transkei Basin during R/V SONNE cruise SO–182 in 2005. These seismic observations have indicated that a large elongate mounded contourite drift, the Agulhas Drift, has been built up by eastward flows of Antarctic Bottom Water (AABW) and North Atlantic Deep Water (NADW) since about 3 Ma.

For a better understanding of the influences of the various currents on sediment transport patterns in the vicinity of the Agulhas Drift, the Regional Oceanic Modeling System (ROMS) has been used to simulate the current system and suspended sediment transport processes.

The results from current system simulation showed that a recurrent individual cyclonic eddy event is the key hydrodynamic feature in the Transkei Basin. These eddies are almost fixed in the center of the Transkei Basin and spread over the entire water column. Flow in their northern segments is eastward across the southern flank of the Agulhas Drift. These eddies are supposedly the result of perturbations in the Subtropical Convergence (STC) in the region of south of Africa, where planetary waves on the STC deform. The perturbations enhance the surface eddy kinetic energy (EKE) in the Transkei Basin. The high EKE is then transferred from the surface to the deep ocean, where it causes the formation of eddies at abyssal depth.

Based on the ocean circulation simulations, grain size experiments were carried out to test the transport behaviors for 4 different silt grain size classes. Our simulations reveal that sediment transport patterns in the Transkei Basin are strongly influenced by the mesoscale eddies. During eddy events, silts at all tested grain sizes can be resuspended by the AABW along the northeastern flank of the Agulhas Plateau that borders the Transkei Bsin to the east, whereas not all of them can be further transported into the region of the Agulhas Drift. Coarse silt cannot be transported over long distances, but it is deposited in the vicinity of the resuspension area. Medium silt can be transported into this region of the Agulhas Drift, only when the eddy current is strong enough. Fine silt and very fine silt can easily be carried into the drift area. The simulations show that medium and fine silt can be deposited on the Agulhas Drift, whereas very fine silt is further transported out of the area into the southern Transkei Basin.

Contents

1

Introduction

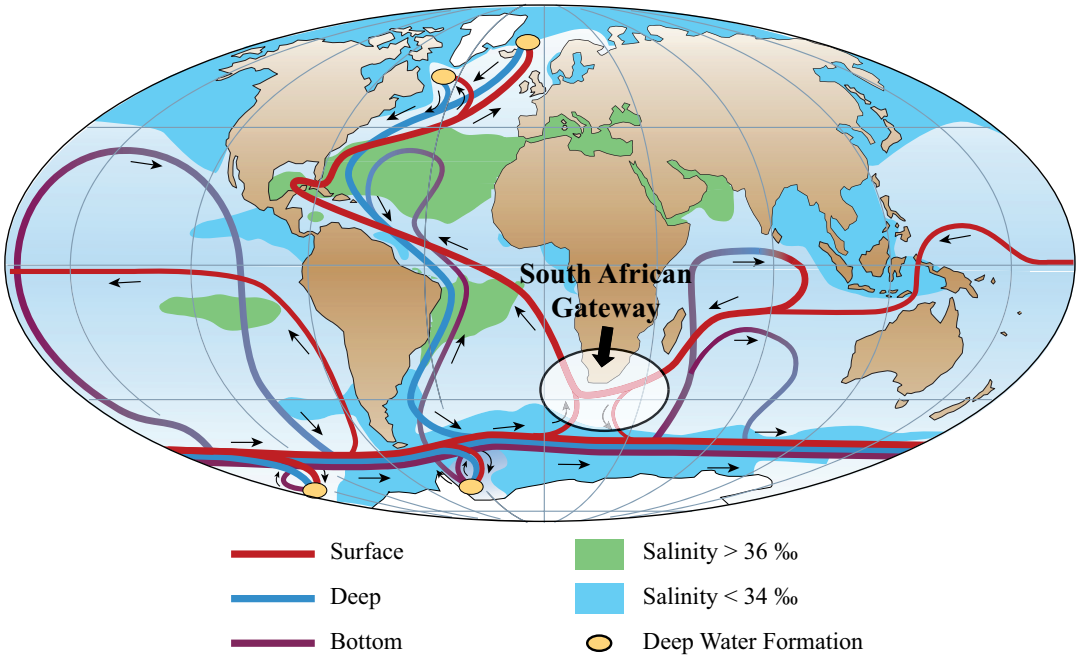

Figure 1.1.: Schematic illustration of the meridional overturning circulation based on the study of *Rahmstorf* (2002)

Meridional Overturning Circulation and Climate Change

Recent global warming and its related prediction of a reduced meridional overturning circulation (MOC) in the future has increased interest in the role of the overturning circulation in climate change. The MOC schematically describes the global scale ocean circulation in horizontal and vertical dimensions (Figure 1.1) (e.g. *Gordon*, 1986; *Bröcker*, 1987; *Gordon*, 1991; *Schmitz*, 1996a,b; *Rahmstorf*, 2002; *Lumpkin and Speer*, 2007; *Richardson*, 2008). The North Atlantic Deep Wa-

ter (NADW) is formed in the North Atlantic. It flows southward from the source regions, across the equator and further extending into the Southern Ocean, Indian Ocean, and Pacific Ocean. On the other side, the Antarctic Bottom Water (AABW) is originated in the Antarctic as part of the deep water. It spreads northward into the Atlantic, Indian and Pacific Oceans. The deep cold water is transformed into warmer upper layer water in the Pacific and Indian Oceans, and returns to the Atlantic around southern Africa. From there, the warm water flows northward in the upper layer back to the North Atlantic (Figure 1.1). This diagram is sometimes also called global ocean conveyor belt or the thermohaline circulation (THC). However, THC only refers to the part of the ocean circulation that is driven by global density gradients created by surface heat and freshwater fluxes (e.g. *Gordon*, 1991; *Richardson*, 2008). The overturning circulation is a complicated system driven by winds, by buoyancy forcing through evaporation, precipitation, heating, and cooling, and by mixing due to winds and tides. The term MOC is therefore better defined and has become more popular in use.

Within the MOC, both heat energy and greenhouse gases are transported by water masses around the globe. Hence, it has significant impact on the climate of the Earth (*Siedler et al.*, 2001). Changes in the ocean circulation and its influences on the climate change have been increasingly reported in different paleo–oceanographic and climatic studies (e.g. *Sarnthein et al.*, 1994; *Webb et al.*, 1997b; *Rahmstorf*, 2002). Moreover, rapid glacial inception associated with abrupt MOC reduction in the future has been simulated in climate models (e.g. *Rahmstorf*, 1995; *Ganopolski et al.*, 2001; *Vellinga and Wood*, 2002; *Drijfhout and Hazeleger*, 2007). For these reasons, further research works on the MOC are essential for the development of a better understanding of climate change.

Critical Region for MOC: South African Gateway

An important region for the meridional overturning circulation is the South African Gateway, which is the unique place for watermass exchange between the

Indian and Atlantic Oceans (Figure 1.1 and 1.2)(*Gordon*, 1986; *de Ruijter et al.*, 1999; *Gordon*, 2003; *Richardson*, 2008). Figure 1.2 provides a detailed illustration of the current system in this region.

At present, in the upper limb of the MOC, warm surface water is transferred from the Indian Ocean to the South Atlantic Ocean via Agulhas Current System. The Agulhas Current originates from recirculation in the southwest Indian Ocean subgyre (*Gordon*, 1985; *Stramma and Lutjeharms*, 1997) and flows along the east coast of Africa affecting the water column to approximately 2000 m depth (*Lutjeharms*, 1996; *Bryden et al.*, 2005; *Lutjeharms*, 2006). Having passed the southern tip of the continental shelf of Africa, the Agulhas Current retroflects and carries its major water mass back to the South Indian Ocean as a meandering jet known as the Agulhas Return Current (*Quartly and Srokosz*, 1993; *Boebel and Barron*, 2003). The Agulhas Retroflection is regularly located near 38 °S, between 15 °E and 20 °E (*Lutjeharms*, 1996). Anomalous upstream retroflection has been observed at about 25 °E by radiometer and drifter data (*Lutjeharms and van Ballegooyen*, 1988) as well as numerical simulations (*Biastoch et al.*, 2008a,b). The retroflection loop is an unstable configuration, and hence occasionally pinches off Agulhas rings, which are the largest mesoscale eddies in the world Ocean (*Olson and Evans*, 1986). In the form of Agulhas rings, warm and saline water is transferred within the sea surface layer from the Indian Ocean into the South Atlantic Ocean (*Lutjeharms and Gordon*, 1987; *Duncombe Rae*, 1991). Underlying the Agulhas Current, NADW is transported in reverse direction along the continental slope off the south and east coast of southern Africa at a general depth of 2000 to 3500 m (*Toole and Warren*, 1993; *van Aken et al.*, 2004). With a similar direction as NADW, cold AABW flows from the Agulhas Basin through the 50 km wide Agulhas Passage into the Transkei Basin (*Camden-Smith et al.*, 1981; *Mantyla and Reid*, 1995). Fluctuations in direction and strength of bottom currents in the Agulhas Passage have been further observed by continuous current measurements (*Camden-Smith et al.*, 1981). The cold NADW and AABW are transported from

the Atlantic Ocean through the Agulhas Passage into the Indian Ocean within the lower limb of the MOC.

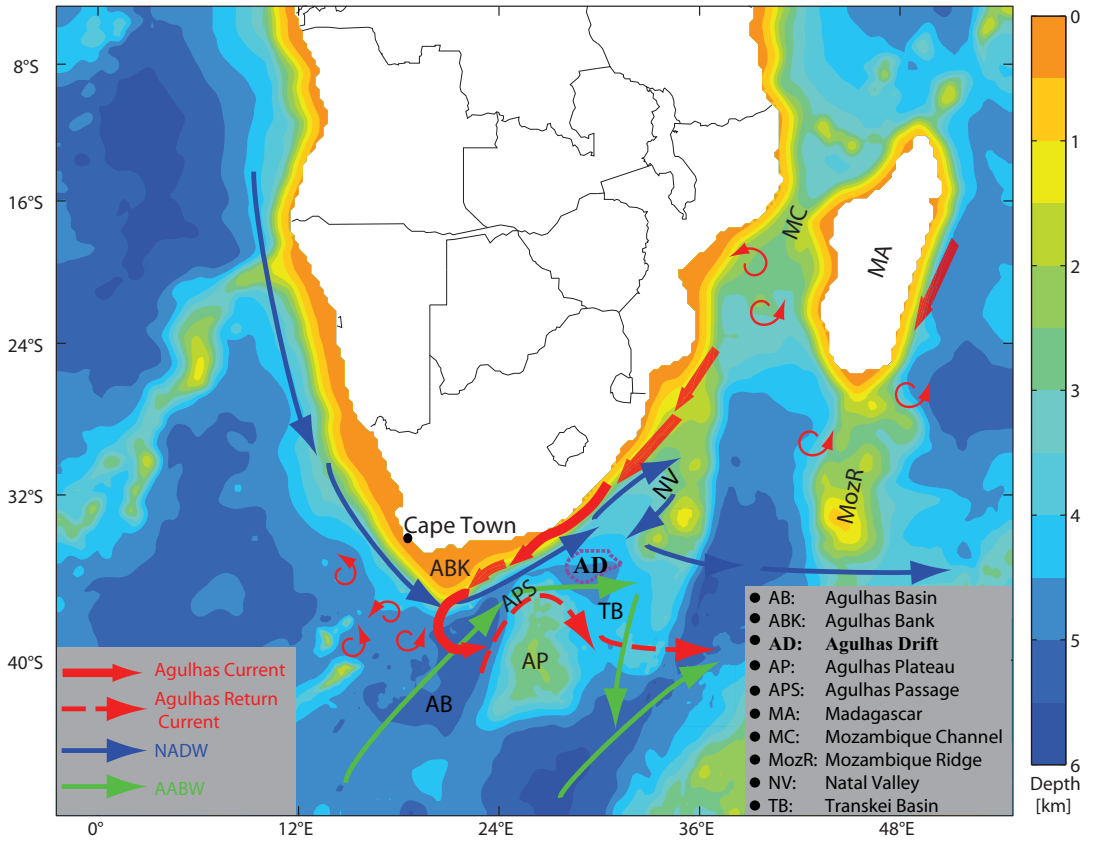

Figure 1.2.: Oceanographic settings at the South African Gateway. The flow paths of the different water masses are schematic, and based on the study of *Lutjeharms* (2006). The magenta dashed lines show the computed boundary of the Agulhas Drift (after *Schlüter and Uenzelmann-Neben*, 2008).

Increase or reduction of the Indian–Atlantic interocean exchange leads to strengthening or weakening of the MOC. The magnitude of this watermass exchange is therefore considered to be important for balancing the MOC and to be indicative for changes in the climate system. A great deal of research has been carried out at the South African Gateway in order to obtain insight into the Indian–Atlantic Ocean exchange. The reconstructions from proxy data (e.g. *Rau et al.*, 2002; *Peeters et al.*, 2004; *Martínez-Méndez et al.*, 2008) and model studies (e.g. *Knorr and Lohmann*, 2003) indicated that this exchange was highly variable over large geological timescale. These investigations further suggested that the strength of

the exchange enhanced during present and past interglacials, while it was reduced during glacial intervals. Therefore, the change in currents at the South African Gateway is considered as a precursor to reestablishment and maintenance of full interglacial conditions.

Seismostratigraphic analysis of the Agulhas Drift at the South African Gateway

Not only the variability in the magnitude of the watermass exchange has been observed, but the change of the flow directions of the water masses at the South African Gateway was suggested by the seismostratigraphic investigations (e.g. *Ben-Avraham et al.*, 1994; *Niemi et al.*, 2000; *Uenzelmann-Neben*, 2002; *Schlüter and Uenzelmann-Neben*, 2007). In these studies, several contourite drifts were revealed in the Transkei Basin and the Natal Valley by seismic reflection data. The term, contourite drift refers to sediment accumulations deposited by bottom currents in general (*Rebesco et al.*, 2008) (for details see Section 2.1). This definition indicates that path and strength of bottom water flow are important factors controlling drift location, morphology and depositional pattern. Any modifications in the hydrographic system are sensitively recorded in contourite drifts. Hence, they provide a link between oceanographic processes and sedimentary record. Studying the architecture of sediment drifts is an effective method to obtain information on paleocirculation that further links to past climates of a certain region (*Stow et al.*, 2002; *Shanmugam*, 2006, 2008).

In the Oligocene, the bottom water flowed along the southeast African continental rise at ≈ 4000 m water depth and then through the Transkei Basin from the north to south (*Niemi et al.*, 2000). The flow of the bottom water offshore South Africa shifted slightly northward in the Early Miocene(*Ben-Avraham et al.*, 1994; *Niemi et al.*, 2000). The bottom water flowed along the continental shelf and further moved northeastward into the Natal Valley at the depths of 3800 to 3600 m. Since Middle Miocene time, the abyssal circulation in the Transkei Basin was predominantly characterized as a northward inflow of the bottom wa-

ter (*Schlüter and Uenzelmann-Neben*, 2007, 2008) via the southern gateway of the Transkei Basin. From the Late Pliocene, the main flow of the bottom water has shifted back through the Agulhas Passage. The bifurcated structure of the bottom water suggested that the cold AABW flows eastward across the Transkei Basin and the NADW flows northeastward at the base of the continental slope (*Schlüter and Uenzelmann-Neben*, 2007, 2008).

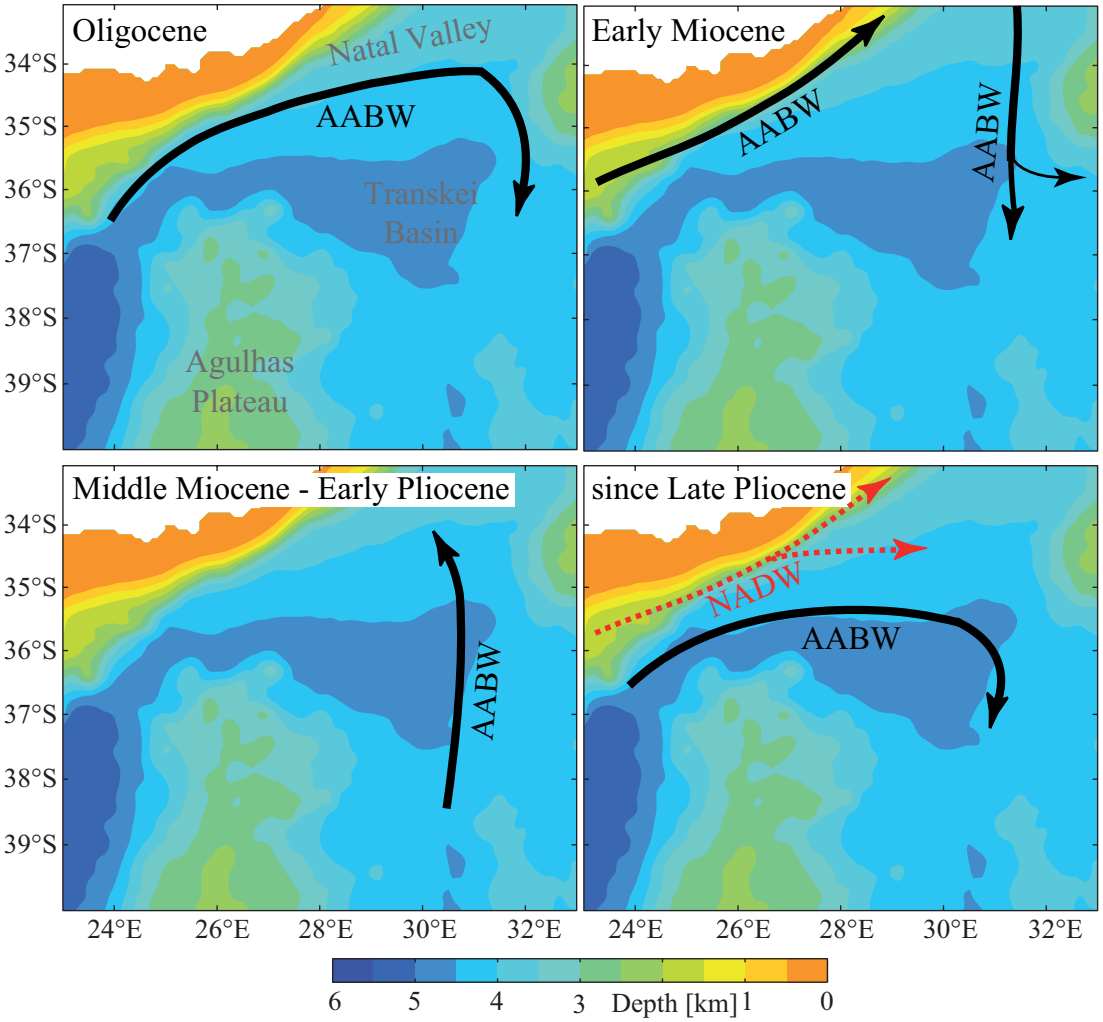

Figure 1.3.: Changes in the flow paths according to the seismostratigraphic analyses (e.g. *Ben-Avraham et al.*, 1994; *Niemi et al.*, 2000; *Schlüter and Uenzelmann-Neben*, 2007)

The last bottom circulation pattern is evidenced both from present–day oceanographic data (*Mantyla and Reid*, 1995; *Casal et al.*, 2006) and the seismic anal-

yses of a contourite drift, the Agulhas Drift in the Transkei Basin (*Schlüter and Uenzelmann-Neben*, 2007, 2008) (for details see Section 2.2). In the seismic profiles, the Agulhas Drift is identified as the youngest seismostratigraphic unit. It appears extending in east–west direction and is asymmetrical with a steeper southern flank and gentler sloping northern flank. These internal geometries suggest that sediments were transported by an AABW branch flowing eastwards into the Transkei Basin, amd deposited to the left of the flow due to the deceleration of the current momentum and the Coriolis force, and then built up the Agulhas Drift (*Schlüter and Uenzelmann-Neben*, 2007, 2008).

Motivations

In view of the previous studies, the motivation of this study is to deepen the understanding of influences of the recent current conditions on sediment distribution in the region of the Agulhas Drift.

As previously mentioned, based on the analysis of seismic data, the evolution of the current pathways is reconstructed at geological timescale. However, to date, no direct and continuous hydrographic measurements at the abyssal depth in the Transkei Basin are available. Therefore, detailed information about the local current conditions on a smaller timescale (e.g. about decades) is missing. The major hydrodynamic processes in the region of the Agulhas Drift, which are important for the sediment transport patterns, are still unknown. Hence, the first question addressed in this thesis is:

(1) Which hydrodynamic processes strongly influence sediment transport patterns over relatively short–term periods at the Agulhas Drift and in its vicinity and how?

It has been recognized that there is link between current strength and grain size (e.g. *Hollister*, 1993; *Stow et al.*, 2002). The coarser the sediments involved in the deposit, the stronger should be the currents. However, the information about the grain size distribution of the Agulhas Drift is still missing due to lack of

drilling data. Hence, we attempt to obtain an insight into the sediment transport patterns for different grain size classes at the Agulhas Drift under the local current conditions. Thereby, we can get possible answers for the following question:

(2) What are the potential components of the Agulhas Drift and their corresponding erosion, transport and depositional processes under the local current condition?

The major sediment source of the Agulhas Drift further remains an enigma. The Agulhas Drift is located in the Transkei Basin, which is far away from any terrigenous sediment source. The sediments deposited at the Agulhas Drift cannot be directly transported from the continents. Hence, the development of the Agulhas Drift might be related to post–depositional processes. The third question in this thesis is therefore:

(3) Where is the region for sediment resuspension that might act as a potential source of the Agulhas Drift?

Methods

As mentioned before, continuous oceanographic and sedimentological measurements at the Agulhas Drift are missing. In order to answer the questions mentioned above, the advantages of numerical tools, which allow to represent any oceanic processes over a large study area, have been taken.

Previous modeling studies in this region focus on the intricacies of the Agulhas Current System and inter–ocean water exchange. For instance, *Chassignet and Boudra* (1988) studied the ring formation from the Agulhas Retroflection by means of a numerical model, which solves primitive equations on quasi–isopycnic coordination (*Bleck and Boudra*, 1986). Similar issue was studied by *Lutjeharms et al.* (2003) with the Regional Ocean Modeling System (ROMS) (*Haidvogel et al.*, 2000; *Shchepetkin and McWilliams*, 2003, 2005). A global ocean general circulation model (OCCAM) (*Webb et al.*, 1997a, 1998) was applied to observe the interocean exchange of thermocline and intermediate waters in the South At-

lantic Ocean (*Donners and Drijfhout*, 2004). With the development of model systems, the resolution is allowed to be enhanced to resolve the mesoscale processes offshore South Africa (e.g. *Penven et al.*, 2006a; *Biastoch et al.*, 2008a,b). However, prior to this thesis, there is no numerical study to observe the local abyssal current–controlled sedimentary features. Hence, a new implementation of oceanic model is carried out in this study to provide a possibility to observe hydrodynamic and sediment transport processes at the abyssal depth in the region of the Agulhas Drift.

The Regional Ocean Modeling System (ROMS) is chosen to simulate ocean circulation and sediment transport processes in the entire region offshore southern Africa shown in Figure 1.2. This open source modeling system has been successfully used to simulate the most active current in the study area, the Agulhas Current (*Lutjeharms et al.*, 2003; *Penven et al.*, 2006a). Furthermore, a sediment transport model has been developed as an integral part of ROMS (*Warner et al.*, 2005; *Blaas et al.*, 2007; *Warner et al.*, 2008a).

Using the ROMS, the oceanic circulation is first simulated to examine hydrodynamic processes at the Agulhas Drift. It thus provides part of the answer for the question (1) (Figure 1.4). To completely answer this question, sediment transport model is further implemented simultaneously with oceanic circulation model (Figure 1.4). The influences of the current system on the sediment transport patterns can be thereafter observed. On the basis of these fundamental implementations, numerical experiments on the sediment grain size classes are carried out (Figure 1.4). Sediment transport patterns for different classes of silt are compared, so that a possible answer of question (2) can be obtained. Finally, in order to answer the question (3), sediment suspension is considered as the unique sediment source in our Models. Hence, the regions, where the sediments on the sea floor can be eroded into the water columns, can be clearly recognized in the simulations. Complete details of ROMS and its application are described in chapter 3.

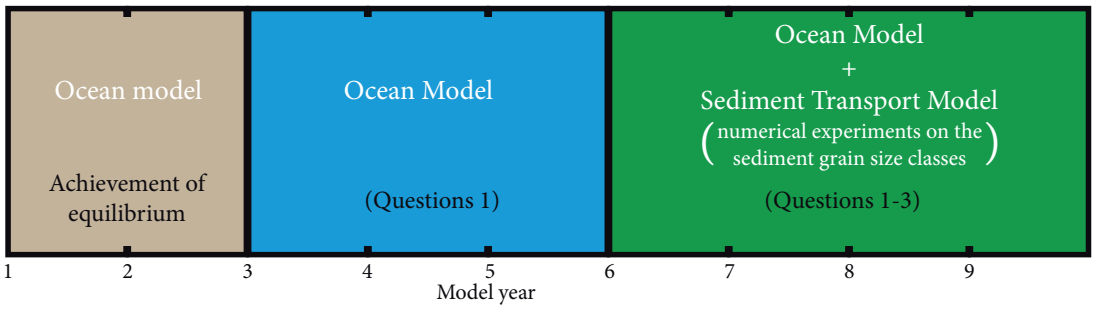

Figure 1.4.: Run chart for model on the basis of application of ROMS

Thesis Outline

This dissertation continues with a more detailed description of the material covered in this introduction. The 2nd chapter deals with contourite drift. After the pertinent background on contourite is laid out, the seismic analyses of Agulhas Drift and the subsequent suggestion on the change of local current path are presented. In Chapter 3, a basic description of the Regional Ocean Modeling System (ROMS) is first introduced, and then our model configurations are described. Our models are evaluated in Chapter 4 by comparing the simulation results with available measured data. Detailed outputs from the oceanic circulation model are provided in Chapter 5. A further discussion in this chapter offers a physical mechanism which might produce simulated hydrodynamic characteristics. Chapter 6 gives detailed results and discussions about the sediment transport model. Chapter 7 contains a summary and concluding remarks, and then some ideas for future projects will be provided as outlooks.

2

Agulhas Drift: A Contourite Drift in the Transkei Basin

The numerical studies presented in this thesis are related to the geodynamic development of the Agulhas Drift. It is interpreted as a contourite drift in the central Transkei Basin (e.g. *Ben-Avraham et al.*, 1994; *Schlüter and Uenzelmann-Neben*, 2007). A general introduction of contourites are generally is given in Section 2.1, and then the details about the Agulhas Drift are described in Section 2.2.

2.1 Contourites

Contourites are sediments deposited or substantially reworked by the strong action of bottom currents (*Rebesco and Stow*, 2001; *Rebesco*, 2005). This influence of the bottom current on the sedimentation processes in the deep oceans was initially recognized by the German oceanographer Wust in 1936. However, the concept of contourites has been widely accepted only after the American team of Heezen and Hollister provided geological and oceanographic evidence of this process along the eastern North American continental margin in the late 1960s (e.g. *Heezen and Hollister*, 1964, 1971). In the past decades, a certain number of projects have been conducted and some important achievements have been made in further understanding of the geological effects of ocean bottom currents (e.g. *Ezer and Weatherly*, 1991; *Hollister and Nowell*, 1991a; *Rebesco et al.*, 2002).

2.1.1 Terminology

With the rapid development of contourite research, the mixed terminology occurs because there is a need to maintain a certain degree of flexibility that allows for development in understanding. Nevertheless, a clearer usage of contourite terminology is also important for description of the products (sediments) and consequently for understanding of the depositional processes.

The term 'contourite' was originally introduced to define the sediments deposited in the deep sea by contour–parallel bottom currents. However, the bottom current–controlled deposits were also recognized in shallow gateways, outer shelf and slopes, and even lakes. On the other hand, the directions of the bottom currents are seldom precisely identifiable. Hence, the original definition of contourite is extremely rigorous and would limit its application. Subsequently, the term was widened to embrace a larger spectrum of sediment deposits that at diverse depths are affected to various extents by different types of currents.

The terms 'contour current' and 'bottom current' are frequently mentioned in contourite studies and are often treated as a pair of synonyms. However, in the strict sense, there is difference in their definitions. The term 'contour current' should be actually applied only to those thermohaline–driven, deep–water currents that flow approximately paralled to the bathymetric contours. In contrast, 'bottom current' includes all abyssal currents. The latter is more widely used, when the current capabilities of eroding, transporting and depositing sediments are described.

Based on the distinction between these two terms, it is possible to give a clear description of two allied terms about the depositional processes. 'Sediment drift' is the generic term for any sediment accumulation that was controlled by the action of bottom currents. There is an often used synonym 'contourite drift', which in contrast should be specifically used for sediment accumulations deposited principally (though not exclusively) by contour currents. In most cases, the most appropriate term for contourite accumulations is the widly applicable definition

of 'sediment drift' or simply 'drift', and hence they are mainly used in this thesis.

2.1.2 Bottom Currents

The formation processes of sediment drifts are largely dependent on bottom currents. There is a wide spectrum of bottom currents, which includes part of the meridional overturning circulation (MOC) (see chapter 1, p. 1) and major wind–driven circulation. The dominant wind systems govern the existing global surface circulation (*Sudre and Morrow*, 2007). In some cases, the action of such wind–driven currents affects the entire water column down to the seafloor. Obvious examples of this are the strong Antarctic Circumpolar Current and the western boundary currents like the Gulf Stream, or Agulhas Current (e.g. *Dengler et al.*, 2004; *Casal et al.*, 2006).

All the above currents may erode, transport and deposit sediments in the form of contourites. Generally, these bottom currents have very slow velocities (few centimeters per second) and hence are just able to slightly affect sediment transport processes. However, bottom currents may speed up when constrained by certain factors including seafloor morphology (obstacles, gateways, and changes in slope direction and steepness), Coriolis force, circular motions (gyres and eddies), and eddy kinetic energy changes. For instance, within the geographical region covered in this thesis, the velocities of bottom currents is up to $80\,\mathrm{cm\,s^{-1}}$ in the narrow Agulhas Passage (*Camden-Smith et al.*, 1981). As another example, the bottom currents accelerate when a North Atlantic deep–water eddy is ejected over the Agulhas Plateau (*Casal et al.*, 2006). In many cases, these accelerated bottom currents are strong enough to influence sedimentation in the deep ocean by a number of processes such as the prevention of fine sediment deposition, or the erosion and transport by traction of silt and fine sand. Such vivid processes take place mainly beneath the core of bottom currents. The velocities decrease away from the axis of the current, and then deposition of various types of contourites take place in the relatively slack waters to the side of sediment–laden bottom cur-

rents. Due to the Coriolis Force, sediments are deposited on the left (right) side of the current direction in the Southern (Northern) Hemisphere (e.g. *Faugères et al.*, 1999; *Rebesco and Stow*, 2001; *Shanmugam*, 2006).

According to the above mentioned effects of currents on sediment transport, in most paleocurrent reconstructions, the axis of the current is hence generally considered subparallel to the elongated direction of sediment drift and on the right (left) hand side of sediment drift in the Southern (Northern) Hemisphere. However, in most case, such relation between current and sediment accumulation is highly speculative, since the associated time–scales required for a drift development are orders of time span of the direct oceanographic observations, which in fact show that the current velocity and direction are extremely variable in both time and space. Hence, to obtain more details about bottom currents, other methods such as numerical simulations should be carried out.

2.1.3 Sediment Drifts

Under the action of bottom currents, sediments can be deposited as contourites. Since the currents are variable in time and space, there is a large variety of contourites. For instance, their dimensions range from a few tens to several hundred thousand square kilometers. Besides, the accumulation rates vary from a few tens to hundreds of meters per million years. The features of contourites are mainly controlled by a number of interrelated factors:

- bathymetric setting (physiography, depth, and morphology),
- current conditions (velocity and its variability),
- sediment availability (amount, type, source type, and variability of input),
- Coriolis force (significantly at high latitudes),
- interaction with other depositional processes (in time and space, either collaboratively or antagonistically).

The complexity of sediment accumulation processes results in difficulties in identifying contourites. Distinguishing sediment drifts becomes particularly challenging when they are partially interbedded with the surrounding sediments. The difficulties encourage a development of a categorization scheme for sediment drift types (Figure 2.1). Such a classification, in return, can be used to evaluate geomorphic, geologic, and oceanographic settings of palaeo–oceans (e.g. *Faugères et al.*, 1993; *Stow and Mayall*, 2000).

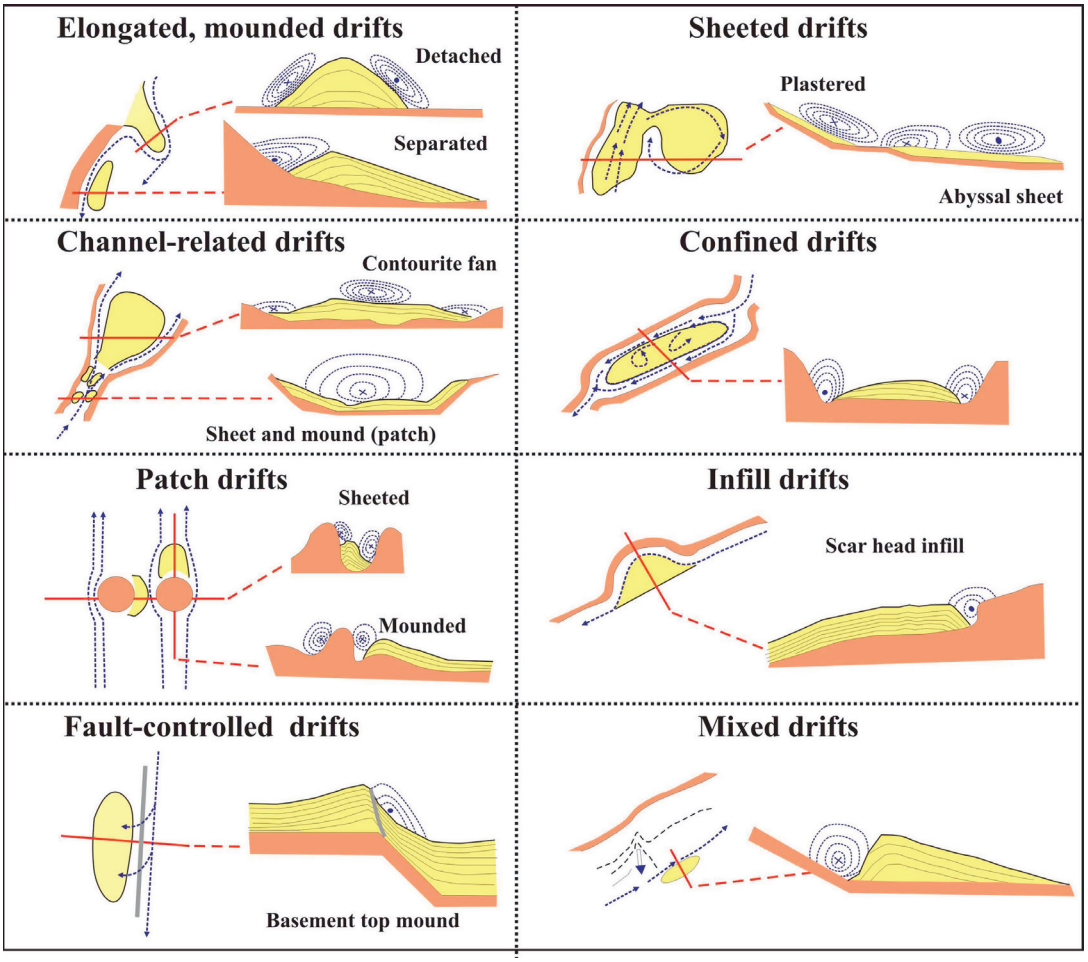

Figure 2.1.: Up and lateral view of sediment drift types and inferred bottom current paths (after *Rebesco and Stow*, 2001; *Rebesco*, 2005; *Rebesco et al.*, 2008). The large–scale geometry of contourites is represented by the seismic expression. Red lines on up views indicate the location of the lateral view. The axis of bottom–currents is marked as black dashed lines in up view and as black dashed arches in lateral view.

In some instances, the classification of contourite sediment drifts can be recognized on the basis of seismic profiles. A three–scale set (large, medium and small scale) of seismic diagnostic criteria has been developed to enable confirmative identification of contourites (*Faugères et al.*, 1999; *Stow and Mayall*, 2000). The large–scale features, which include geometry, dimensions, elongation and widespread regional discontinuities of entire sediment body (Figure 2.2), reflect long lasting stable condition for the sediment drift. Medium scale features, namely depositional seismic units (Figure 2.2) are formed as a result of local variation in sedimentary processes and accumulation rates linked to changes in current activity. In greater detail, the nature of individual seismic facies can be interpreted from small–scale structures in seismic profiles.

2.2 Agulhas Drift

Based on the knowledge of contourites, significant progress has been made on the studies of the Agulhas Drift, the contourite in the Transkei Basin situated southeast of South Africa.

The Agulhas Drift was previously mapped as an east–west extending sediment ridge (*Camden-Smith et al.*, 1981; *Dingle and Camden-Smith*, 1979). These earlier studies showed that the Agulhas Drift extends for at least 350 km along approximately 35.15 °S. The details of its internal structure were initially provided by earlier seismic studies of *Ben-Avraham et al.* (1994) and *Niemi et al.* (2000). In their seismic reflection profiles, the Agulhas Drift appears asymmetrical with a steeper southern flank and gentler sloping northern flank. According to its internal geometries, the Agulhas Drift was classified as an elongate mounded drift (*Niemi et al.*, 2000) (Figure 2.1).

In the recent high resolution seismic reflection profiles, which were recorded during R/V SONNE cruise SO–182 in Spring 2005, the Agulhas Drift is identified as the youngest seismostratigraphic unit (i.e. unit 5 in Figure 2.2) to build up the drift with a root mean square thickness of 150.4 m (*Schlüter and Uenzelmann-*

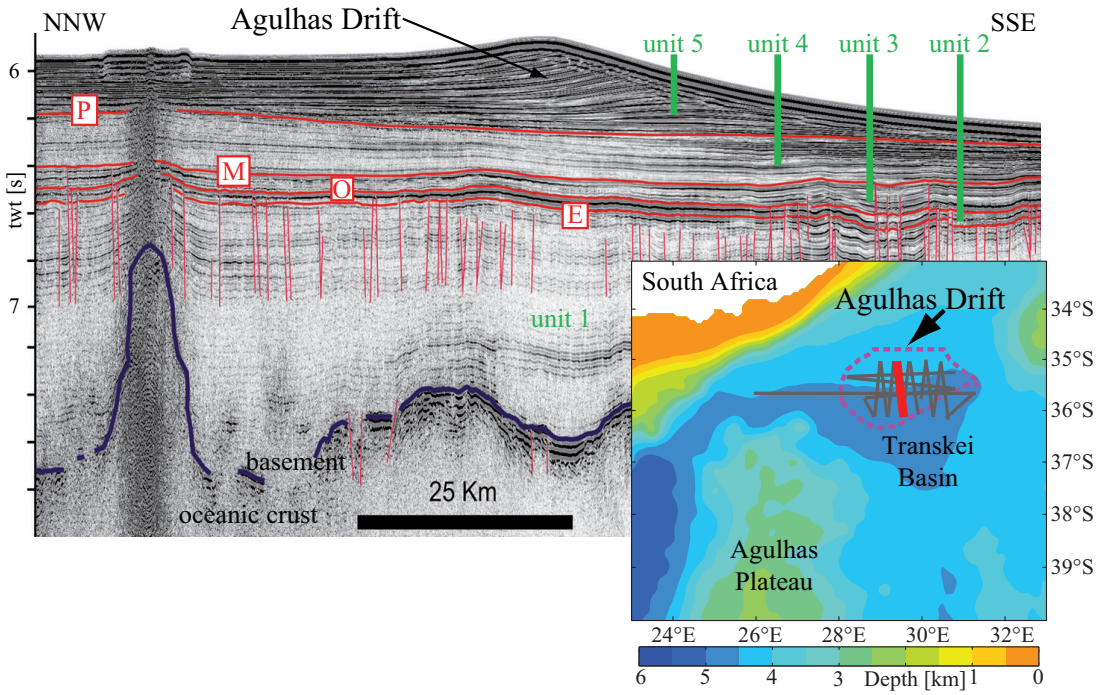

Figure 2.2.: A 2D seismic reflection profile acquired in Transkei basin during R/V SONNE cruise SO–182. Its interpretation shows acoustic basement (blue line), seismic reflectors (red lines) and seismostratigraphic units 1 to 5 on the basis of the study of *Niemi et al.* (2000). E: Late Eocene; M: middle Miocene; O: Eocene/Oligocene boundary; P: early Pliocene. (Modified after *Schlüter and Uenzelmann-Neben*, 2007). Inset: The location of this seismic profile (red line) profile and the other high resolution seismic reflection survey profiles (grey lines) collected during the cruise. The magenta dashed lines show the computed boundary of the Agulhas Drift (after *Schlüter and Uenzelmann-Neben*, 2008).

Neben, 2007, 2008). A map of the thicknesses of this unit, which are obtained from all seismic profiles, visualized the partial geometry of the Agulhas Drift (Figure 2.3). Unfortunately, an entire direct view of Agulhas Drift cannot be obtained due to the limited coverage area of the seismic profiles. However, on the basis of this map, a self–consistent model developed further by *Schlüter and Uenzelmann-Neben* (2008) suggested that the Agulhas Drift has been built up by a branch of AABW flowing eastward through the Agulhas Passage since 3 Ma.

Additionally, the high resolution seismic profiles revealed presence of another contourite drift (M–Drift), which is beyond the Agulhas Drift and perpendicular to it. The south–northward elongation of M–Drift indicated that a local change

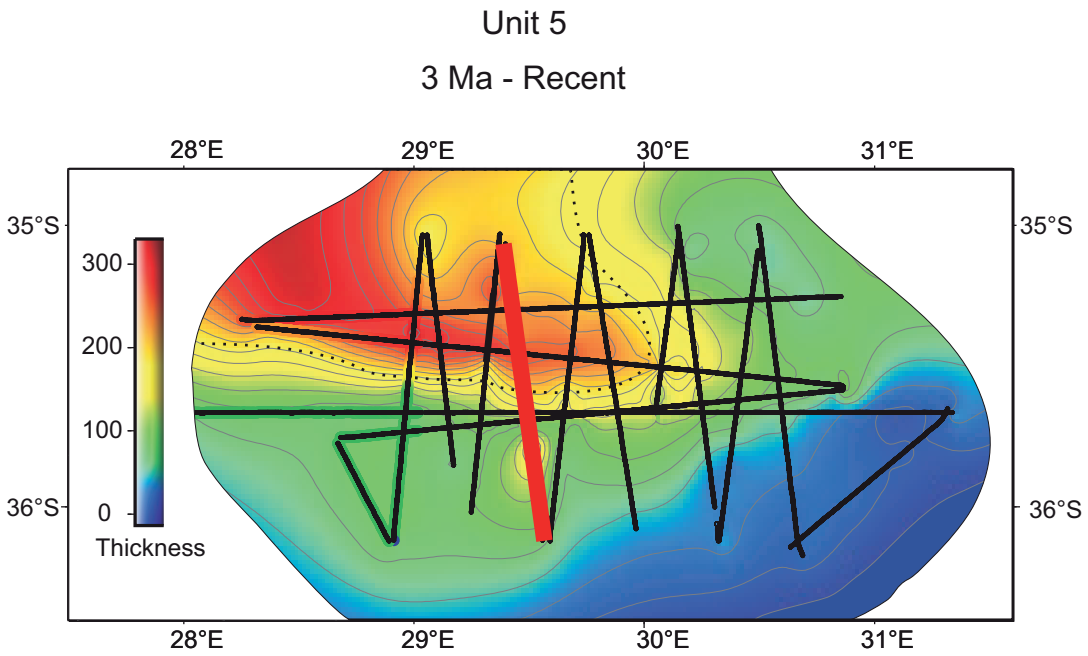

Figure 2.3.: Map of thicknesses of the youngest seismostratigraphic unit. Note that Agulhas Drift is indicated by the thicknessees larger than zero. Black lines indicate location of seismic reflection profiles. The horizontal red line labels the position of the seismic profile of Figure 2.2 (Modified after *Schlüter and Uenzelmann-Neben*, 2008).

of AABW direction (*Niemi et al.*, 2000; *Schlüter and Uenzelmann-Neben*, 2007). This flow of deep water might have oriented in a south–north direction from 15 Ma to 3 Ma.

On the basis of these seismic surveys, the influences of the bottom water on the sedimentary features of the Agulhas Drift are further studied by means of numerical method.

3

Method – A Regional Model Offshore Southern Africa

The Regional Ocean Modeling Systems (ROMS) used for this thesis is an advanced open source 3D ocean model (e.g. *Haidvogel et al.*, 2000; *Shchepetkin and McWilliams*, 2003, 2005). It solves free surface, hydrostatic primitive equations over stretched topography–following vertical coordinates (s–coordinate system) and orthogonal horizontal coordinates with providing of forcing data, boundary conditions and initial conditions on a regional scale (Figure 3.1). ROMS further includes several coupled models, such as biogeochemical (*Powell et al.*, 2006; *Fennel et al.*, 2006), sea ice (*Budgell*, 2005) and sediment transport(*Warner et al.*, 2005; *Blaas et al.*, 2007; *Warner et al.*, 2008a) applications. In addition, local mesh refinement capability has been added to ROMS (*Shchepetkin and McWilliams*, 2005; *Penven et al.*, 2006b) utilizing the advantage of the Adaptive Grid Refinement in Fortran (AGRIF) package (*Blayo and Debreu*, 1999; *Debreu et al.*, 2008). For more details regarding the theoretical background of ROMS, see `http://roms.mpl.ird.fr/`.

This chapter begins with a basic description of the ROMS (see Section 3.1). The primitive equations and the equations for boundary conditions are first given in Section 3.1.1, the vertical coordinates are then introduced in Section 3.1.2, after that the algorithm of the sediment transport model is described in Section 3.1.3. Finally, the detailed model configurations including model domain, grids, and input data sets are provided in Section 3.2.

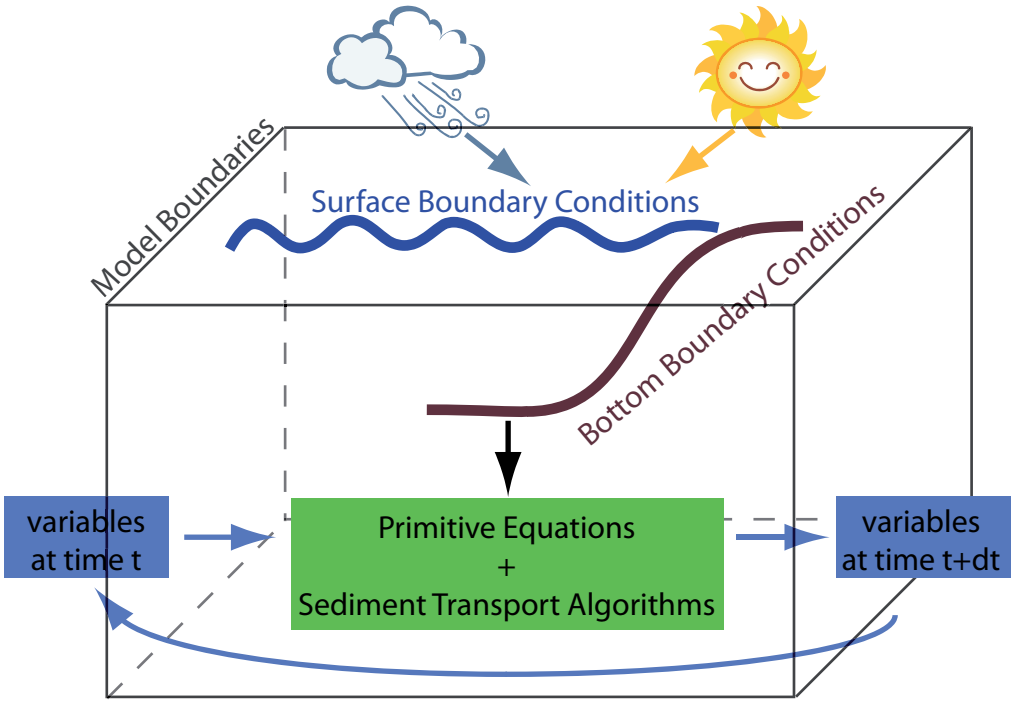

Figure 3.1.: Principle of simulation models for calculating realistic ocean circulation.

3.1 Model Description and Boundary Conditions

3.1.1 Equations of Motion

The primitive equations used in ROMS are a set of nonlinear differential equations that are used to approximate global oceanic/atmospheric flows. Here, these equations are written for Cartesian tangential plane (i.e. a plane tangent to some point on the surface of the Earth). This form does not take the curvature of the Earth into account, but is useful for visualizing some of the physical processes involved in formulating the equations due to its relative simplicity. In addition, the effects of forcing and horizontal dissipation will be represented by the schematic terms $\mathcal{F}$ and $\mathcal{D}$, respectively.

The momentum balance in the x– and y–directions take the form:

$$\frac{\partial u}{\partial t} = -u\frac{\partial u}{\partial x} - v\frac{\partial u}{\partial y} - w\frac{\partial u}{\partial z} + fv - \frac{\partial \phi}{\partial x} + \mathcal{F}_u + \mathcal{D}_u \tag{3.1}$$

$$\frac{\partial v}{\partial t} = -u\frac{\partial v}{\partial x} - v\frac{\partial v}{\partial y} - w\frac{\partial v}{\partial z} - fu - \frac{\partial \phi}{\partial y} + \mathcal{F}_v + \mathcal{D}_v \tag{3.2}$$

The scalar concentration fields, for instance, temperature T and salinity S are governed by the advective–diffusive equation:

$$\frac{\partial T}{\partial t} = -u\frac{\partial T}{\partial x} - v\frac{\partial T}{\partial y} - w\frac{\partial T}{\partial z} + \mathcal{F}_T + \mathcal{D}_T \tag{3.3}$$

$$\frac{\partial S}{\partial t} = -u\frac{\partial S}{\partial x} - v\frac{\partial S}{\partial y} - w\frac{\partial S}{\partial z} + \mathcal{F}_S + \mathcal{D}_S \tag{3.4}$$

The equation of state is given by:

$$\rho = \rho(T, S, P) \tag{3.5}$$

In the Boussinesq approximation, density variations are neglected in the momentum equations except in their contribution to the buoyancy force in the vertical momentum equation. Under the hydrostatic approximation, it is further assumed that the vertical pressure gradient balances the buoyancy force:

$$\frac{\partial \phi}{\partial z} = -\frac{\rho g}{\rho_0} \tag{3.6}$$

Finally, the continuity equation for an incompressible fluid is expressed as

$$0 = \frac{\partial u}{\partial x} + \frac{\partial v}{\partial y} + \frac{\partial w}{\partial z} \tag{3.7}$$

The variables of the primitive equations are:

x, y, z: the coordinates in the Cartesian frame (z marks vertical coordinate positive upwards)

u, v, w: are components of the velocity vectors in this frame

f: the Coriolis parameter

ϕ: the dynamic pressure

$\mathcal{F}_u$, $\mathcal{F}_v$, $\mathcal{F}_T$, $\mathcal{F}_S$: the forcing terms

$\mathcal{D}_u$, $\mathcal{D}_v$, $\mathcal{D}_T$, $\mathcal{D}_S$: the dissipation terms

T: the potential temperature of the Ocean

S: the salinity of the Ocean

P: the total pressure

$\rho_0 + \rho$: the total in–situ density

g: the acceleration of gravity

Since the ROMS is a regional oceanic model, a satisfactory prescription for the open boundary conditions is essential. The surface and bottom boundary conditions illustrated in Figure 3.1 can be prescribed at the top, $z = \zeta$:

$$K_M \frac{\partial u}{\partial z} = \tau_{\mathrm{s}}^x(x, y, t) \tag{3.8}$$

$$K_M \frac{\partial v}{\partial z} = \tau_{\mathrm{s}}^y(x, y, t) \tag{3.9}$$

$$K_T \frac{\partial T}{\partial z} = \frac{Q_T}{\rho_0 C_p} \tag{3.10}$$

$$K_S \frac{\partial S}{\partial z} = \frac{(E - P)S}{\rho_0} \tag{3.11}$$

$$w = \frac{\partial \zeta}{\partial t} + u \frac{\partial \zeta}{\partial x} + v \frac{\partial \zeta}{\partial y} \tag{3.12}$$

and at the bottom, $z = -h$:

$$K_M \frac{\partial u}{\partial z} = \tau_{\mathrm{b}}^x \tag{3.13}$$

$$K_M \frac{\partial v}{\partial z} = \tau_{\mathrm{b}}^y \tag{3.14}$$

$$K_T \frac{\partial T}{\partial z} = 0 \tag{3.15}$$

$$K_S \frac{\partial S}{\partial z} = 0 \tag{3.16}$$

$$w = -u \frac{\partial H}{\partial x} - v \frac{\partial H}{\partial y} \tag{3.17}$$

The new variables above are:

ζ**:** the free surface elevation

K_M**,** K_T**,** K_S**:** the vertical diffusivity coefficients

$\tau_{\mathbf{s}}^x$**,** $\tau_{\mathbf{s}}^y$**:** the surface wind stress components

$\tau_{\mathbf{b}}^x$**,** $\tau_{\mathbf{b}}^y$**:** the bottom stress components

Q_T**:** the surface heat flux

$E - P$**:** the evaporation minus the precipitation

H**:** the resting thickness of the water column

For the lateral open boundaries, ROMS, as one of well developed regional models, allows the inner solution to radiate through the boundary without reflection and information from the surrounding ocean to come into the model according to the methods by *Marchesiello et al.* (2001). The outflow is handled in a sponge layer with linearly increasing lateral Laplacian mixing coefficient (*Marchesiello et al.*, 2001). This sponge layer filters out the possible numerical noise or reflections produced by the open boundaries. With this method, the model solution is connected to the surrounding smooth oceanic data after filtering, while the development of a meaningful internal solution is allowed.

3.1.2 Vertical S–Coordinate

The equations listed in the last section are solved over vertical coordinates related to bottom topography. The z–coordinate and s–coordinate (Figure 3.2) are two major coordinate systems used in oceanic models. In z–coordinate system, the depth of same vertical level is constant. Differently, in s–coordinate, the number of vertical levels in the water column is the same everywhere within the domain irrespective of the depth of the water column.

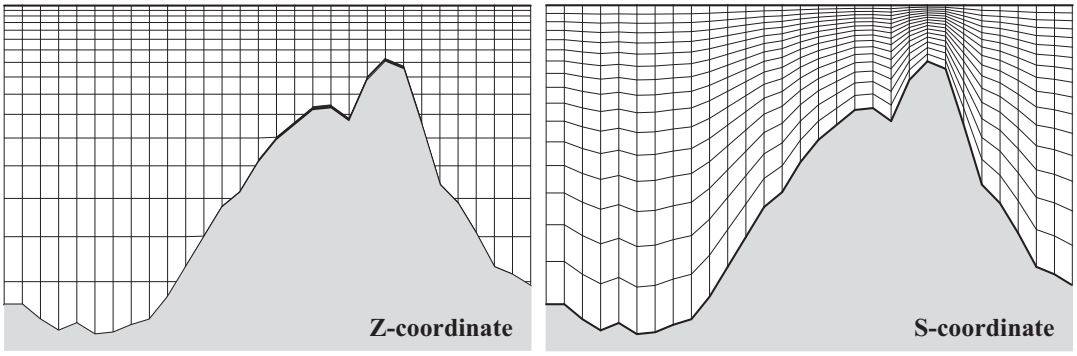

Figure 3.2.: Examples of z–coordinate and s–coordinate

The real oceans have complicated geometry and large changes in bottom depth, ranging from a very few meters near the coast to a few kilometers in the deep basins. As exhibited in Figure 3.2, it is difficult to reveal bottom topography in z–coordinate, especially where the topography is undulating. Consequently, the representation and parameterization of the bottom boundary layer is unnatural. Moreover, the z–coordinate has disadvantage to represent advection and diffusion along inclined density surfaces in the ocean interior (*Mellor et al.*, 2002).

In contrast, a smooth representation of the bottom topography can be obtained in s–coordinate system (Figure 3.2), since the coordinate is normalized by the fluid depth. Because of this advantage, this stretched topography-following coordinate system is used in ROMS. This further allows us to increase vertical resolutions in the bottom layer, and hence to improve simulation performance of processes, such as sediment transport, in the bottom layer.

In ROMS, the vertical transformation equations, which support vertical stretch

of coordinates, can be used to generate a more uniform vertical resolution not only on the bottom but also near the surface. The vertical coordinate transformation takes the form:

$$z(x,y,\sigma,t) = S(x,y,\sigma) + \zeta(x,y,t)\left(1 + \frac{S(x,y,\sigma)}{h(x,y)}\right), \tag{3.18}$$

$$S(x,y,\sigma) = h_c\,\sigma + \Big(h(x,y) - h_c\Big)\,C(\sigma) \tag{3.19}$$

where $S(x,y,\sigma)$ is a nonlinear vertical transformation function, $\zeta(x,y,t)$ is the time–varying free–surface, $h(x,y)$ is the water column thickness and $z = -h(x,y)$ corresponds to the ocean bottom, σ is a fractional vertical stretching coordinate ranging from $-1 \leq \sigma \leq 0$ (i.e. $\sigma = 0$ at the free–surface, $\sigma = -1$ at the ocean bottom and else in between). In the nonlinear vertical transformation function $S(x,y,\sigma)$, h_c is a constant to be chosen as a typical surface mixed layer depth, and $C(\sigma)$ is a vertical stretching function ranging from $-1 \leq C(\sigma) \leq 0$. In ROMS, this function is defined by *Song and Haidvogel* (1994) as:

$$C(\sigma) = (1-\theta_b)\,\frac{\sinh(\theta_s\,\sigma)}{\sinh\theta_s} + \theta_b\left(\frac{\tanh\Big(\theta_s(\sigma+\frac{1}{2})\Big)}{2\tanh(\frac{1}{2}\theta_s)} - \frac{1}{2}\right) \tag{3.20}$$

where θ_s and θ_b are the surface and bottom control parameters. For large θ_s, the finer resolution is kept above h_c; additionally, if θ_b approaches 1, resolution at the bottom boundary is enhanced. In short, θ_s, θ_b, h_c and N (i.e. the number of the vertical layers) are the important parameters to design a custom s–coordinate system.

As mentioned above, the major advantage of s–coordinate models is the transformation of the surface and sea bottom to coordinate surfaces. Unfortunately, this is also the source of pressure gradient error. In order to explain the generation of the error simply, a linear s–coordinate is in use here. The x–component of the pressure gradient force in the topography following coordinate is determined by

the sum of 2 terms:

$$\left.\frac{\partial p}{\partial x}\right|_{z=\text{const}} = \left.\frac{\partial p}{\partial x}\right|_{s=\text{const}} - \frac{s}{h}\frac{\partial p}{\partial s}\frac{\partial h}{\partial x} \tag{3.21}$$

On the right hand side of the Eq. 3.21, the first term involves the variation of pressure along a constant s–surface and the second is the hydrostatic correction. Near steep topography, these two terms are large, comparable in magnitude and tend to cancel each other. A small error in computing either term can result in a relatively large error in horizontal pressure gradient.

Song (1998) and *Kliem and Pietrzak* (1999) proposed different ways to reduce these errors in the pressure gradient scheme of the ROMS. In addition, topographic smoothing is another important method to ensure stable and accurate solving of equations involving the gradient of total pressure along the s–coordinate. A parameter is introduced by *Beckmann and Haidvogel* (1993) as

$$r = \frac{\Delta h}{2h} = \frac{h_{+1/2} - h_{-1/2}}{h_{+1/2} + h_{-1/2}} \tag{3.22}$$

where h is the depth of water as ever. If r is larger than a target value, which can be chosen as an empirical value, the topography is smoothed using a Shapiro filter.

3.1.3 Sediment Transport Model

Sediment Transport Algorithms

A sediment transport model has been developed as an integral part of ROMS (*Blaas et al.*, 2007). The suspended sediment concentrations (C_j) for sediment size class j in the water column is solved by the advection–diffusion equation with two additional terms added for (1) vertical settling and (2) sources related to erosion (E_{sj}) in our implementation, as follows:

$$\frac{\partial C_j}{\partial t} + \frac{\partial u_i C_j}{\partial x_i} - \frac{\partial}{\partial x_i}\left(K\frac{\partial C_j}{\partial x_i}\right) = \frac{\partial w_{sj} C_j}{\partial x_3} + E_{sj} \tag{3.23}$$

Subscripts i denotes coordinate direction (with x_3 vertically upward), u_i is velocity, K is vertical diffusivity tensor, w_{sj} is the vertical settling velocity (positive upwards), and E_{sj} is the erosion flux.

For each sediment size class, setting velocity (w_{sj}) is computed from the empirical function of grain size by *Soulsby* (1995, 1997) as:

$$w_{sj} = \frac{1.3}{\rho}\left(\sqrt{a^2 + bD^3} - a\right)/d_j, \tag{3.24}$$

$$D = d_j \sqrt[3]{g(\rho_s/\rho - 1)/\left(1.3/\rho\right)^2} \tag{3.25}$$

where d_j is grain diameter for sediment size class j, ρ_s is density of sediment, ρ is density of water and g is gravity, and a and b are constants with $a = 10.36, b = 1.049$.

The erosion flux E_{sj} is parameterized following *Ariathurai and Arulanandan* (1978) as:

$$E_{sj} = \begin{cases} E_{0,j}\left(1-\varphi\right) f_j \left(\frac{\tau_b - \tau_{\mathrm{cr},j}}{\tau_{\mathrm{cr},j}}\right), & \text{for } \tau_b \geq \tau_{\mathrm{cr},j} \\ 0, & \text{otherwise} \end{cases} \tag{3.26}$$

Here $E_{0,j}$ is a bed erodibility constant, φ is the porosity (volume of voids/total volume), f_j is the volumetric fraction of sediment of class j, τ_b is the magnitude of bed shear stress, and $\tau_{\mathrm{cr},j}$ is the critical shear stress.

The bed erodibility constant is $E_{0,j}$ is modified from the entrainment rate E_{uj}, which can be obtained according to the parameterization of *Garcia and Parker* (1991) as:

$$E_{uj} = \gamma_0 w_{sj} \rho_s \tag{3.27}$$

with the constant $\gamma_0 = 1 \times 10^{-3}$ to 1×10^{-5}.

The critical (skin frictional) shear stress $\tau_{\mathrm{cr},j}$, beyond which sediment starts to move, is derived from the critical Shields parameter according to the assumption of suspended load transport. They are determined by using the approximation of

Soulsby (1995) and *Soulsby and Whitehouse* (1997) as:

$$\tau_{\mathrm{cr}} = \rho\,(0.8\,w_{sj})^2 \tag{3.28}$$

The bed shear stress τ_b is determined by the hydrodynamic routines as:

$$\tau_b = \rho\left(\frac{k}{\ln\left(z/z_{ob}\right)}\right)^2 u^2\Bigg|_{z=z_a} \tag{3.29}$$

where $k = 0.4$ is the Von Kármán constant, z_{ob} is bottom roughness height, u is velocity at the bottom, and $z = z_a$ is a reference height above the ocean bottom.

Sediment Classes

The sediment transport model of ROMS is capable of representing transport patterns of user–defined sediment classes. From above, it is indicated that the characteristics of different types of the sediment size classes retain on grain diameter (d_j), settling velocity (w_{sj}), entrainment rate (E_{uj}) and critical shear stress ($\tau_{\mathrm{cr},j}$). Two classes of non–cohesive sediments are included in the default model framework of ROMS, whereas the number of sediment classes is increased to 4 for this thesis. They are calculated separately as noncohesive sediments, as so far the algorithms governing cohesive sediment dynamics are still being developed and are not discussed here.

The Wentworth scale or Udden–Wentworth scale 1922 is used to define the grain–size ranges and the names of the textural groups defines grain–size ranges and the names of the textural groups (gravel, sand, silt, and clay) and subgroups (fine sand, coarse silt, etc.) (Figure 3.3).

3.2 Model Configurations

Essential steps for model configurations are presented in this section. Furthermore, the structure of the section follows the operational sequence of configuration procedure.

Millimeters	µm	Phi (ϕ)	Wentworth size class	
		-20		
4096		-12	Boulder (-8 to -12ϕ)	
1024		-10		
256		-8	Pebble (-6 to -8ϕ)	
64		-6		
16		-4	Pebble (-2 to -6ϕ)	Gravel
4		-2		
3.36		-1.75		
2.83		-1.50	Gravel	
2.38		-1.25		
2.00		-1.00		
1.68		-0.75		
1.41		-0.50	Very coarse sand	
1.19		-0.25		
1.00		-0.00		
0.84		0.25		
0.71		0.50	Coarse sand	
0.59		0.75		
1/2 – 0.50	500	1.00		
0.42	420	1.25		
0.35	350	1.50	Medium sand	Sand
0.30	300	1.75		
1/4 – 0.25	250	2.00		
0.210	210	2.25		
0.177	177	2.50	Fine sand	
0.149	149	2.75		
1/8 – 0.125	125	3.00		
0.105	105	3.25		
0.088	88	3.50	Very fine sand	
0.074	74	3.75		
1/16 – 0.0625	63	4.00		
0.0530	53	4.25		
0.0440	44	4.50	Coarse silt	
0.0370	37	4.75		
1/32 – 0.0310	31	5		
1/64 0.0156	15.6	6	Medium silt	
1/128 0.0078	7.8	7	Fine silt	
1/256 – 0.0039	3.9	8	Very fine silt	Mud
0.0020	2.0	9		
0.00098	0.98	10		
0.00049	0.49	11	Clay	
0.00024	0.24	12		
0.00012	0.12	13		
0.00006	0.06	14		

Figure 3.3.: Wentworth grain–size scale for siliciclastic sediment (*Wentworth*, 1922)

3.2.1 Domain

In the regional model, the choices of model domain are basically constrained by following arguments:

- the domain should be large enough to ensure the reality of important dynamic features.

- the domain should be small enough to hold a reasonable computational cost, while high resolution is still desired.

- the steep topography should be kept away from open boundaries. These boundaries should be placed where the topographic gradient perpendicular to the boundary is as small as possible to avoid along–boundary currents. They should also be placed where there is a minimum in current velocities and in variability.

To satisfy these criteria, especially the last term, our model is firstly built in a large region offshore southern Africa, which covers the whole highly variable Agulhas Current system. This domain ranges from 2.5 °W to 54.75 °E and from 46.75 °S to 4.8 °S (Figure 1.2). However, the study area of this thesis, Agulhas Drift and its vicinity, is a relative small region. It is therefore unworthy to use high resolution for the entire field. Within this large domain, the model has a horizontal resolution of 1/4°, which in E–W direction ranges from approximately 19 km in the south to 27.6 km in the north.

On the basis of this large model (also called parent model), it is necessary to embed a model with higher resolution over the region of interest (also named child model), so that a better numerical approach of reality can be obtained. On the other side, computational time should also be saved. In order to achieve both of these objectives simultaneously, the domain of child model is tested in different dimensions (Figure 3.4). The smallest child domain covers only the region of Transkei Basin. The middle–size domain comprises both east and west offshore region off South Africa. The largest domain further expands in north direction. All these child models have the same horizontal resolution of 1/12°. With this higher resolution, we expect to solve the temporal and spatial variability of the flow regime in mesoscale features, e.g. eddies and filaments, in this region (*Lutjeharms*

et al., 1991, 2003; *Biastoch et al.*, 2008a,b). To examine the reality of these child models, their results are compared together with satellite data sets, including sea surface temperature (SST) and sea surface height (SSH) (Figure 3.4). In addition, the model chosen for the nesting procedure in the present simulations is the 1–way embedding technique. It has been proven that the use of this 1–way embedding can strongly enhance the simulation results, although no important discontinuities are visible at the parent–child grid interface (*Penven et al.*, 2006b).

The satellite image of average SSTs is derived from the AVHRR Pathfinder Version 5.0 data from 1985 to 2001. This satellite data set is a new reanalysis of the AVHRR data stream developed by the University of Miami–Rosenstiel School of Marine and Atmospheric Science (RSMAS) and the NOAA National Oceanographic Data Center (NODC). The climatological AVHRR data are available globally at approximately 4 km resolution and accessible via `http://data.nodc.noaa.gov/pathfinder/Version5.0_Climatologies/`.

The comparisons of average SSTs indicate that the representations of child models strongly depend on their scopes (Figure 3.4). A satisfied approach to reality cannot be obtained in the smallest child domain that only covers the Transkei Basin. For instance, the corner of the 20 °C isotherm, which is located south of South Africa, is shifted eastwards in the smallest child model compared to the satellite image. The location of this feature is best represented in the largest child model, while the southern branch of the 20 °C isotherm is shifted northwards comparing to the satellite image. Hence, for the average SSTs, the child model of the middle–size provides closest approach to the observation in general.

Not only the average fields of the child models are examined, the standard deviation of their numerical results are further compared with the satellite measurements. Here, standard deviation of SSH is calculated from the AVISO Rio05 product at 0.5° resolution (*Rio and Hernandez*, 2004) from 14th October 1992 to 1st January 2006 (`http://www.aviso.oceanobs.com/`). The comparisons of the child model results with satellite data indicate again that better simulation

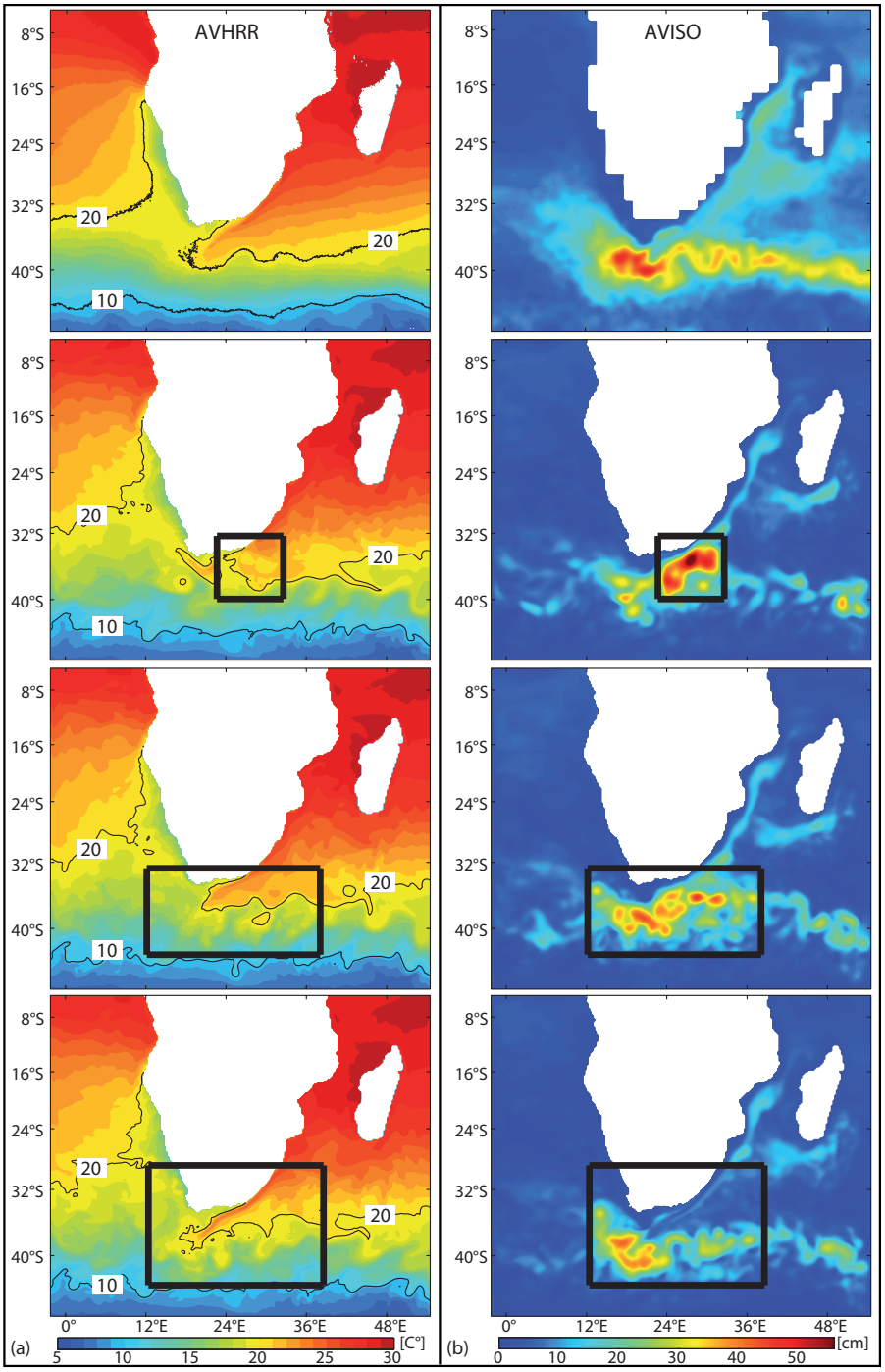

Figure 3.4.: Observations/model comparisons of mean of SST (left) and standard deviation of SSH (right). The simulation results are computed from models with different nesting domains, which are indicated by black frames. The satellite image of SSH is derived from the AVHRR Pathfinder Version 5.0 data. The measured SSH is calculated from the AVISO Rio05 product.

approach can be obtained in the larger child domains (Figure 3.4). In AVISO image, large standard deviations of SSH ($\geq 30\,\mathrm{cm}$) are located in the region south of South Africa and oriented in an approximate east–west direction. In the smallest child model, extreme high standard deviation is falsely represented within its domain. Large standard deviations from the other two child models can be also found in the region south of South Africa. However, their values are slightly lower than those exhibited in the satellite image. Nevertheless, an east–west distribution of high standard deviation is roughly represented within these child domains.

The separate comparisons described above indicate that both east and west offshore region off South Africa must be covered in the domain of the child model. However, the extending of the child domain in north–direction is not necessary. Hence, the middle large domain of the child model, which ranges from 47 °S to 32 °S and from 12 °E to 38 °E is chosen for this thesis (Figures 3.4–3.5). Within this domain, the horizontal resolution of 1/12° decreases southward from approximately 10 km to 8 km. Using this child model, computational time can be kept within a reasonable range on the premise of obtaining a satisfied simulation approach to reality.

For both parent and child domain, 20 vertical layers are used (Figure 3.5). The model bottom topography is interpolated from ETOPO2 (*Smith and Sandwell*, 1997). Based on this bottom topography, the 20 vertical levels are stretched toward the surface as well as the bottom with s–coordinate parameters (see Section 3.1.2): $\theta_s = 4.9$, $\theta_b = 0.9$, $h_c = 5$. Within this stretched grid, the vertical resolution shows non–linear degrading for the uppermost half whereas the resolution increases again further downward (Figure 3.5). The lowest vertical resolution is at intermediate depth and has a value of about 645 m. The high resolution at the surface is essential for simulating the near–surface mixed layer dynamics. For the bottom layer, the suspended sediments are predominantly confined close to the deep sea floor. Note that with the high θ_b, the resolution is still coarse on the bottom of the deep ocean. In particular, the vertical resolutions of the bottom

layer range from 2 m at the continental shelf to 150 m in the deep sea (Table 3.1). It would be better to use more vertical levels to resolve more accurately the bottom layers, but trial model runs with an increased number of vertical levels blow up easily. The simulation interrupts are caused by pressure gradient errors within the thinner steep vertical layers.

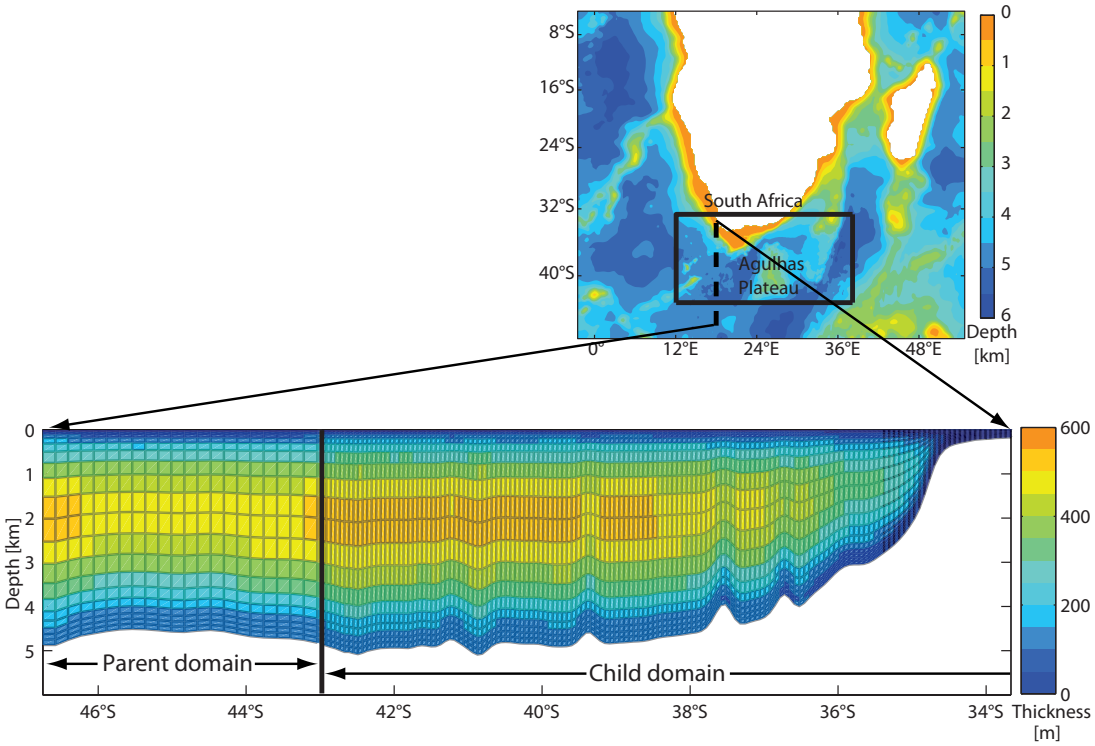

Figure 3.5.: Top: Map of the whole model domain and the nested child model domain (black frame). Bottom: Vertical structure of parent model and child model along 18 °E.

Additionally, for model grid generation, topographic smoothing is an important process to reduce horizontal pressure gradient errors created in s–coordinate (see Section 3.1.2). In the models of this thesis, the model topography (h derived from ETOPO2–data) is slightly smoothed using the selective Shapiro filter to keep the topography parameter (r in Eq. 3.22) below 0.25. In our model grids, especially in the lower-resolution parent domain, the isobaths are smoothed and many small details exhibited in ETOPO2 are removed (Figure 3.6).

Table 3.1.: Vertical s–coordinate system: depth in meters of the s levels. The other variables are at intermediate levels.

Level	at $h_{\min}$	over the slope	at $h_{\max}$
20	0.0	0.0	0.0
19	−0.571	−13.478	−26.386
18	−1.325	−34.472	−67.619
17	−2.367	−67.374	−132.380
16	−3.857	−118.727	−233.596
15	−6.019	−197.741	−389.462
14	−9.137	−316.152	−623.167
13	−13.512	−486.332	−959.151
12	−19.340	−716.415	−1413.490
11	−26.537	−1002.864	−1979.191
10	−34.600	−1324.998	−2615.397
9	−42.699	−1648.623	−3254.548
8	−50.006	−1939.633	−3829.259
7	−56.026	−2177.622	−4299.218
6	−60.685	−2359.530	−4658.374
5	−64.198	−2494.200	−4924.202
4	−66.888	−2594.983	−5123.078
3	−69.073	−2674.929	−5280.786
2	−71.017	−2744.973	−5418.930
1	−72.933	−2813.899	−5554.864
0	−75.000	−2888.990	−5702.979

3.2.2 Forcing, Climatology and Initial Conditions

After the gridding process, the forcing, boundary, and initial conditions are prepared within the structured grids as the next procedure. Since we want to observe the influence of the ocean currents on the sediment transport patterns over a relative long period, two climatological datasets are used to derive input fields.

The forcing fields are combined with momentum forcing, thermal forcing and fresh water flux (Eq. 3.8–3.12). Within both parent and child domain, the forcing fields of our simulations are derived from a monthly climatological dataset, Comprehensive Ocean-Atmosphere Data Set (COADS) , a monthly climatology data with 0.5° resolution ($\sim$ 48 km) (*da Silva et al.*, 1994). As shown in Eq. 3.8–3.9, the momentum forcing is given by the longitudinal and latitudinal components of

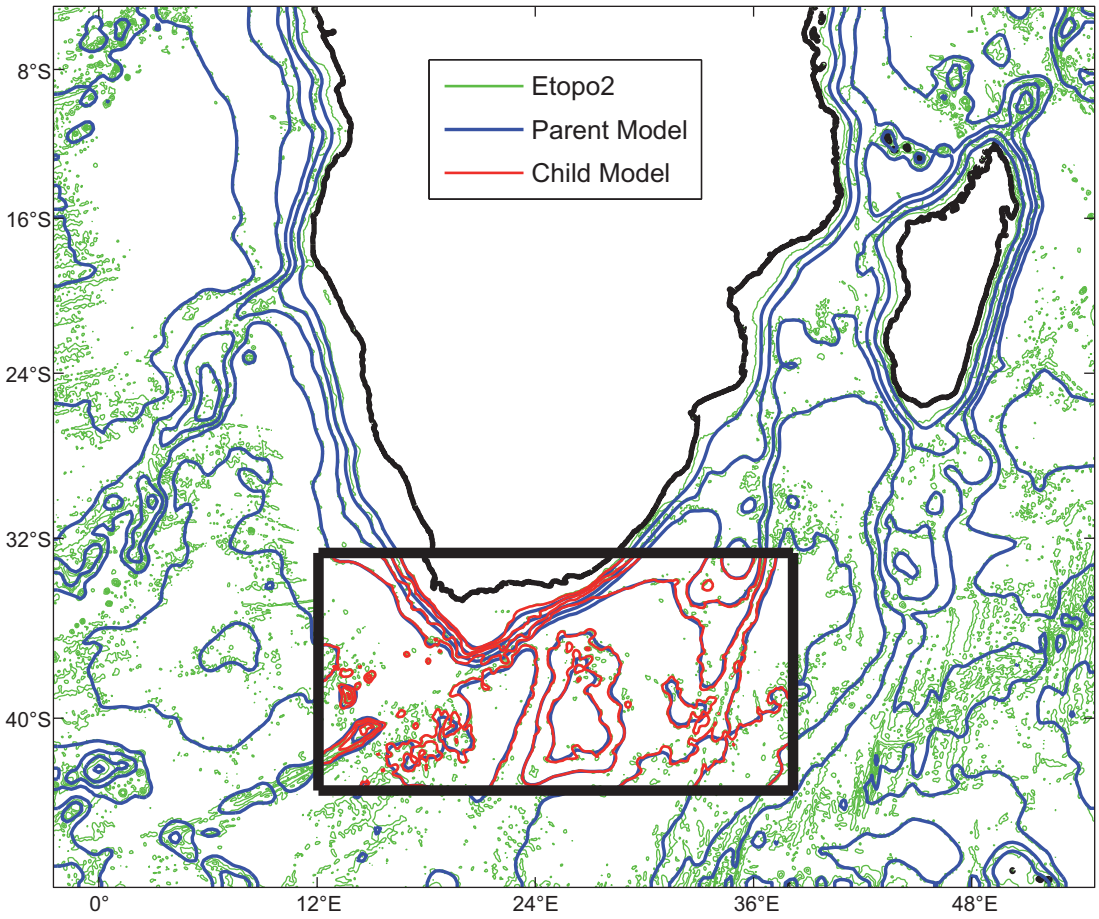

Figure 3.6.: Comparisons of isobaths from the raw Etopo2 data set with those from models after smoothing. The interval between the isobaths is 1000 m.

the wind stress. Four examples of wind fields for different seasons are presented in Figure 3.7. One can note seasonal changes in wind field in the Transkei Basin. In summer (e.g. on model day 195), wind stress is strong in Transkei Basin, where the major direction of wind stress is eastward. Besides, thermohaline forcing is another important term for the surface fields (Eq. 3.10). It is specified as net heat flux derived from the COADS data set (Figure 3.8). In the region of Agulhas Retroflection (roughly from 12 °E to 24 °E and from 42 °S to 34 °S, more details see Chapter 1, p. 2), the net heat flux is negative throughout the year.

For the boundary conditions, as mentioned in Section 3.1.1, ROMS has an option for providing radiation conditions on outflow and nudging to a known exterior value on inflow (*Marchesiello et al.*, 2001). Along the lateral boundaries of

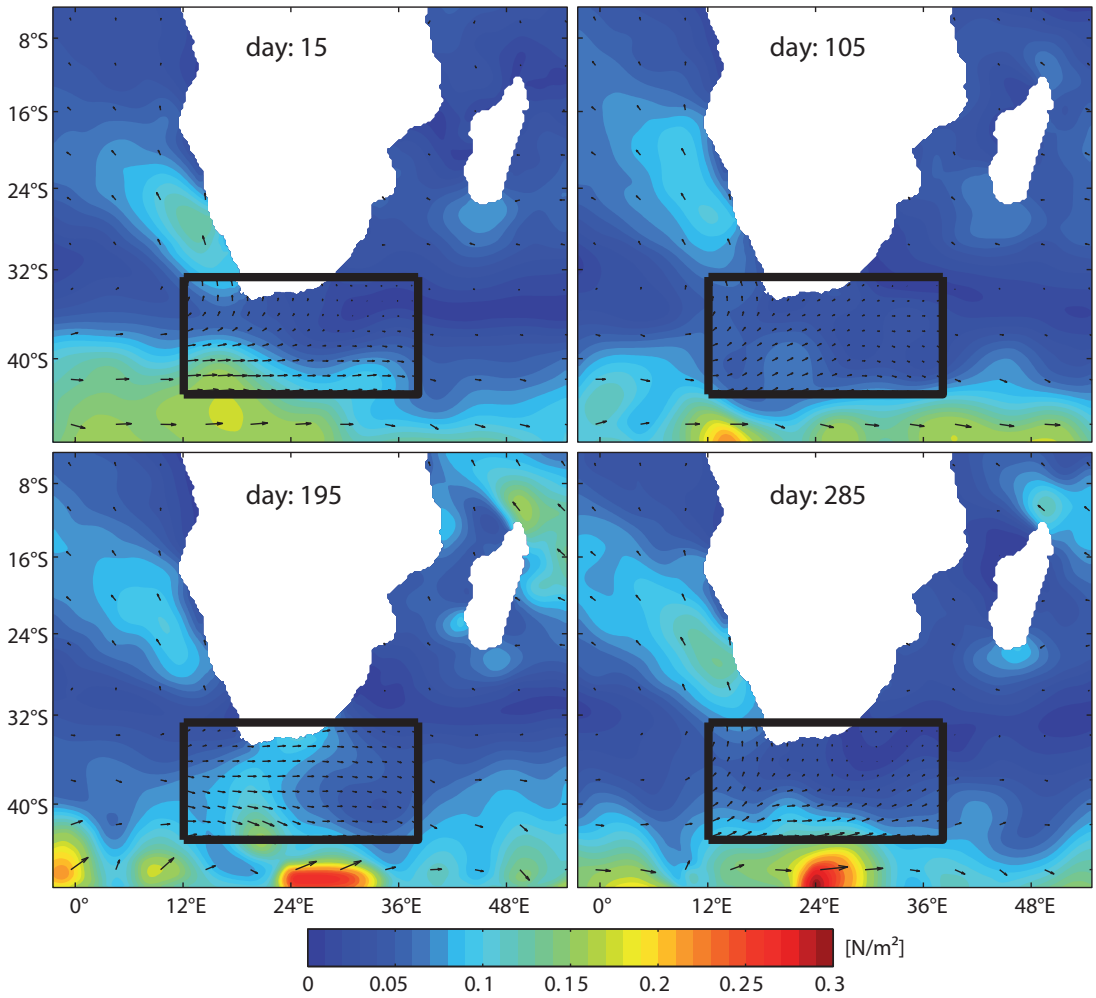

Figure 3.7.: Examples of wind stress based on the COADS monthly climatology data (1 vector is portrayed every 20 vectors)

the parent domain, temperature and salinity are nudged towards the climatological values from the monthly climatology of the World Ocean Atlas 2005 (WOA 2005) (*Locarnini et al.*, 2006). The WOA data and COADS winds are further combined to estimate geostrophic and Ekman velocity components at all these boundaries. For the child model, the lateral boundary conditions are provided by the parent grid.

The entire model is initiated with WOA data of January and no flow. Additionally, the entire configurations for these data sets and their corresponding nesting data sets are processed using ROMSTOOLS (*Penven et al.*, 2008).

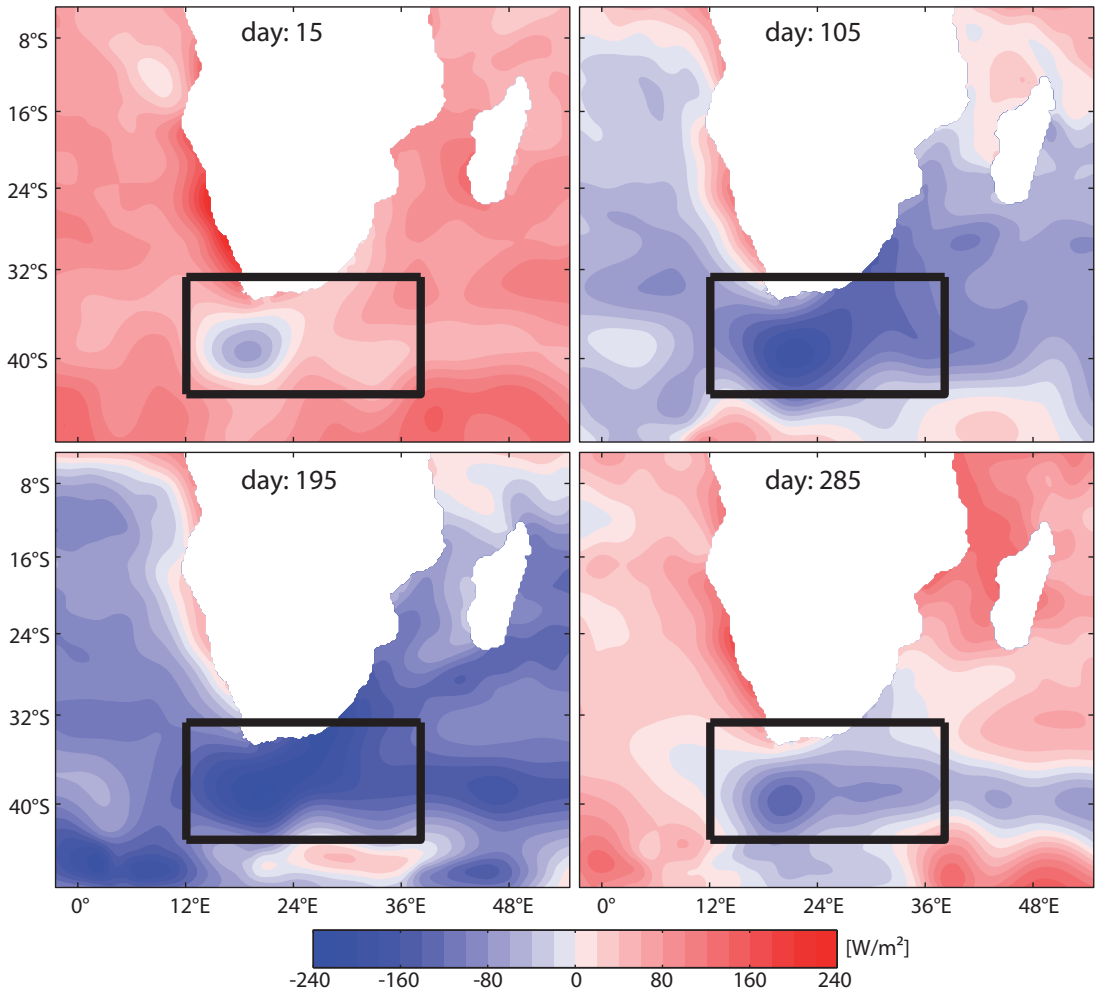

Figure 3.8.: Examples of net heat flux based on the COADS monthly climatology data

3.2.3 Test of Different Sediment Grain Sizes

Since the grain sizes composing the Agulhas Drift are unknown, sediment transport patterns of silt were investigated exemplarily. Many case studies indicated that the grain size of elongate mounded sediment drifts vary from mud to silt as a result of long–term fluctuations in bottom current strength (*Dingle and Camden-Smith*, 1979; *Dingle and Robson*, 1985; *Stow et al.*, 2002). Therefore, coarser sediments are not considered in this study. Four different sediment grain sizes in the range of silt are tested refering to classification of *Wentworth* (1922) (see Section 3.1.3).

In our present simulations, these sediments are specified as different grain size

diameters (d_j): silt1 (coarse silt, $d_1 = 0.0310\,\mathrm{mm}$), silt2 (medium silt, $d_2 = 0.0156\,\mathrm{mm}$), silt3 (fine silt, $d_3 = 0.0078\,\mathrm{mm}$), and silt4 (very fine silt, $d_4 = 0.0039\,\mathrm{mm}$) respectively. They are calculated separately as noncohesive sediments. For different silt size classes, their specific sediment parameters mentioned in Section 3.1.3 are listed in Table 3.2. Additionally, the porosities are set to 0.4, and the densities are given as $2650\,\mathrm{kg\,m^{-3}}$. The same values were successfully used by *Blaas et al.* (2007) and *Warner et al.* (2008b,a) to simulate sediment transport patterns in other regions.

Gross and Dade (1991) indicated that materials, which are suspended by strong turbulences in the abyssal ocean, act as a major sediment source. In order to examine the potential sediment sources due to erosion, two procedure steps are carried out: (1) initial concentrations of the four silt classes are set to $0\,\mathrm{mg\,l^{-1}}$ in each grid cell in the water columns; (2) sediments, which can be eroded and entrained into water columns by simulated currents in the each grid at the ocean bottom, are computed according to Eq. 3.26–3.29 after the onset of our simulations. Additionally, river input and other sediment sources are not taken into account in this study.

3.2.4 Simulation Procedures

Our model is firstly spun up for 2 years to reach equilibrium, as it has been shown that ROMS can reach statistical equilibrium after being run for a period of 2 years (*Karakas et al.*, 2006; *Penven et al.*, 2001). Afterwards, we run our simulations

Table 3.2.: Sediment parameters (For explanation see Section 3.1.3). d_j: Diameter of grain size class; w_{sj}: Settling velocity of size class; E_{uj}: Erosion rate of size class; $\tau_{cr,j}$: Critical shear stress for sediment motion.

	d_j [mm]	w_{sj} [$\mathrm{mm\,s^{-1}}$]	E_{uj} [$\mathrm{kg\,m^{-2}\,s^{-1}}$]	$\tau_{cr,j}$ [$\mathrm{N\,m^{-2}}$]
silt1	0.0310	0.605	1.60×10^{-5}	0.08
silt2	0.0156	0.153	0.41×10^{-5}	0.05
silt3	0.0078	0.038	0.10×10^{-5}	0.03
silt4	0.0039	0.010	0.03×10^{-5}	0.02

for 3 additional years to examine the reality of our model and to observe the hydrodynamic features in our study area. On the basis of these simulations, the sediment transport model is further carried out simultaneously with the ocean circulation model from the 6th to 9th model year (see Chapter 1,p. 8).

4

Model Comparisons with Field Observations

After the model configurations are applied, the approach of these simulations is examined by comparison with observations in this chapter. The results both from the parent model and child model (Figure 4.1) are firstly compared with images derived from different remote datasets (in section 4.1–4.2). By comparative analysis, the representation of ocean currents in the surface layer is observed. In order to further test the performance of the simulations at abyssal depths, direct measurements of vertical profiles offshore South Africa (Figure 4.1) are compared with the simulation results of the child model (Section 4.3–4.4).

4.1 Sea Surface Temperature

Simulated Sea Surface Temperatures (SSTs) from our models are compared with measured SSTs, because SST contrasts are high in this area, and hence the Agulhas Current can be easily identified by the surface thermal expression (*Lutjeharms*, 2006). The satellite images are derived from the AVHRR Pathfinder Version 5.0 data from 1985 to 2001, which are used for determining the child model domain in Section 3.2.1. Note that the climatological AVHRR data have a global resolution of approximately 4 km.

In Figures 4.2a–c, simulated spring SSTs averaged from March to May over 3 model years are compared with a satellite image of SSTs for the same season. In both, satellite data (Figure 4.2a) and our simulation(Figures 4.2b–c), the warm Agulhas Current with SST over 20 °C is found along the south east continental

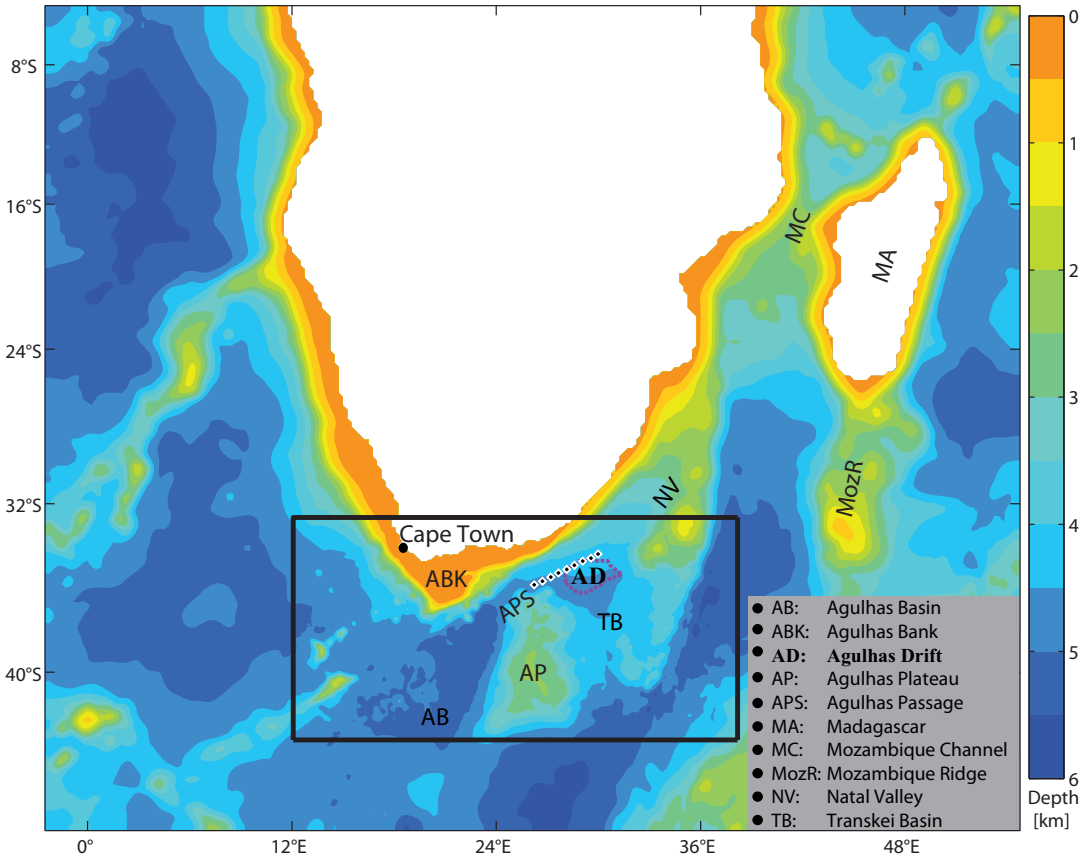

Figure 4.1.: Map of the entire model domain. The nested child model domain is indicated by the black frame. The locations of LADCP/CTD stations of AUCE carried out in February 2003 are marked by white diamonds with solid black dots. These CTD and LADCP profiles are compared with the simulation results in Figures 4.5–4.6. Computed boundary of the Agulhas Drift (*Schlüter and Uenzelmann-Neben*, 2008) is marked as in Figure 1.2.

shelf offshore South Africa.

The locations of the Agulhas Current Retroflection can be roughly monitored by the 20 °C isotherm southwest of South Africa. The loop of the retroflection in the parent model (Figure 4.2b) is shifted north–westwards compared to the satellite data (Figure 4.2a). However, this feature is improved by the child model (Figure 4.2c).

Above the Agulhas Plateau, the satellite data show that SSTs are lower than that east and west of it (Figure 4.2a). This wide north–south meander is indicated by the 20 °C isotherm. The field observations of *Boebel et al.* (2003) pointed out

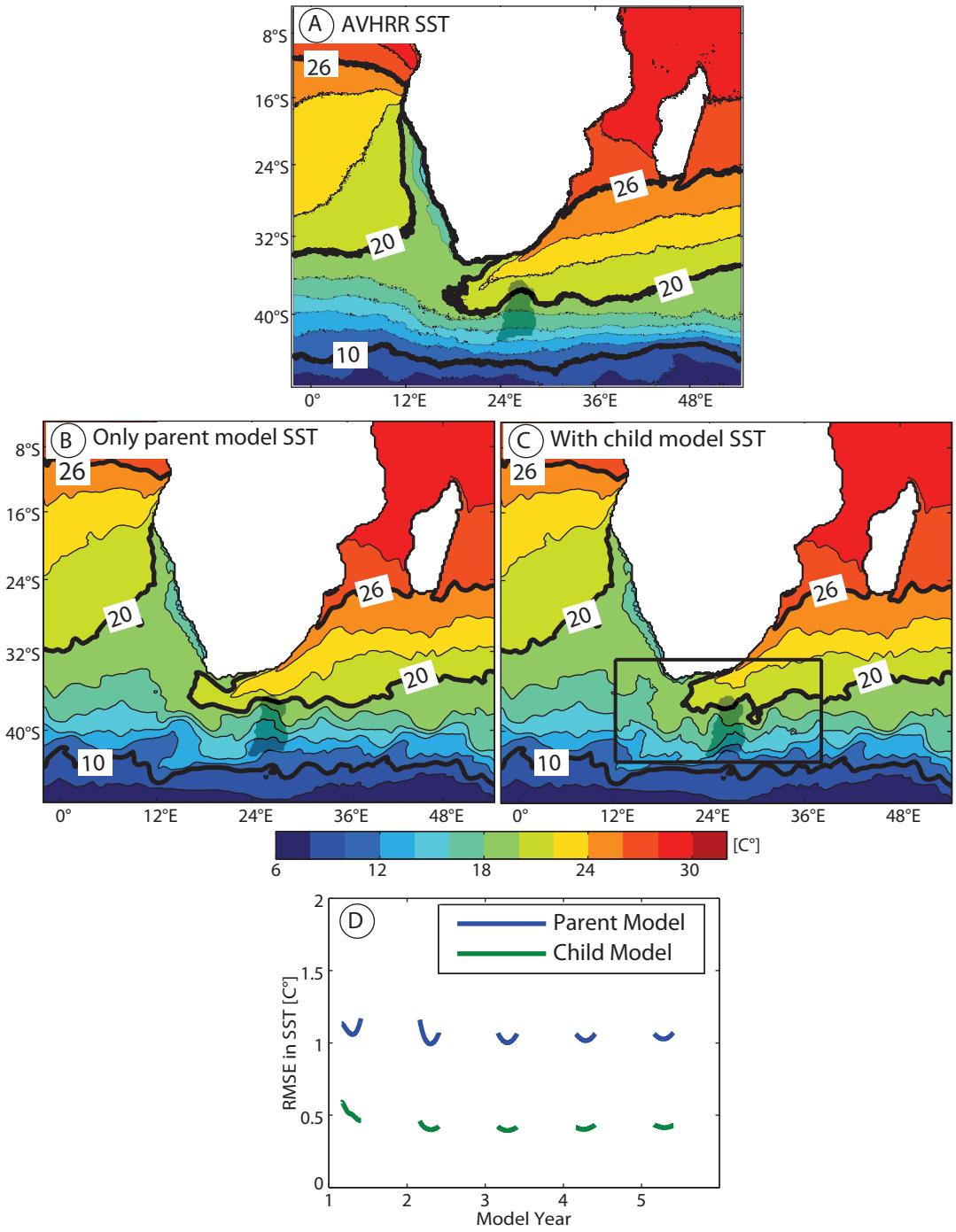

Figure 4.2.: Observations/model comparisons of averaged SST (a–c) and time evolution of RMSE in SST(d). The SST satellite image is derived from the AVHRR Pathfinder Version 5.0 data. In Figures a–c, grey shadow indicates the position of the Agulhas Plateau.

that this feature is a near–permanent northward meander of the Agulhas Return Current, and it is produced by the bathymetric structure of the Agulhas Plateau, which rises ≈ 3000 m from the sea floor. The center of this meander in the satellite image is found approximately along 28 °E in the region slightly east of the central point of the Agulhas Plateau (Figure 4.2a). The meander and its center are not well reproduced in the parent model due to the low resolution (Figure 4.2b). In the child model, the meander feature is better imaged, although the center of this meander shifts slightly eastward (Figure 4.2c).

Root Mean Square Errors (RMSEs) (see Appendix A) in SSTs between the satellite data and simulation results are calculated to obtain a view of error levels. Figure 4.2d shows the time evolution of the RMSE in the parent and child domains during the springs of 5 years. The RMSEs change slightly with time because of the interseasonal variations. The errors are about 1.2 °C for the parent model, and 0.5 °C for the child model (Figure 4.2d). The match between simulated SSTs of the child model and measured field data is much better compared to those of the parent model.

Summarizing, in both model domains general distribution and magnitude of SSTs fit with field observations. Therefore, our simulations have the capability to simulate the Agulhas Current, the Agulhas Retroflection as well as of the Agulhas Return Current with the larger scale meander as the most important surface currents off southern South Africa.

4.2 Sea Surface Height and Eddy Kinetic Energy

In order to further test the capability of our hydrodynamic modeling, our simulations are compared to measured sea surface height (SSH) in Figures 4.3a–c and the surface eddy kinetic energy (EKE) derived from SSH anomalies in Figures 4.4a–c, as other independent data sets. SSH roughly resolves the geographic location of the Agulhas Current system, and EKE further reveals its mesoscale variability. Measured mean SSH is calculated from the AVISO Rio05 product at

0.5° resolution (*Rio and Hernandez*, 2004) from 14th October 1992 to 1st January 2006. The same data are also used in Section 3.2.1 to examine the approach of the child models with different dimensions. Using AVISO SSH, EKE is computed according to the studies of *Ducet et al.* (2000) and *Jordi and Wang* (2009) (see Appendix B).

The geographic location and the trend of the Agulhas Current are associated with positive SSH. The Agulhas Current represented by the SSH contours in both satellite image and simulation results are quite similarly (Figures 4.3a–c). However, the simulated Agulhas Retroflection loop is shifted slightly northwestward in our simulations compared to AVISO. In addition, the oscillation of the Agulhas Return Current presented by AVISO SSH contours is more distinct than that from our simulations. Nevertheless, these biases are significantly improved in the child model compared to its parent model (Figures 4.3a–c).

The RMSEs in SSH between simulation values and field observations quickly converge to a constant value. The RMSE for the parent model is steady at about 12 cm, and the error for the child model is around 6 cm, only half of that of the parent model. This again confirms the improved performance of the child model.

In the region of the Agulhas Retroflection, the highest mean AVISO EKE is found with values greater than $3000\,\mathrm{cm^2\,s^{-2}}$ (Figure 4.4a). Although this characteristic area is not distinguished in the parent model (Figure 4.4b), it is similarly resolved in the child model (Figure 4.4c). In addition, another area with high variability (larger than $2000\,\mathrm{cm^2\,s^{-2}}$) is shown in the region of the Agulhas Return Current (Figure 4.4a). Once again, the averaged EKE from the parent model in this region is lower than that from the satellite data. For the child model, the area with EKE greater than $2000\,\mathrm{cm^2\,s^{-2}}$ is smaller than that shown by AVISO EKE due to the limitation of the child domain. However, in our area of interest, the region of the Agulhas Drift, the range of simulated variability in EKE is substantially similar to that derived from AVISO data set (Figures 4.4a and c).

Unlike the RMSEs in SSH for the parent model and child model converge to

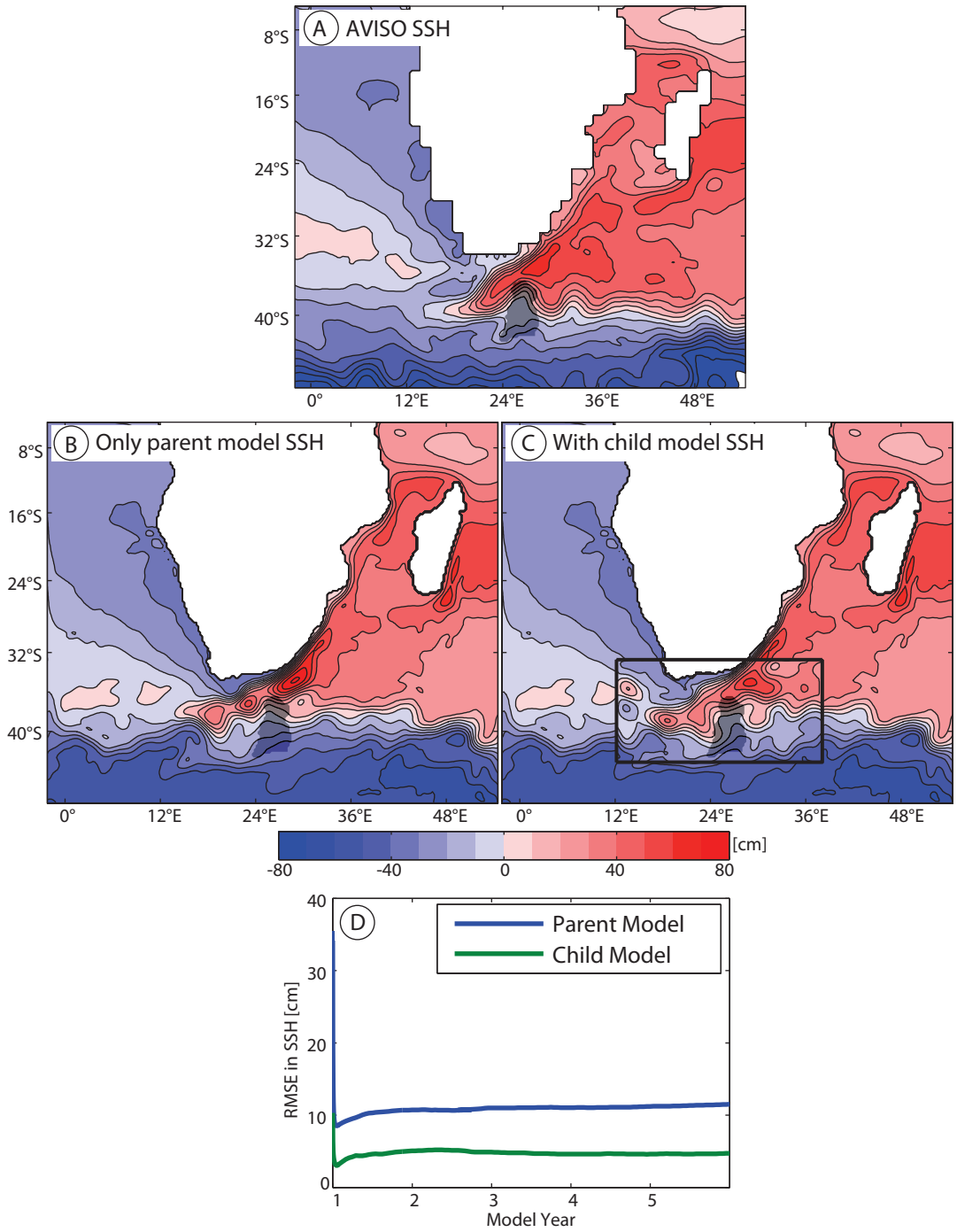

Figure 4.3.: Observations/model comparisons of averaged SSH (a–c) and time evolution of RMSE in SSH(d). The satellite image of SSH is calculated from the AVISO Rio05 product. The interval between the isocontours for SSH is 10 cm. Otherwise like Figure 4.2.

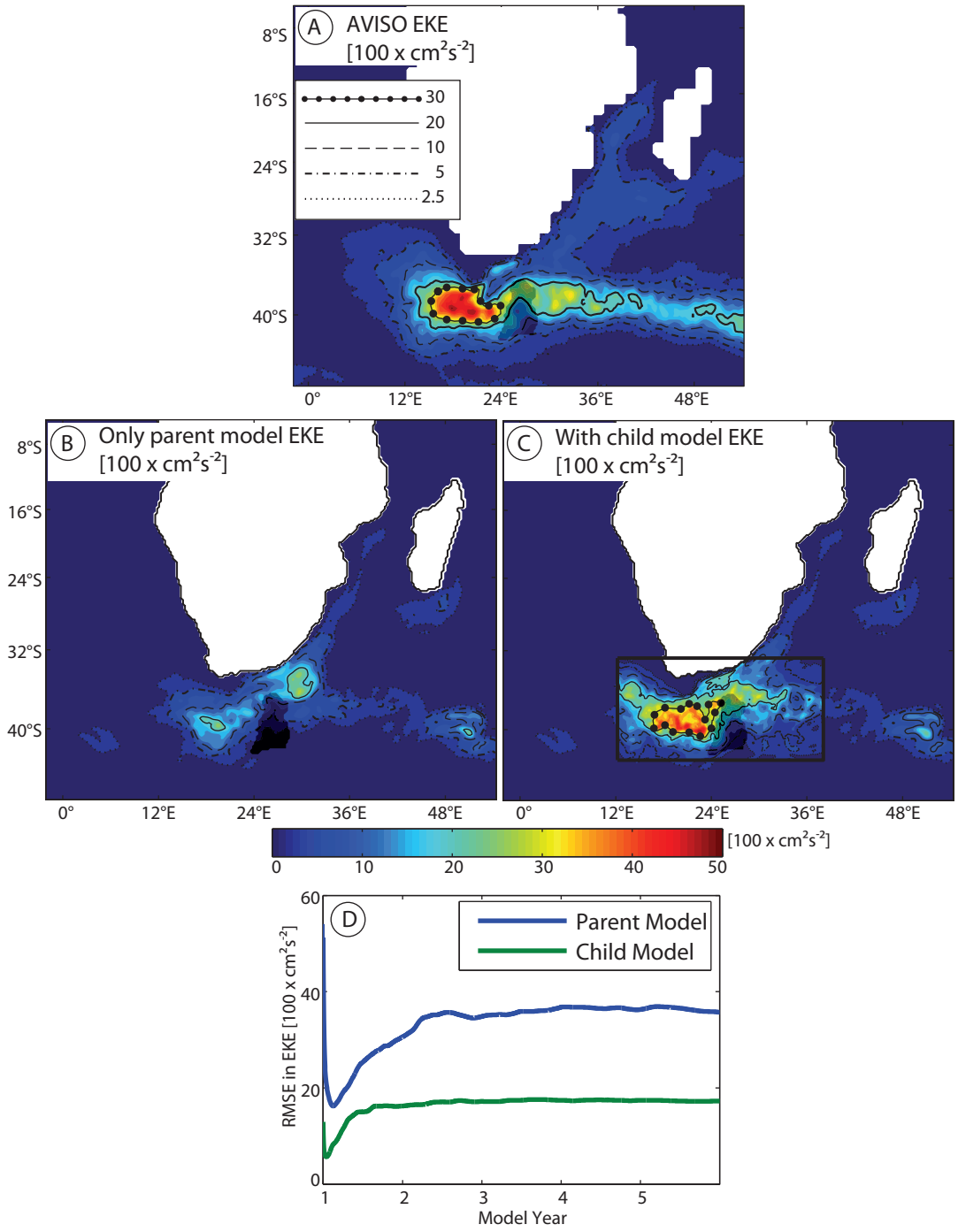

Figure 4.4.: Observations/model comparisons of EKE (a–c) and time evolution of RMSE in EKE(d). The measured EKE is derived from the AVISO Rio05 product. Otherwise like Figure 4.2.

the constant values simultaneously, RMSE in EKE of the child model decreases more rapidly than that of the parent model. On the other hand, the constant

error in EKE of the child model is about half of that of the parent model. This once again strongly proves the necessity of the nesting.

4.3 Vertical Salinity Profile

As an additional method to verify our model, we compare the vertical salinity structure of the simulated data to CTD (Conductivity Temperature Depth) data (Figure 4.5). These data were gathered out during the Agulhas Under Current Experiment (AUCE) in February 2003 (Figure 4.1) (*Bryden et al.*, 2005). The vertical resolutions of both datasets are different as AUCE data are available with a vertical spacing of 10 m whereas our simulations deliver current velocities at 20 depths layers of different thicknesses (Figure 3.5).

A water mass with high salinities (larger than 34.9 psu) is found in the surface layer ($\leq$ 1000 m) in both the simulated as well as measured salinities (Figure 4.5). According to studies from this region (e.g. *Lutjeharms and van Ballegooyen*, 1988; *Lutjeharms*, 2006), this high salinity typifies the Agulhas Current.

Underlying this water mass, in the depth range between 1000 m to 2000 m, the salinities are generally lower ($\leq$ 34.6 psu) compared to surrounding water masses in both datasets (Figure 4.5). This water mass can be identified as Antarctic Intermediate Water (AAIW) in the southwest Indian Ocean based on the study of e.g. *van Aken* (2000) and *You et al.* (2003). AAIW salinity recorded from CTD measurements is lower than that simulated by our model (Figure 4.5). This difference results from the low vertical resolution (about 350 m) within this depth level in our model (Figure 3.5). However, the depth range and the general salinity trend of this water mass correlate with AAIW in nature. Below this layer, between approximately 2000 m and 3500 m, a water mass with salinities about 34.8 psu is observed in both CTD measurements and simulations (Figure 4.5). This water mass can be interpreted as NADW (*Toole and Warren*, 1993; *van Aken et al.*, 2004). Furthermore, a thickening of the NADW layer has been observed at station 18 during the AUCE field experiment (Figure 4.5a). This feature has

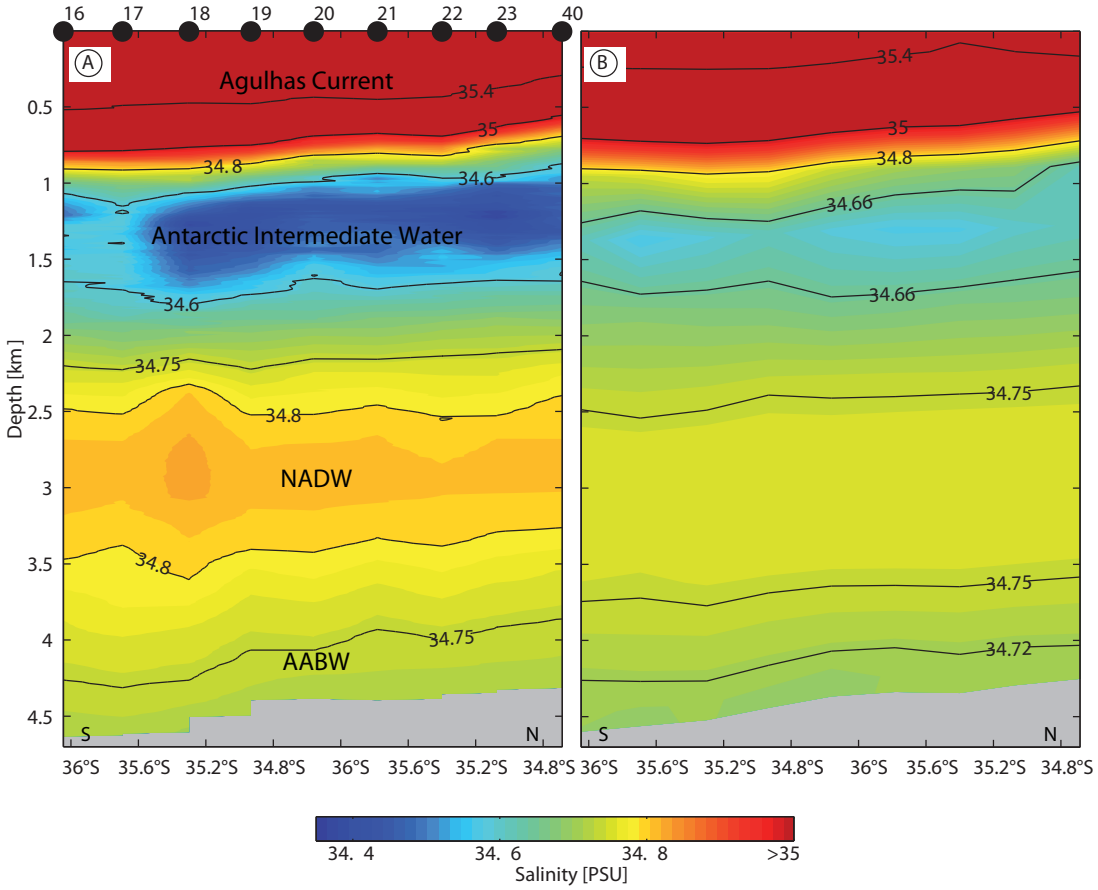

Figure 4.5.: Observations/model comparison of salinities in the vertical direction. (a) Salinity section from the CTD measurements of the AUCE. The locations of AUCE measurements are depicted in Figure 4.1. The station positions from AUCE are marked as black dots. (b) A snapshot of the salinity section on 4th February of the 5th model year of the child model.

been interpreted as an NADW eddy by *Casal et al.* (2006). A similar concave–convex lens–shaped structure caused by thickening of NADW can be found in our model data at the depth of $2500 - -4000$ m, but is much less pronounced (Figure 4.5b). Close to the sea floor (≥ 3500 m), salinities are about 34.7 psu at both cross sections. According to the studies of *Mantyla and Reid* (1995), *Boswell and Smythe-Wright* (2002) and *Boswell et al.* (2002), AABW in the southwest Indian Ocean has salinities of 34.66 to 34.75 psu from 3500 m to the bottom. We thus interpret this simulated water mass as AABW.

In short, modeled salinities and those from CTD measurements have a simi-

lar stratification (Figure 4.5). Identical water masses (Agulhas Current, AAIW, NADW and AABW) with respect to salinities and depth levels could be identified both in the measured and modeled data. Additionally, mesoscale variability of these main hydrographic features, e.g. eddy, can be modeled.

4.4 Vertical Current Profiles

Lower Acoustic Doppler Current Profiler data (LADCP) are another independent recorded parameter which can be compared to the simulated currents (Figure 4.6). These data were also collected during the AUCE (Figure 4.1).

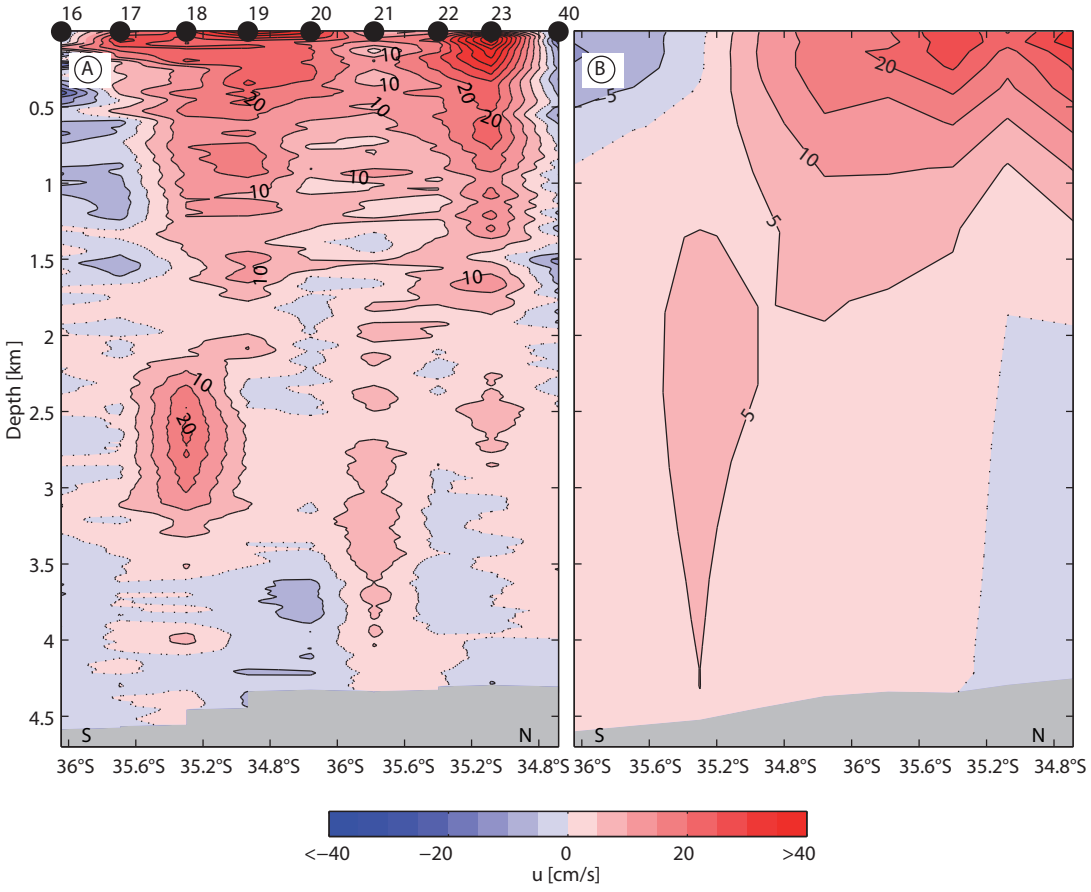

Figure 4.6.: Observations/model comparison of velocities in the vertical direction. (a) Velocity section from LADCP measurements of the AUCE. The locations of AUCE measurements are depicted in Figure 4.1. Velocities are positive (red) in direction towards the coast, which is perpendicular to the section. (b) A snapshot of velocity section from the child model on 4th February of the 5th model year of the child model.

The measured velocities of the Agulhas Current are larger than $15\,\mathrm{cm\,s^{-1}}$. Such high velocities are also shown in our simulations for the Agulhas Current (Figure 4.6). Below the Agulhas Current ($\geq 2000\,\mathrm{m}$), velocities decrease downward to values mostly lower than $5\,\mathrm{cm\,s^{-1}}$ except for the area of NADW eddy, which is revealed in salinity profiles in the last section, both in LADCP data and in simulations, which range from about 2000 to $\geq 3500\,\mathrm{m}$, between $35.6\,^{\circ}\mathrm{S}$ and $34.8\,^{\circ}\mathrm{S}$ (Figure 4.6). In the area of the NADW eddy, higher velocities ($\geq 10\,\mathrm{cm\,s^{-1}}$) are observed during AUCE. Only the seaward branch of the NADW eddy, which is interpreted as the outer edge of the eddy (*Casal et al.*, 2006) is monitored (Figure 4.6a). A similar feature can be observed in our simulations (Figure 4.6b). This simulated eddy occurs over a period of approximately two weeks and is located in almost the same latitude as shown by the LADCP (Figure 4.6). The comparison shows that our simulations have the capability to simulate variability in the deep ocean (like NADW eddy) as well as at the sea surface. The simulated velocity of this eddy event ($\approx 5\,\mathrm{cm\,s^{-1}}$) is much lower than that measured in situ (Figure 4.6b). This discrepancy and the difference in eddy depth range are caused by the low resolution of our model in this particular depth level as mentioned above. Nevertheless, since we focus on hydrodynamic processes and sediment transport patterns in only a few layers (i.e. $\approx 400\,\mathrm{m}$) above the sea floor, this discrepancy is in an acceptable range.

Im summary, SST, SSH and EKE, the vertical sections of salinities and velocities further confirm the high quality of our ROMS model, especially that of the nested child model. These different parameters substantiate that the complex current system offshore south of South Africa at the sea surface as well as in deeper sections and along the bottom layer can be simulated realistically. Furthermore, the mesoscale eddy variability observed by CTD and LADCP data are represented in the child model. Hence, our simulations in the child domain allow us to identify and quantify the key role of different ocean currents as potential triggers for the sediment transport into the Transkei Basin.

5

Ocean Circulation South of South Africa

The simulation results of the ocean circulation model from the 3rd to 5th model year are used not only to checked the simulation approach to the nature, but also to observe the important hydrodynamic processes at the Agulhas Drift (Chapter 1, Figure 1.4). Since we are only interested in the current system in the region of the Agulhas Drift and its vicinity, the model results of the child model are analyzed in the area from 40 °S to 33 °S and from 23 °E to 33 °E (Figure 5.1).

5.1 Velocity Field in the Transkei Basin

In order to obtain a 3D view of the circulation patterns in the Transkei Basin, the mean and the standard deviation of the velocity fields at 3 different s–layers (Figure 5.1) are initially observed.

A strong velocity field is shown in the bottom layer (i.e. $s = 1$) (Figure 5.2). Starting from the north, a southwest flowing current can be identified along the 500 m isobath. Both direction and location indicate that the current represents the Agulhas Current on the continental shelf (*Lutjeharms*, 2006). Within the core of this Agulhas Current, the mean velocities are up to $12\,\mathrm{cm\,s^{-1}}$. Further downward between approximately 1000 m and 2000 m water depth along the continental slope, a current flows in the opposite direction and transports water from the Atlantic into the Indian Ocean. Using the current direction and its position again, the water mass of this inflow is suggested to be NADW. The averaged velocity of this slope parallel NADW inflow has a maximum of $7\,\mathrm{cm\,s^{-1}}$. Further offshore

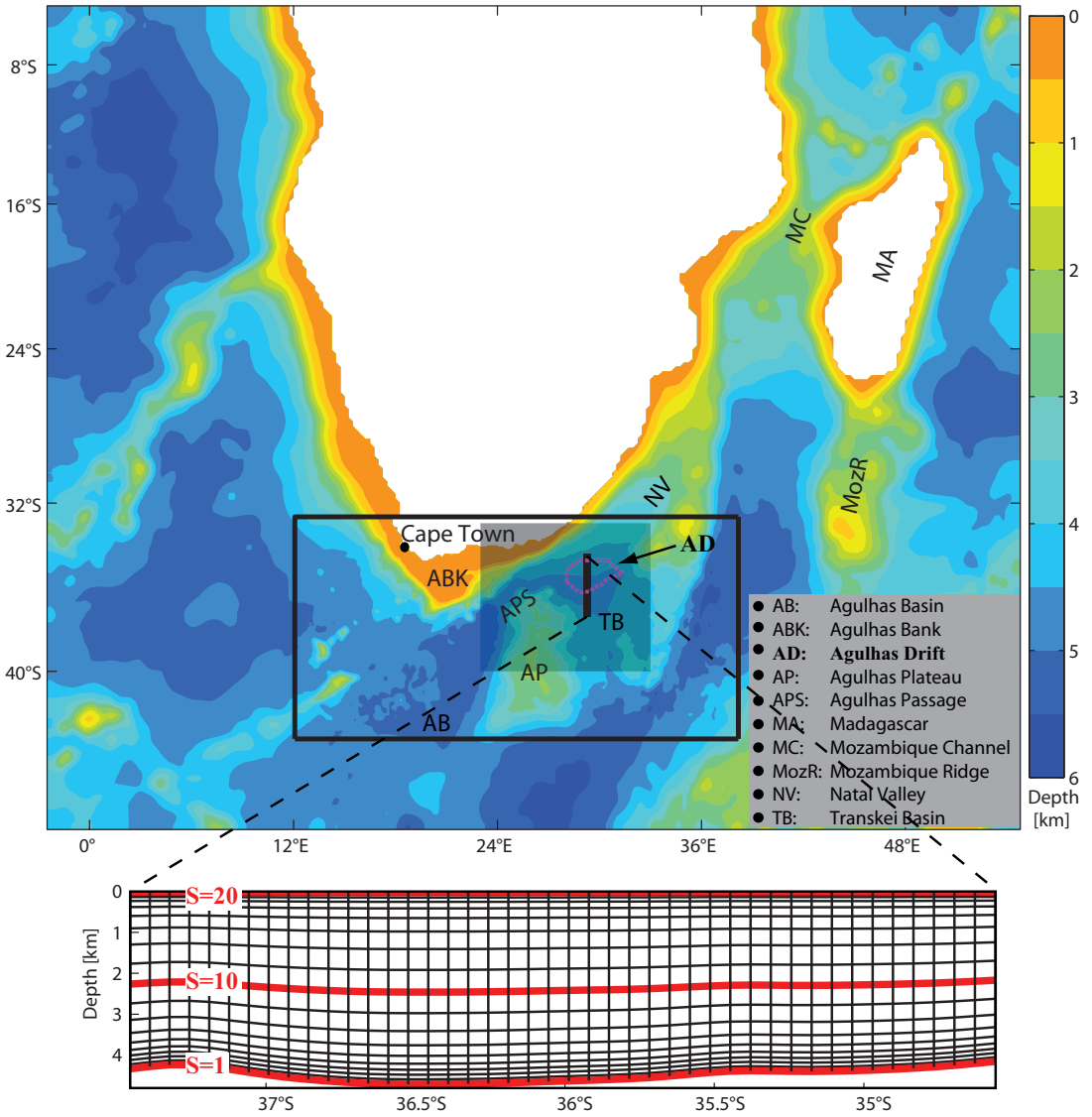

Figure 5.1.: Top: Map of the entire model domain and the nested child model domain (black frame). The grey transparent rectangle marks the area observed in Figure 5.2–5.3. The thick solid line labels the position of the Hovmöller diagrams in Figure 5.4 and velocity sections in Figure 5.5. Computed boundary of the Agulhas Drift (*Schlüter and Uenzelmann-Neben*, 2008) is marked as in Figure 1.2. Bottom: Vertical structure of the child model along 29.25 °E. The red lines indicate the positions of the *s*–levels, at which the velocity fields are revealed in Figures 5.2– 5.3.

within the Agulhas Passage, between the two 4000 m isobaths, the water mass could be interpreted as AABW on the basis of the study of *Camden-Smith et al.* (1981). In the northern part of the Agulhas Passage, AABW flows eastward while it flows generally in the opposite direction from the Transkei Basin to the Agulhas

Basin through the southern part of the Agulhas Passage. The mean speed of the eastward AABW flow is lower than that of the opposed oriented AABW.

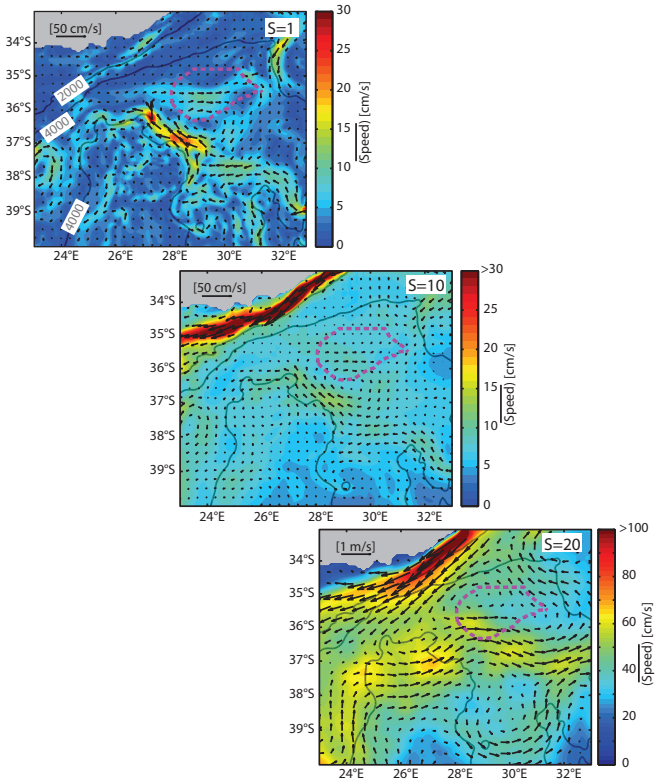

Figure 5.2.: The averaged velocity fields in the layers $s1$, $s10$ and $s20$ from the 3rd to 5th model years. The positions of these layers are marked in Figure 5.1. 1 vector is portrayed every 4 vectors. The grey lines mark the isobaths. Computed boundary of the Agulhas Drift (*Schlüter and Uenzelmann-Neben*, 2008) is marked as in Figure 5.1.

East of the Agulhas Passage, the simulation shows a cyclonic vortex movement in the average of the velocity field near the bottom in the Transkei Basin (Figure 5.2). Because the depth in this region is greater than 4000 m, only AABW can dominate this cyclonic movement (*Mantyla and Reid*, 1995; *Boswell and Smythe-Wright*, 2002; *Boswell et al.*, 2002). The center of this vortex of AABW is located at approximately 36.45 °S and 29.25 °E. It extends ≈ 210 km in north–south direction, and ≈ 350 km east-westward. Within the vortex, the highest averaged velocities of up to 29.6 cm s^{-1} can be found within its southwestern segment close to the northeastern flank of the Agulhas Plateau. For the remaining area, values up to 15 cm s^{-1} are reached. Most importantly, the northern segment of this vortex sets eastward and crosses the steep southern flank of the Agulhas Drift between 35.5 °S and 36.5 °S. In addition, south of 37.5 °S, the averaged velocities of its southern segment flow mainly westward (Figure 5.2).

The cyclonic vortex movement, which is shown in the central Transkei Basin in the bottom layer, is presented in the layer $s10$ as well (Figure 5.2). Note that he depth of this layer is approximately 2000 m (Figure 5.1) in the Transkei Basin. In this layer, the velocity field of the vortex movement is more homogeneous comparing to that in the bottom layer. The velocities along the northeast flank of the Agulhas Plateau are not much greater than the velocities in the other part of the outer edge of the vortex in the layer $s10$. Additionally, the velocities along the northeast flank of the Agulhas Plateau are less than those in the bottom layer of about $10\,\mathrm{cm\,s^{-1}}$. Except for this area, the velocity field of the vortex movement at $s10$ layer is quite similar to that at the bottom.

At the sea surface ($s = 20$), no vortex movement is observed in the mean velocity field in the Transkei Basin (Figure 5.2). In the location, where the vortex movement are presented in the $s1$ and $s10$ layers, a strong current eastward winds into the Transkei Basin. According to the direction and the location of this current, it is interpreted as Agulhas Return Current (*Quartly and Srokosz*, 1993; *Boebel and Barron*, 2003). It is indicated that under the unstable Agulhas Return Current, there is a large vortex movement in the averaged velocity filed extending from the ocean bottom to at least middle depth of the Transkei Basin.

Additionally, the standard deviations of these velocity fields at these 3 s–layers are further observed (Figure 5.3). High standard deviations (up to $44\,\mathrm{cm\,s^{-1}}$) are found at the sea surface in the Transkei Basin, south of the region of the Agulhas Drift. By contrast, the variations of the velocity field in layers $s10$ and $s1$ are much lower. The standard deviations at the ocean bottom are higher than those at the depth of about 2000 m, except for the region along the northeast flank of the Agulhas Plateau. In short, in the Transkei Basin, the current is very unstable at the sea surface, and is relatively active at the ocean bottom and at the middle depth.

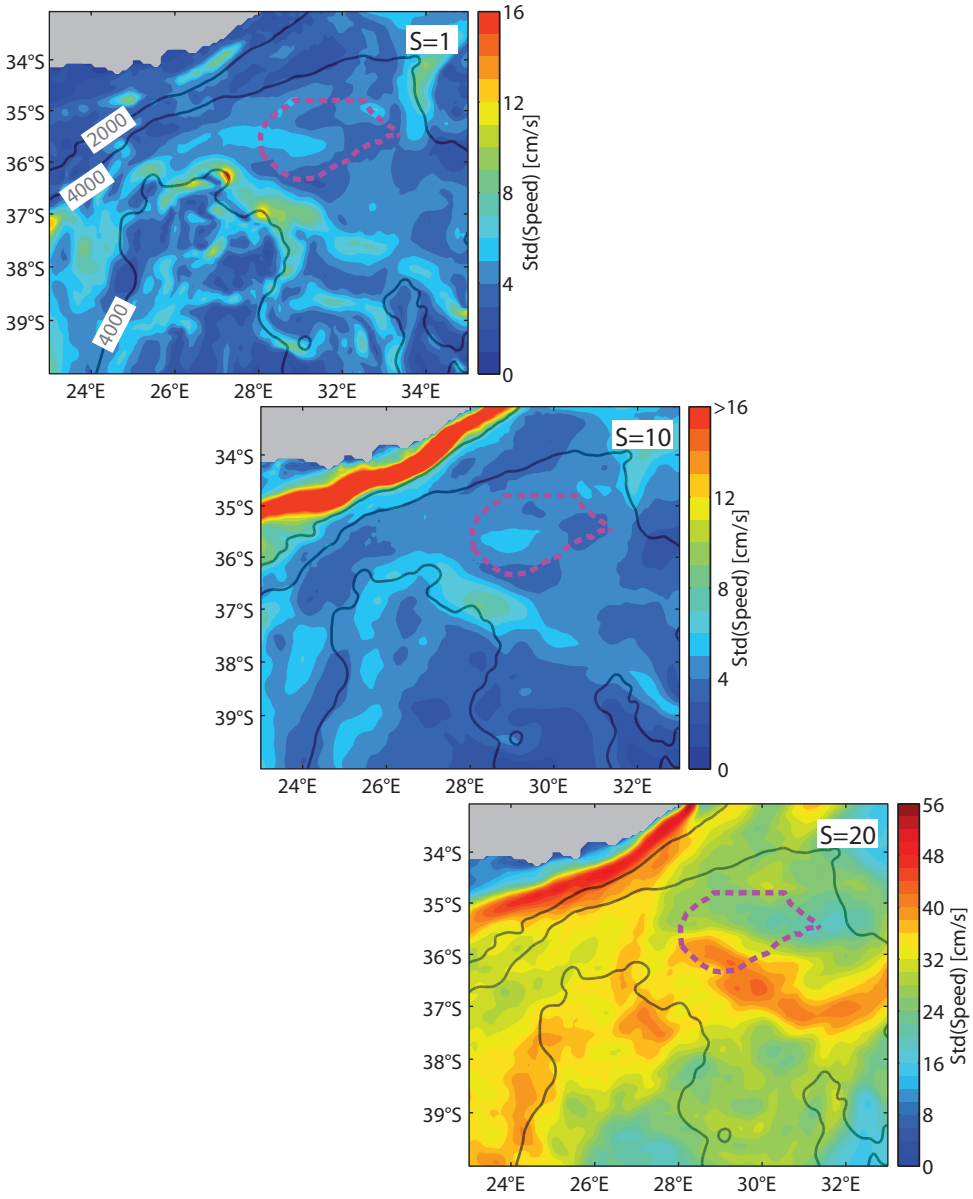

Figure 5.3.: The standard deviations of velocity fields in the layers $s1$, $s10$ and $s20$ from the 3rd to 5th model years. Otherwise like Figure 5.2.

5.2 Eddies in the Transkei Basin

In order to gain a better understanding of the temporal and spatial evolution of this vortex, a Hovmöller diagram of bottom velocities from the 3rd to the 5th model year is analyzed (Figure 5.4). This diagram crosses the center of the vortex movement along 29.25 °E from its northern to southern part (section shown

in Figure 5.1). We can distinguish two main flow directions: 1) approximately between 35.3 °S and 36.3 °S in eastward direction with velocities up to 27 cm s^{-1}, and 2) values of $5 - -35$ cm s^{-1} in westward direction between 36.3 °S and 37.2 °S (Figure 5.4). Their directions are relatively stable throughout these 3 model years. Such a hydrodynamic feature, currents with opposing directions and high velocities, can be identified as eddy events, similarly as the interpretation of the outer edge of the NADW eddy mentioned in Section 4.4. Using this feature shown in the Hovmöller diagram (Figure 5.4), 10 cyclonic eddies are revealed as individual, single events (Figure 5.4). With the current directions always being eastward in the northern parts and westward in its southern parts of the eddies, no anti–cyclonic eddy is found in the same location. The duration of these eddies is found to be variable. The longest eddy event continues for about two months (e.g. from 27th July to 2nd October of the 3rd model year). However, the shortest one exists for only about 13 days (e.g. from 11th April to 24th April of the 5th model year) (Figure 5.4). The centers of these eddies are marked by the velocity contour line of 0 cm s^{-1} which shifts slightly between 35.8 °S and 36.4 °S. Hence, centers of the eddies are mostly fixed in the center of the Transkei Basin. The southern boundary of the eddy events is mainly located along latitude 37.4 °S. Compared to this, the northern boundary is relatively unstable and shifts between 35 °S and 35.6 °S with a focal point near 35.4 °S. For all 10 eddy events over the 3 model years, their eastward setting branches always flow along the southern flank of the Agulhas Drift with velocities larger than 10 cm s^{-1}.

Velocity and salinity sections for a ‘no eddy event’ are compared to those during an ‘eddy event’ in order to image the vertical extent of these eddies (Figure 5.5). The cross section with typical isohalines on one day of a ‘no eddy event’ is shown as an example in Figure 5.5a. Following observed salinities (*Lutjeharms*, 2006; *You et al.*, 2003; *van Aken et al.*, 2004; *Boswell and Smythe-Wright*, 2002) and the verification of our model in Section 4.3, we can identify the water masses of the Agulhas Current System, Antarctic Intermediate Water, NADW and AABW

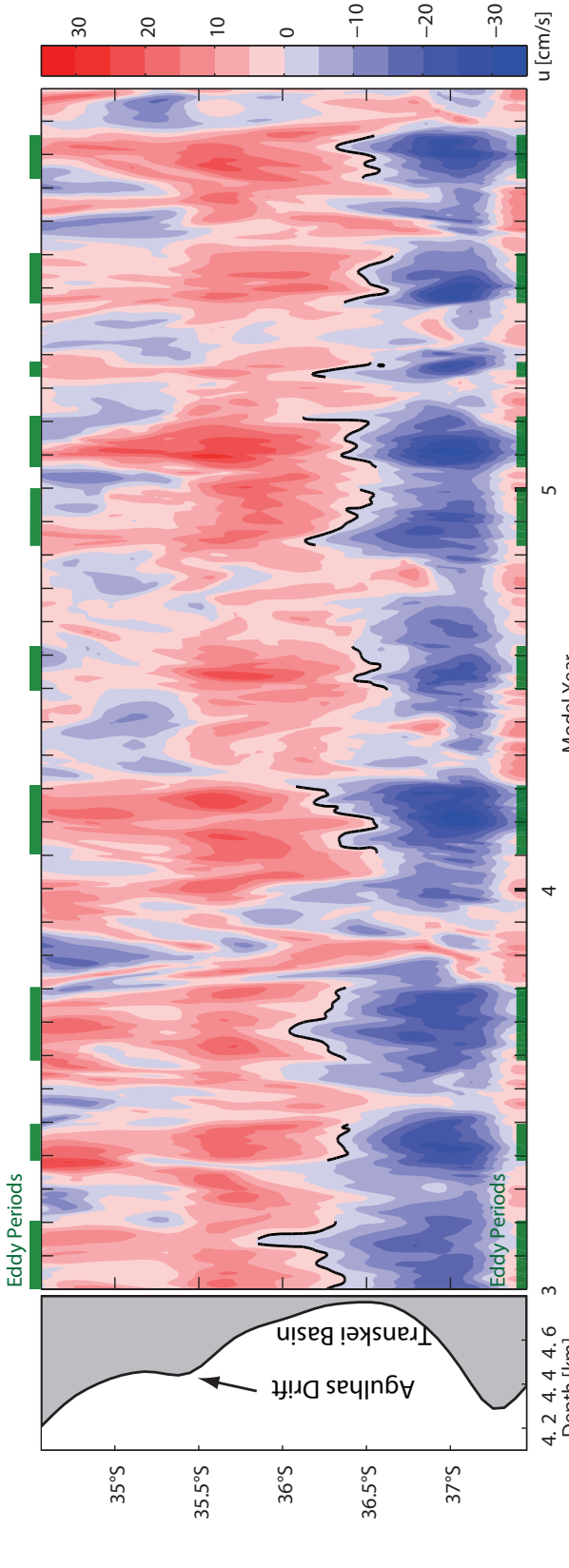

Figure 5.4.: Hovmöller diagrams for velocity along 29.25 °E from the 3rd model year to 5th model year. Location of this section is depicted in Figure 5.1. Velocities are positive (red) in the eastward direction. The green lines on the x–axis mark the periods of the eddy events. The black solid lines mark the centers of the eddies along this section.

from the surface to the bottom of this cross section through the Transkei Basin (Figure 5.5a). For the 'no eddy event', the stratification over the entire water column is distinct. Different water masses stably flow along isohalines. In contrast to this 'no eddy event', the isohalines indicate a significant convergence with a center approximately along 36.2 °S through the entire water column (Figure 5.5b). This feature indicates a high instability for the different water masses during the eddy event.

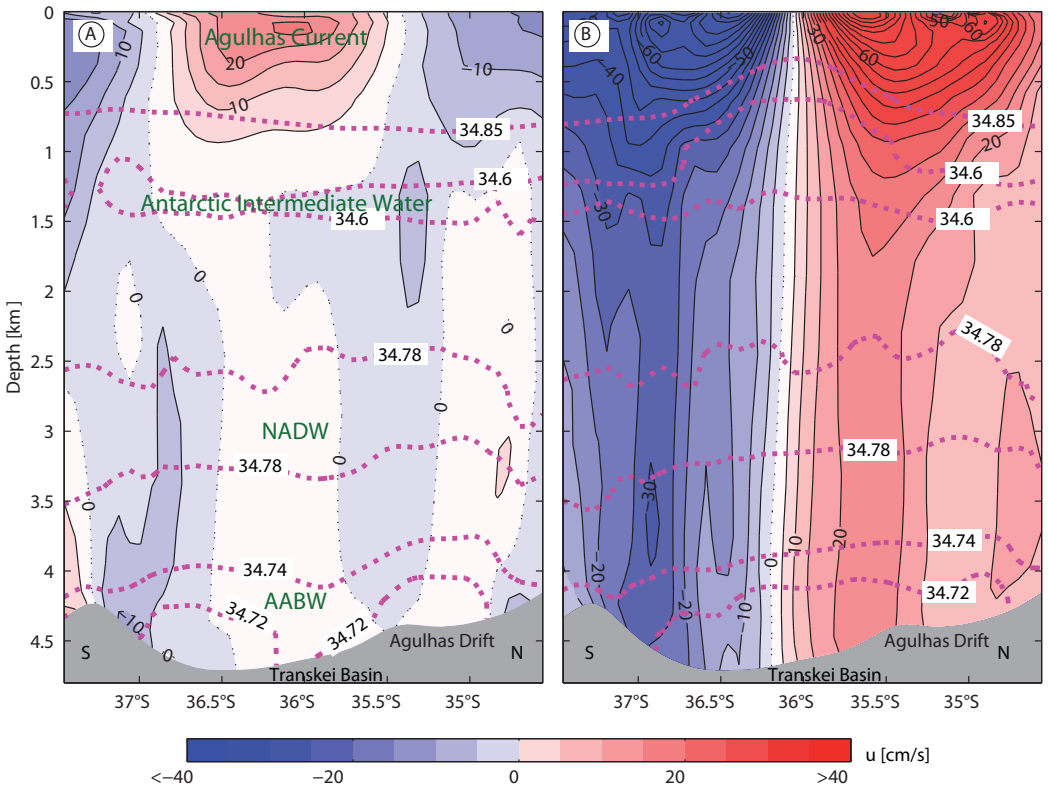

Figure 5.5.: Velocity section along 29.25 °E (a) for a 'no eddy' event on the 20th March, and (b) for an eddy event on the 12th April in the 4th model year. Location of these sections is depicted in Figure 5.1. Velocities are positive (red) in the eastward direction. In both plots, the black dotted lines denote zero velocity, and the magenta dashed lines mark the salinity surfaces indicating the different water masses.

5.3 Discussion: Mechanism for the Eddies

Eddies in the deep ocean have rarely been reported because of the limitation of the measurements. So far, there is no observation of a cyclonic movement in the deep part of Transkei Basin. However, *Casal et al.* (2006) sampled the outer edge of an NADW eddy at approximately 35.6 °S and 27.3 °E between 2200 m and 3500 m. Although this NADW eddy reveals a reverse rotation direction (anticyclone) compared to our simulated eddies, its location is within the extension of eddies from our models. In addition, different studies suggest the possibility of eddies existing in the deep ocean, e.g. *Kontar and Sokov* (1994) report considerable eddy activity through the entire water column in the northeastern tropical Pacific. Furthermore, *Weatherly et al.* (2002) and *Dengler et al.* (2004) revealed the presence of deep water eddies in the Brazil Basin.

Based on these studies of eddies, we further consider the formation mechanism of eddies in the Transkei Basin in our simulations. Due to the absence of a Deep Western Boundary Current in this region, our simulated eddies cannot be generated similar to the process explained by *Dengler et al.* (2004). *Kontar and Sokov* (1994) as well as *Casal et al.* (2006) pointed out that a high kinetic energy at the surface can be transferred downward and contribute to the formation of cyclonic or anticyclonic eddies in the deep water and even in the bottom water. This mechanism was also identified by *Chassignet and Boudra* (1988) in a numerical model. *Hollister and Nowell* (1991b) indicated that areas of sea–surface variability correlate with areas of excess benthic EKE. Similar conditions are appropriate for the current system in the Transkei Basin. High EKE in the Transkei Basin is shown in Figure 4.4. Here, the Agulhas Return Current is associated with high variability of sea surface height (*Naeije et al.*, 1992; *Boebel and Barron*, 2003). This high variability can be caused by perturbations in the Subtropical Convergence (STC). Such warm eddies in the surface layer with dimension of about 200 by 600 km have been observed at the Agulhas Plateau (*Lutjeharms and van Ballegooyen*, 1988).

We hence consider the formation mechanism of our simulated eddies as follows: The perturbations in STC and its corresponding shedding of eddies result in an increase of EKE from the surface to larger depths. Subsequently, the energy is transferred further downward. It causes an intensification of cyclonic motion in the depth ranges of deep water and even that of bottom water. In order to further confirm the location, dimension and orientation of simulated eddies in the Transkei Basin, continuous hydrographic measurements are needed.

6

Sediment Transport Patterns in the Transkei Basin

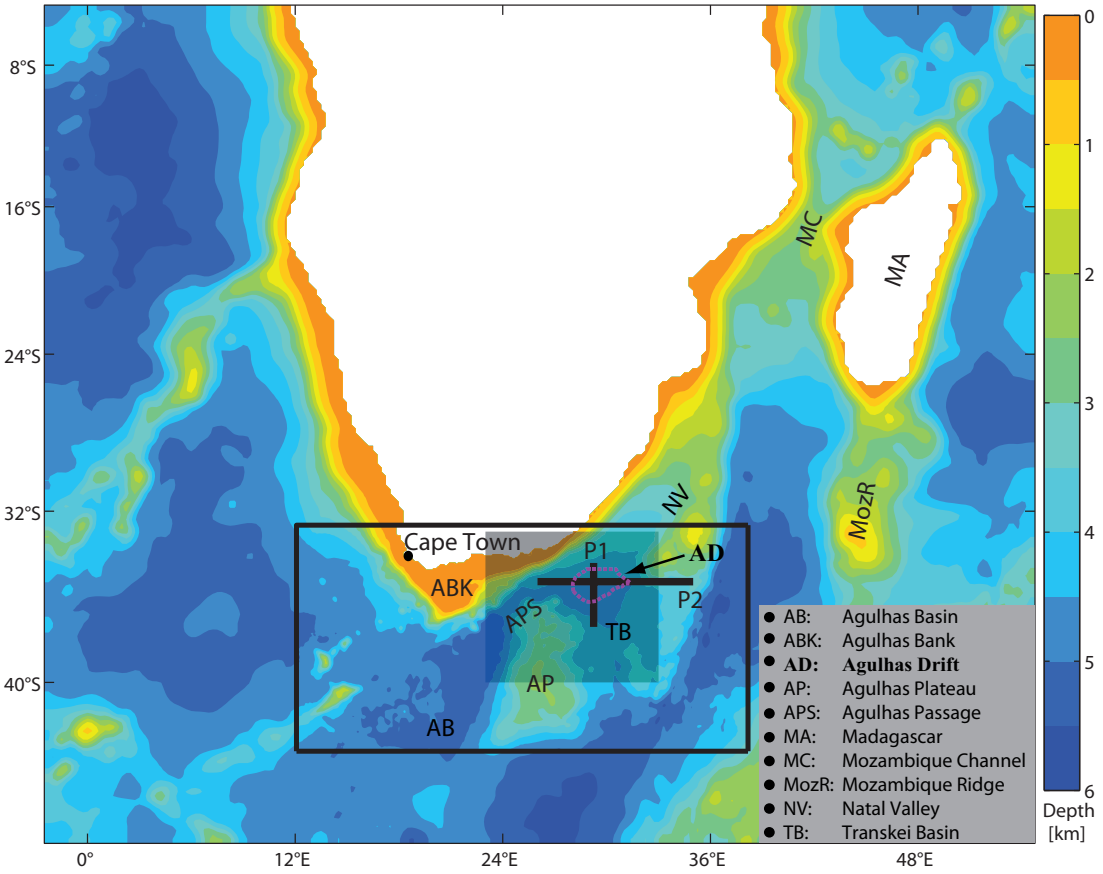

Figure 6.1.: Map of the whole model domain and the nested child model domain (black frame). The grey transparent rectangle marks the area observed in Figures 6.3– 6.8. Two thick solid lines marked as P1 and P2 label the positions of the Hovmöller diagrams shown in Figures 6.9 and 6.11. Computed boundary of the Agulhas Drift (*Schlüter and Uenzelmann-Neben*, 2008) is marked as in Figure 1.2.

As mentioned in Section 3.2.4, sediment transport patterns are simultaneously

simulated with the ocean circulation model from 6th to 9th model years. Similar to the analysis on the ocean circulation simulation in the previous chapter, the simulated sediment transport patterns for 4 size classes of silt (see Section 3.2.3) are observed in the area from 40 °S to 33 °S and from 23 °E to 33 °E (Figure 6.1).

6.1 Mean and Variation of Sediment Concentrations in the Bottom Layer

In Figures 6.2–6.5, the averages (top row) and standard deviations (bottom row) of concentrations of these 4 silt classes from the 6th to 9th model year are firstly presented to obtain an idea about their general distribution patterns and variabilities.

Silt1 is generally found to be sparse. The only noteworthy appearance ($\leq 0.06\,\mathrm{mg\,l^{-1}}$) is found along the north–east flank of the Agulhas Plateau (Figure 6.2a). In this area, the standard deviation of its concentrations (with a maximum of about $0.12\,\mathrm{mg\,l^{-1}}$) is also higher than in other areas (Figure 6.2b). Standard deviations higher than zero also appear within the 2000 m isobath along the northeast flank of the Agulhas Plateau, around the south–west flank of the Mozambique Ridge, and in the western part of the entrance of the Agulhas Passage (Figure 6.2b).

Silt2 also has its highest mean concentrations and standard deviations around the northeastern tip of the Agulhas Plateau (Figure 6.3). Here, values are higher than those of silt1 and cover a larger area. The maximum of averaged concentrations for silt2 is about $0.1\,\mathrm{mg\,l^{-1}}$. For its standard deviations, the highest value is $0.18\,\mathrm{mg\,l^{-1}}$. Silt2 can also be found in the southern part of the Agulhas Passage. Its standard deviation is distributed almost in the entire Agulhas Passage (Figure 6.3). Most significantly, silt2 can be found in the region of the Agulhas Drift. Furthermore, Silt2 mean concentrations decrease along the hump of the Agulhas Drift from $0.04\,\mathrm{mg\,l^{-1}}$ at its western boundary to zero in its geographic middle. From the hump, concentrations of silt2 further decrease north– and southward

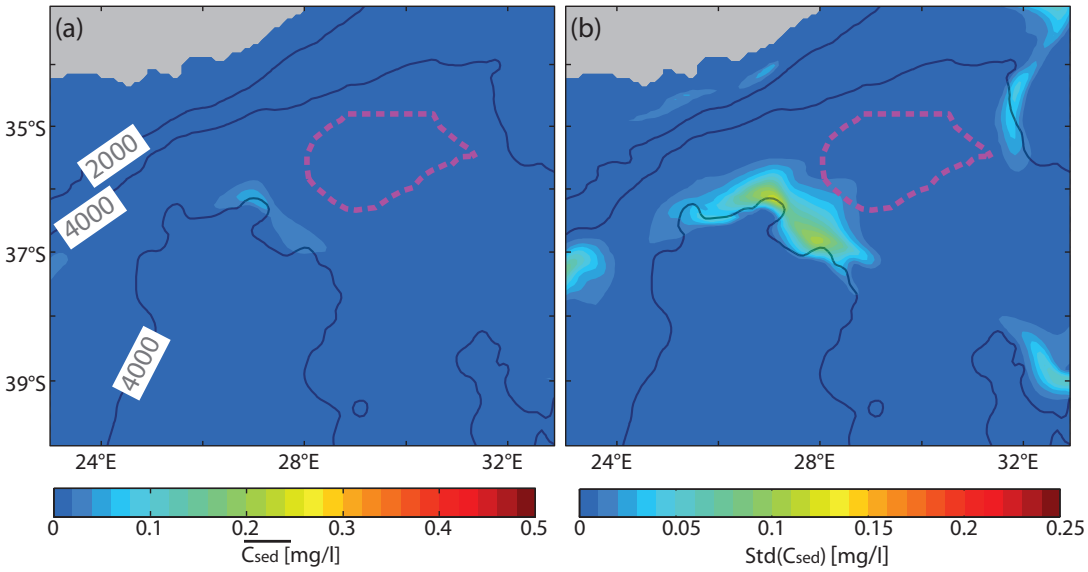

Figure 6.2.: Mean concentrations (a) and their standard deviations (b) of silt1 (coarse silt) in the model bottom layer in the Transkei Basin and vicinity from the 6th to 9th model year. The computed boundary of the Agulhas Drift is marked with the magenta line (*Schlüter and Uenzelmann-Neben*, 2008) as in Figure 6.1. Grey lines show 2000 m and 4000 m isobaths.

(Figure 6.3a). In this region, the elongation pattern of standard deviations for silt2 is quite similar to that of the average concentrations, whereas the standard deviations are more widely spread in the entire region of the Agulhas Drift and decease from $0.12\,\mathrm{mg\,l^{-1}}$ to $0.02\,\mathrm{mg\,l^{-1}}$.

Silt3 distributed widely in areas deeper than 4000 m water depth in the Transkei Basin and Agulhas Passage. In addition to these places, standard deviations up to $0.04\,\mathrm{mg\,l^{-1}}$ can be found north of the Agulhas Plateau (Figure 6.4). The highest mean concentration ($0.28\,\mathrm{mg\,l^{-1}}$) and the largest standard deviation ($0.24\,\mathrm{mg\,l^{-1}}$) are shown in the region northeast of the Agulhas Plateau. The difference between these two maxima is quite small compared to that of silt1 or silt2 (Figures 6.2–6.3). Not only the maxima, but also the values of mean concentrations and standard deviations in the region of the Agulhas Drift are quite similar for silt3. Along the hump of the Agulhas Drift, an eastward decrease of mean concentrations can be observed. In N–S direction mean concentrations increase from $0.08\,\mathrm{mg\,l^{-1}}$ in the north to $0.18\,\mathrm{mg\,l^{-1}}$ on the crest and then decrease again to

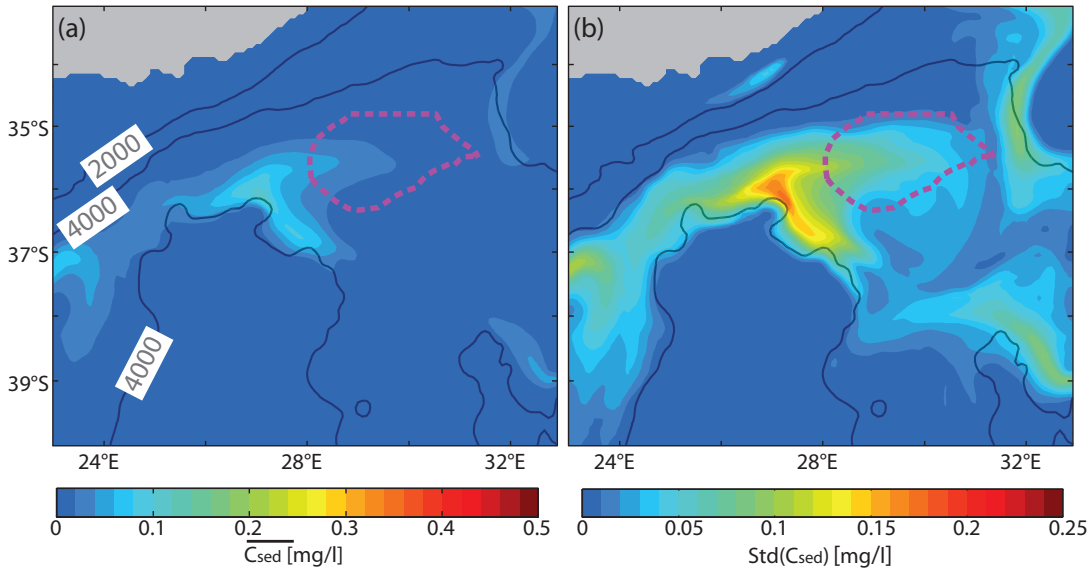

Figure 6.3.: Mean concentrations (a) and their standard deviations (b) of silt2 (medium silt) in the model bottom layer in the Transkei Basin and vicinity from the 6th to 9th model year. Otherwise like Figure 6.2.

0.14 mg l^{-1} in the south (Figure 6.4a). The standard deviations decrease eastward along the hump beginning apparently at its geographic center (approximately 35.5 °S, 30 °E). From there, the values are reduced from 0.2 mg l^{-1} to 0.13 mg l^{-1} towards the eastern boundary of the Agulhas Drift. To the north, the deviations decrease to approximately 0.1 mg l^{-1}, whereas taking on values of 0.13 mg l^{-1} in the south (Figure 6.4b).

High mean concentrations of silt4 are found almost across the whole Transkei Basin with a value of about 0.4 mg l^{-1}. They are higher in the southern Transkei Basin than in its north (Figure 6.5a). Mean concentrations gradually decrease from about 0.4 mg l^{-1} on the southeastern border of the Agulhas Drift to about 0.2 mg l^{-1} on the northwestern border (Figure 6.5a). From the Transkei Basin, the concentrations decrease eastward throughout the Agulhas Passage (Figure 6.5a). Both mean concentrations and standard deviations of silt4 take on high values in the Transkei Basin. Standard deviations range around 0.2 mg l^{-1}, which is approximately half of the values of the mean concentrations in this region (Figure 6.5b). We do not observe a decrease of silt4 standard deviations in relation

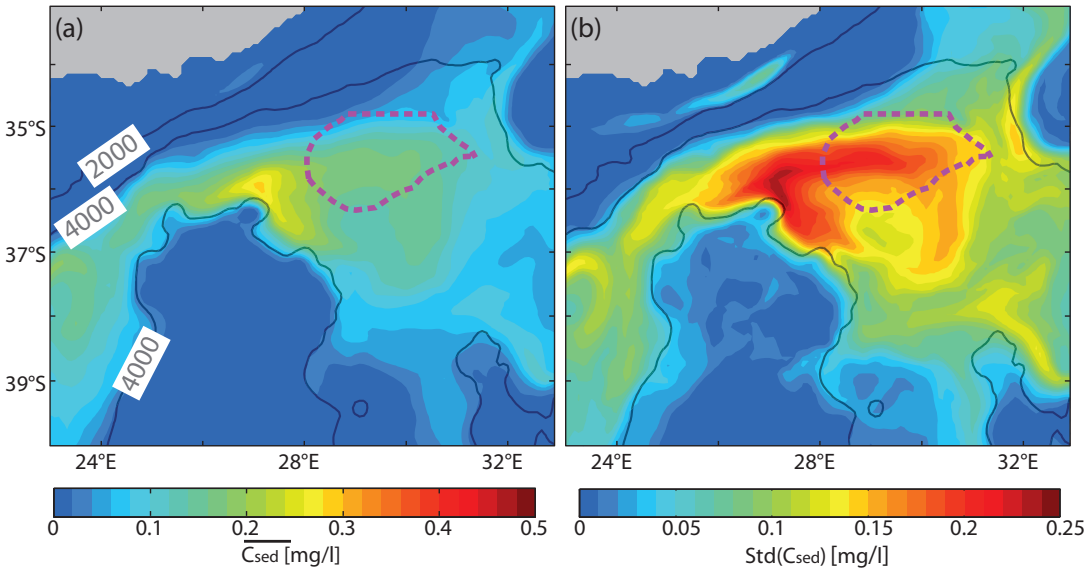

Figure 6.4.: Mean concentrations (a) and their standard deviations (b) of silt3 (fine silt) in the model bottom layer in the Transkei Basin and vicinity from the 6th to 9th model year. Otherwise like Figure 6.2.

to the Agulhas Drift structure, as we do for silt2 or silt3 (Figure 6.5b).

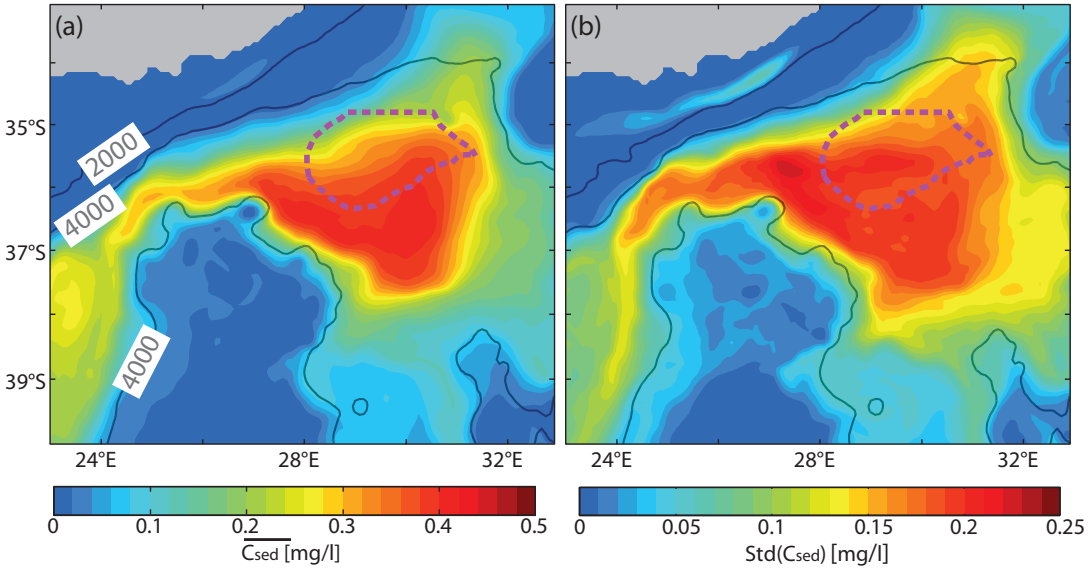

Figure 6.5.: Mean concentrations (a) and their standard deviations (b) of silt4 (very fine silt) in the model bottom layer in the Transkei Basin and vicinity from the 6th to 9th model year. Otherwise like Figure 6.2.

Comparing the mean concentrations of the 4 different silt classes in the region of the Agulhas Drift, we observe that silt1 does not go into suspension. Mean

concentrations increase with finer grain sizes from silt2 to silt4. Along the hump of the Agulhas Drift, mean concentrations of silt2 and silt3 are distributed in east–west direction, while this cannot be observed for silt4 (Figure 6.3a, 6.4a and 6.5a). Standard deviations of the 4 different silts also increase with smaller grain sizes. Furthermore, the E–W extensions along the hump of the Agulhas Drift can be identified more clearly in the standard deviation fields for silt2 and specially for silt3 (Figures 6.3–6.4).

6.2 Influence of the Eddies over the Sea Floor

As mentioned in Chapter 5, cyclonic eddies comprise the important local hydrodynamic process in our simulations. On the other hand, mean concentration and standard deviation fields show that silt2, silt3, and silt4 can be transported into the Transkei Basin, while silt1 does not appear there. Hence, the influence of eddies on the sediment transport patterns for silt2, silt3 and silt4 is studied. Snapshots of sediment concentrations and velocity fields over a typical eddy event are presented in Figures 6.6–6.8.

It is shown that e.g. on the 186th model day in the 8th model year, a certain day before the onset of an eddy event, there is no silt2 in the Transkei Basin (Figure 6.6). Directly after the onset of the eddy (e.g. on model day 222), only little silt2 with concentrations up to $0.2\,\mathrm{mg\,l^{-1}}$ can be observed in the eddy current along the northeastern flank of the Agulhas Plateau (Figure 6.6). With the strengthening of the eddy, more suspended silt2 can be found in the water column in this region. The concentration reaches a maximum of $0.8\,\mathrm{mg\,l^{-1}}$ on the 245th model day. However, only little silt2 can be brought further into the eastern part of the Agulhas Drift at this time. The strong eastward current within the northern segment of the eddy carries silt2 along the hump of the Agulhas Drift. There, the concentrations decrease eastward from $0.2\,\mathrm{mg\,l^{-1}}$ to zero (Figure 6.6). On model day 258, the intensity of the eddy has decayed. The concentrations along the northeastern flank of the Agulhas Plateau are markedly reduced. Nevertheless,

more silt2 (up to 0.4 mg l^{-1}) is found further eastward in the Agulhas Drift region. The gradual eastward reduction for the concentration is more distinct within a narrow band (Figure 6.6). A larger amount of silt2 is transported in the opposite direction: westwards along the northern flank of the Agulhas Plateau into the Agulhas Passage. The concentration maximum in the Agulhas Passage is 0.7 mg l^{-1} on model day 258 (Figure 6.6). Ten days later, the eddy in the Transkei Basin has already broken up. We now see only a small amount of silt2 with concentrations of about 0.1 mg l^{-1} in the Agulhas Drift area (Figure 6.6). Another ten days later, no silt2 can be found in the entire Transkei Basin (Figure 6.6).

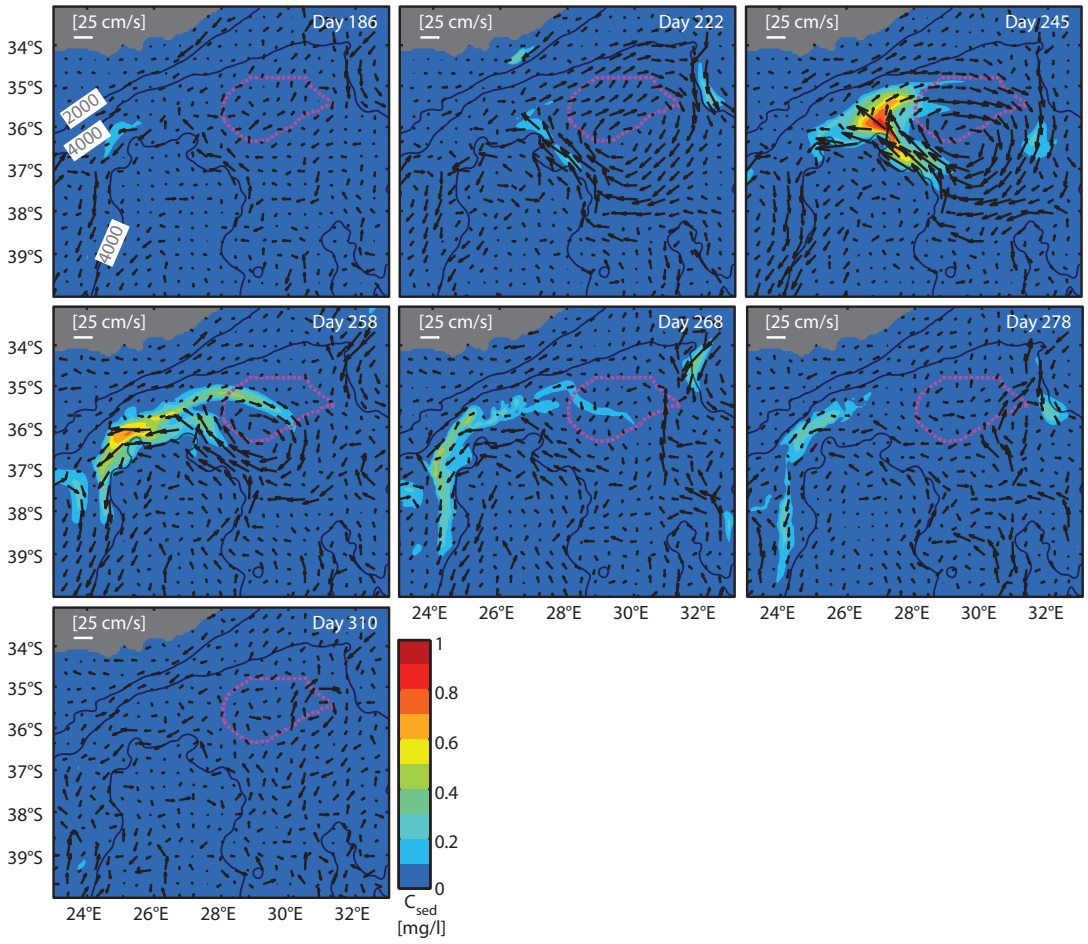

Figure 6.6.: Change of suspended concentrations for silt2 (medium silt) and velocity field (shown as black arrows) in the model bottom layer during an eddy event in the 8th model year. 1 vector is portrayed every 4 vectors. Otherwise like Figure 6.2.

The transport patterns for silt3 in general are similar to that of silt2 (Fig-

ures 6.6–6.7). However, larger amounts of silt3 can be observed throughout the whole eddy period. For example, silt3 concentrations along the northeastern flank of the Agulhas Plateau are up to $0.4\,\mathrm{mg\,l^{-1}}$ on model day 222 and distributed over a larger area compared to silt2. Furthermore, more silt3 is carried into the region of the Agulhas Drift. On model day 258, the maximum concentration of silt3 is $0.7\,\mathrm{mg\,l^{-1}}$ within the drift region. This value is almost twice that of silt2 (Figures 6.6–6.7). Silt3 also can be retained in the water column for a longer period than silt2. On model day 268, the concentrations of silt3 are still up to $0.7\,\mathrm{mg\,l^{-1}}$. On model day 278, the concentrations' maximum slightly reduces to $0.6\,\mathrm{mg\,l^{-1}}$. Until model day 310, silt3 can always be found in the region of the Agulhas Drift (Figure 6.7).

Different from silt2 and silt3, silt4 has a more complex transport pattern (Figure 6.8). Before the eddy event (on model day 186), silt4 can already be found in the Transkei Basin. These sediments are remnants from the last eddy event (not shown here). At the beginning of the eddy formation, silt4 is homogeneously redistributed by the eddy current. It is converged in the eddy center with concentrations of about $0.5\,\mathrm{mg\,l^{-1}}$ (Figure 6.8). Simultaneously, high concentrations of silt4 are also shown along the northeastern flank of the Agulhas Plateau where we also observe high concentrations of silt2 and silt3 (Figures 6.6–6.8). On the 245th model day, the concentrations of silt4 are just up to $0.4\,\mathrm{mg\,l^{-1}}$ along the flank, where the eddy current is very strong. These values of concentrations are lower than those of silt2 and silt3 for the same place and time (Figures 6.6–6.8). High concentrations for silt4 (around $0.5\,\mathrm{mg\,l^{-1}}$) are mostly found in the northern part of the Agulhas Drift (Figure 6.8). During the last phase of the eddy event (e.g. on model day 258), most of silt4 is distributed along the northern and northeastern flanks of the Agulhas Plateau. There, concentrations are up to $0.9\,\mathrm{mg\,l^{-1}}$. Silt4 concentrations are significantly lower in the entire Agulhas Drift region than those on model day 245, even though they still reach values of $0.5\,\mathrm{mg\,l^{-1}}$ (Figure 6.8). After the eddy event, on model days 268, 278 and 310, silt4 concentrations remain

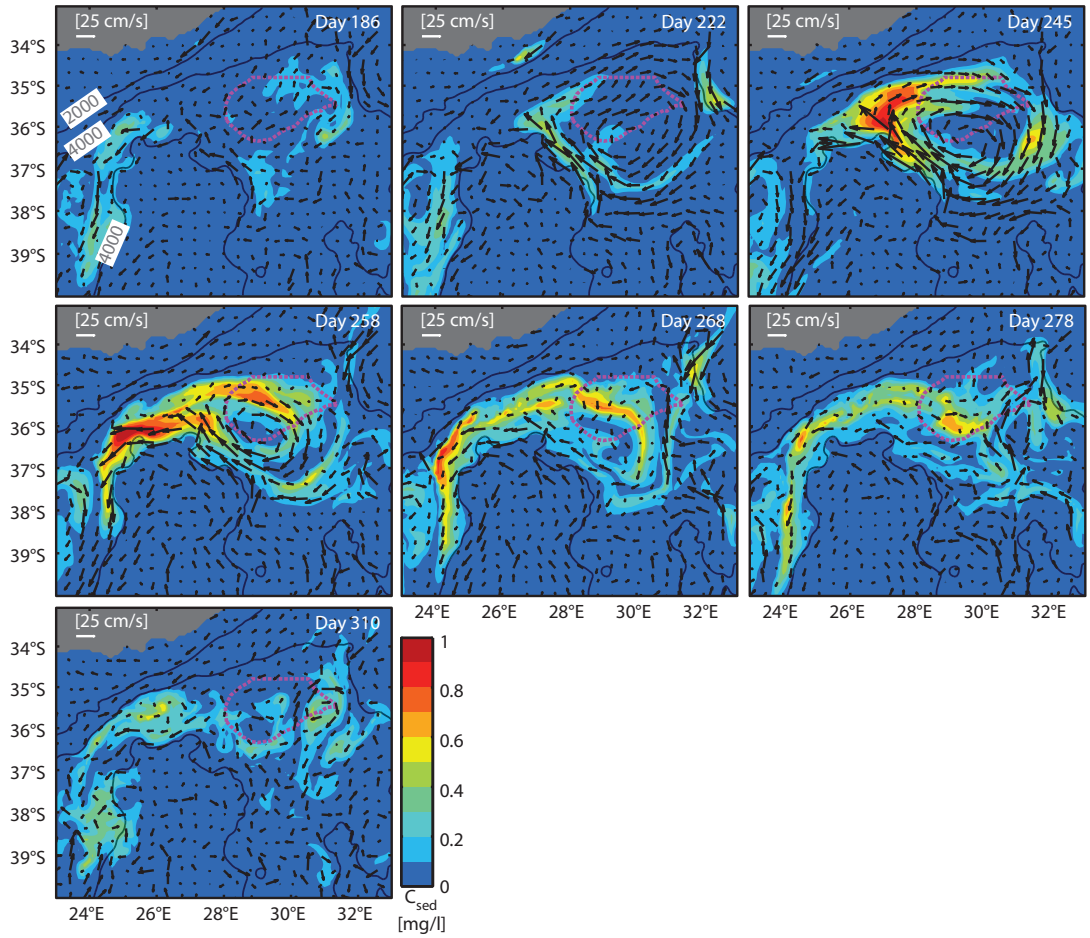

Figure 6.7.: Change of suspended concentrations for silt3 (fine silt) and velocity field (shown as black arrows) in the model bottom layer during an eddy event in the 8th model year. Otherwise like Figure 6.6.

high (up to $0.5\,\mathrm{mg\,l^{-1}}$) decrease slowly within the Transkei Basin.

Based on the just described influence of a single eddy event on the sediment transport pattern, the correlations between eddies and suspended sediment concentrations of different silt classes from the 6th to 9th model year are further discussed (Figure 6.9).

As we have seen in Chapter 5, the strongest velocities within the eddy are found along the northeastern flank of the Agulhas Plateau. After the onset of the eddy, a first increase of the sediment concentration is shown in this region (Figures 6.6–6.8). In Figure 6.9a, we compare mean concentrations of the 4 silt

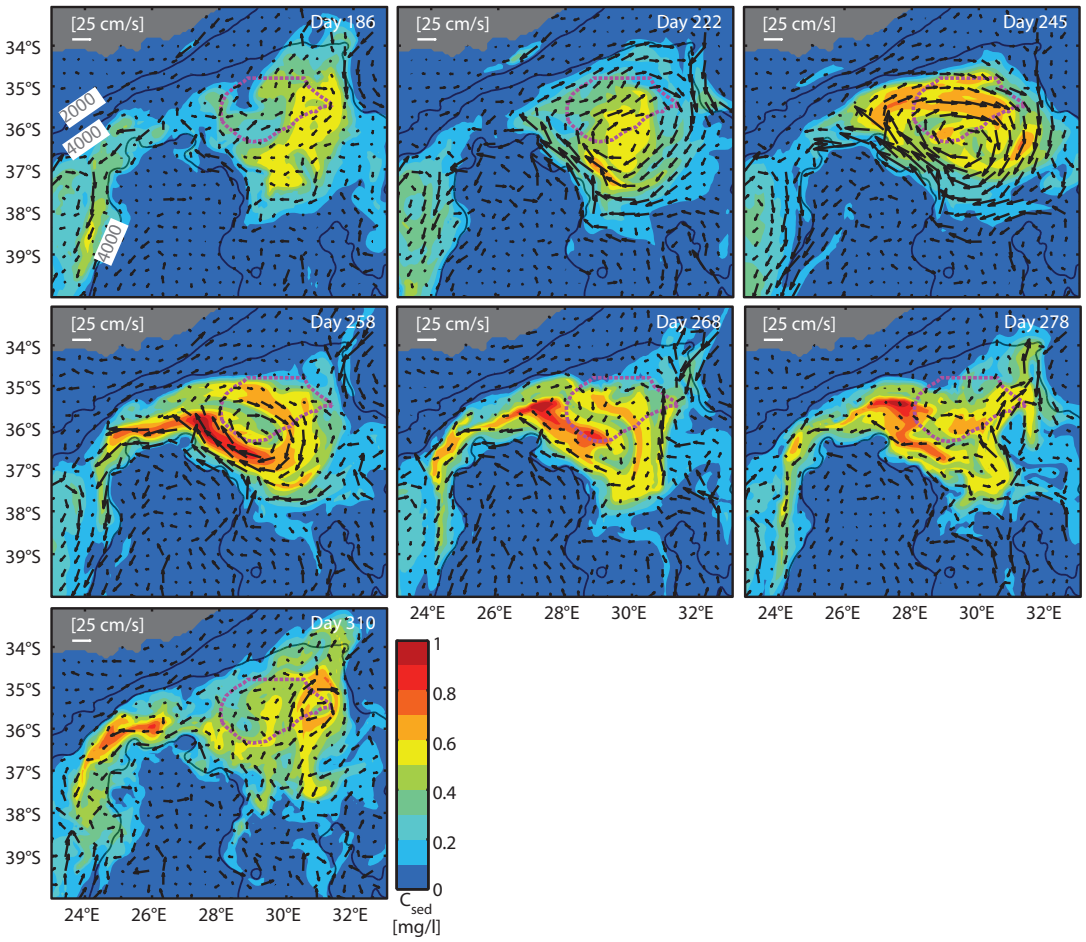

Figure 6.8.: Change of suspended concentrations for silt4 (very fine silt) and velocity field (shown as black arrows) in the model bottom layer during an eddy event in the 8th model year. Otherwise like Figure 6.6.

grain sizes with the averaged kinematic bottom stress for this region, where the bathymetry varies from 3800 m to 4600 m from 37.6 °S to 35.85 °S and from 26 °E to 30.5 °E. The kinematic bottom stress and the sediment concentrations for all different sediment classes strongly correlate with each other (Figure 6.9a). The sediment concentrations increase directly following changes of the kinematic bottom stress in this region. Silt3 shows the large increase in concentration. The concentrations of silt1 and silt2 are close to zero, when the kinematic bottom stress is not higher than $0.1\,\mathrm{N^2\,m^{-2}}$. The decreases of silt1 and silt2 concentrations are still synchronous with a reduction in bottom stress. In contrast, the

concentrations of silt3 and silt4 decrease slower. The concentrations of silt4 are higher than $0.1\,\mathrm{mg\,l^{-1}}$ at all times following model year 7 (Figure 6.9a).

Peaks of kinematic bottom stress along the northeastern flank of the Agulhas Plateau (Figure 6.9a) correlate with individual eddy events, which are shown in the Hovmöller diagram of the velocity field across the middle of these eddies from north to south (Figure 6.9b, section P1 in Figure 6.1). Over the 4 model years, we found 14 eddy events, which are highlighted by green lines on the upper x–axis. Referring to these eddy periods (Figure 6.9b), we see that the sediment concentrations along the northeastern flank of the Agulhas Plateau (Figure 6.9a) begin to increase almost simultaneously with the onset the eddies, and the decrease of the concentrations come to end after the breakup of the eddies.

The changes of sediment concentrations along section $29.25\,^{\circ}\mathrm{E}$ are further considered (Figure 6.9b). Silt2 is mainly distributed along the hump of the Agulhas Drift ($\approx 35.4\,^{\circ}\mathrm{S}$). The values rise up to $0.5\,\mathrm{mg\,l^{-1}}$ during the 4th eddy event from October in model year 6 to January of model year 7. Except for this period, the concentrations are not larger than $0.3\,\mathrm{mg\,l^{-1}}$. Small amounts of silt2 can also be found in the southern Transkei Basin in the early days of long eddy events (Figure 6.9b, $36.5\,^{\circ}\mathrm{S} - -37\,^{\circ}\mathrm{S}$, e.g. October, model year 6 – January, model year 7). Furthermore, the appearance of silt2 lags behind the onset of the eddy events. The concentrations of silt2 decrease to zero before the eddies totally break up (Figure 6.9b).

Changes of silt3 concentrations can be observed for all eddy events (Figure 6.9b). During these periods, silt3 can be found from $35\,^{\circ}\mathrm{S}$ to $37.5\,^{\circ}\mathrm{S}$ (Figure 6.9b). However, concentrations higher than $0.5\,\mathrm{mg\,l^{-1}}$ are found primarily in the area around the hump of the Agulhas Drift ($\approx 35.4\,^{\circ}\mathrm{S}$). The increase in silt3 concentrations also lags behind the initiations of eddy formation, but not as much as the concentrations of silt2. Moreover, silt3 concentrations decrease more slowly than those of silt2. Even after the ends of the eddy events have ended, the

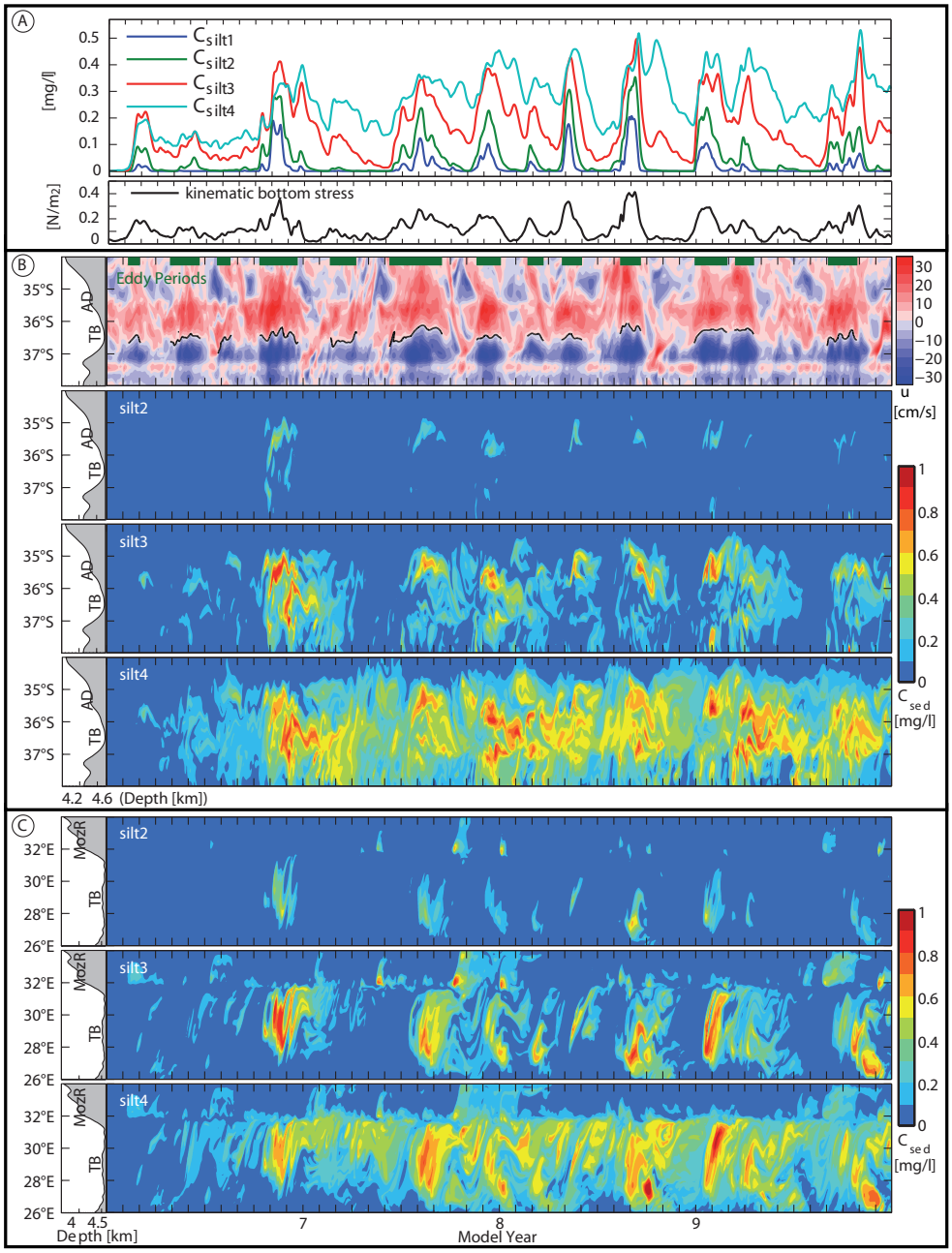

Figure 6.9.: (a) Time series of mean sediment concentrations and mean kinematic bottom stress along northeastern flank of the Agulhas Plateau over the four model years. (b) Hovmöller diagrams of velocity and sediment concentrations across the region of the Agulhas Drift along 29.25 °E (P1 in Figure 6.1) over 4 model years. Velocities are positive in the eastward direction. The green lines on upper x–axis mark the periods of the eddy events. The black solid lines mark the centers of the eddies along this section. (c) Hovmöller diagrams of sediment concentrations like (b) but along 35.38 °S (P2 in Figure 6.1). The topographic abbreviations are as in Figure 6.1.

concentrations of silt3 still have not decreased to zero (Figure 6.9b).

Concentrations of silt4 are always larger than zero once the first eddy is formed (Figure 6.9b). Still, silt4 concentrations increase and decrease with the eddy periods. The highest concentrations of silt4 (larger than $0.7\,\mathrm{mg\,l^{-1}}$) for each eddy are located almost in the center of the Transkei Basin between 36 °S and 37 °S, not on the hump but on the southern flank of the Agulhas Drift (Figure 6.9b).

Figure 6.9c further shows the changes of these concentrations for these 3 silt classes from the 6th to 9th model year along another cross section, which is perpendicular to the section mentioned above, and crosses the Agulhas Drift along 35.38 °S in E–W direction (section P2 in in Figure 6.1). West–east changes of silt2 concentrations are clearly revealed. Silt2 concentrations strongly increase eastward at approximately 26.5 °E. The highest quantities (larger than $0.5\,\mathrm{mg\,l^{-1}}$) are reached on the western side of the Agulhas Drift, at about 28 °E. From there, an eastward decrease of concentrations can be observed to about 30 °E (Figure 6.9c). A small amount of silt2 can also be found during a few eddy events on the rise of the Mozambique Ridge. Concentrations there usually are less than $0.2\,\mathrm{mg\,l^{-1}}$, and the material does not reside longer than 1 month (Figure 6.9c). Silt3 also shows east–west variations in concentrations (Figure 6.9c). Still, the concentrations' maxima are distributed more widely and further eastward (Figure 6.9c). Along this latitudinal cross section, the highest concentrations of silt4 appear to be located randomly for each eddy event. They can be found across the entire Agulhas Drift (Figure 6.9c).

Based on the above analyses along specific sections cross the Agulhas Drift, we further observe the changes in averaged concentrations of silt2, silt3 and silt4 over the entire Agulhas Drift region, whose boundaries are based on the study of *Schlüter and Uenzelmann-Neben* (2008) (Figure 6.1), from the 6th to 9th model year (Figure 6.9). The comparison of the concentrations of these sediments shows again that finer sediments have higher concentrations at the Agulhas Drift. These values are compared to the averaged horizontal kinetic energy (HKE) in the same

region. The HKE indicates the strength of the velocity field, and hence links to the eddies. The peaks of concentrations of silt2 and silt3 are correlated with high HKE and long duration of the eddies, although the changes in concentrations and HKE are not simultaneous (Figure 6.10). The concentrations of silt2 and silt3 increase within a few days after the onsets of eddy events. The time difference between the changes in HKE and silt2 concentrations is larger than that between changes in HKE and silt3 concentrations. The maximum values of the peaks for silt2 concentrations are mostly between $0.05\,\mathrm{mg\,l^{-1}}$ and $0.1\,\mathrm{mg\,l^{-1}}$. Silt2 concentrations in the region of the Agulhas Drift can decrease to $0\,\mathrm{mg\,l^{-1}}$ during the no eddy periods. For silt3, the highest concentrations of the peaks are mainly situated between $0.2\,\mathrm{mg\,l^{-1}}$ and $0.4\,\mathrm{mg\,l^{-1}}$. The minimum of silt3 concentrations lies about $0.05\,\mathrm{mg\,l^{-1}}$. In contrast to those of silt2 and silt3, the variation in silt4 concentrations is complicated (Figure 6.10). The correlation between eddy event and silt4 concentrations is not obvious. Increases of its concentrations sometimes increase after the eddy events. One thing was for certain, the suspended concentrations of silt4 at the Agulhas Drift are larger than $0.2\,\mathrm{mg\,l^{-1}}$ for all the time after the 7th model year (Figure 6.10).

6.3 Vertical Concentration Profiles Cross the Agulhas Drift

In addition to horizontal variations we further study the vertical distribution of the different silt sizes within the water column for one representative day of an eddy event.

An arc–shaped distribution of silt2 concentrations is shown over the hump of the Agulhas Drift (Figure 6.11a). There, concentrations of up to $0.2\,\mathrm{mg\,l^{-1}}$ can be found close to the sea floor. The suspended silt2 in the water column extends upwards to a water depth of about 4200 m (Figure 6.11a). A similar distribution pattern is revealed in the vertical structure of silt3 concentrations. Silt3 concentrations are spread over a larger area from $34.5\,^{\circ}\mathrm{E}$ to $36\,^{\circ}\mathrm{E}$ in horizontal, and

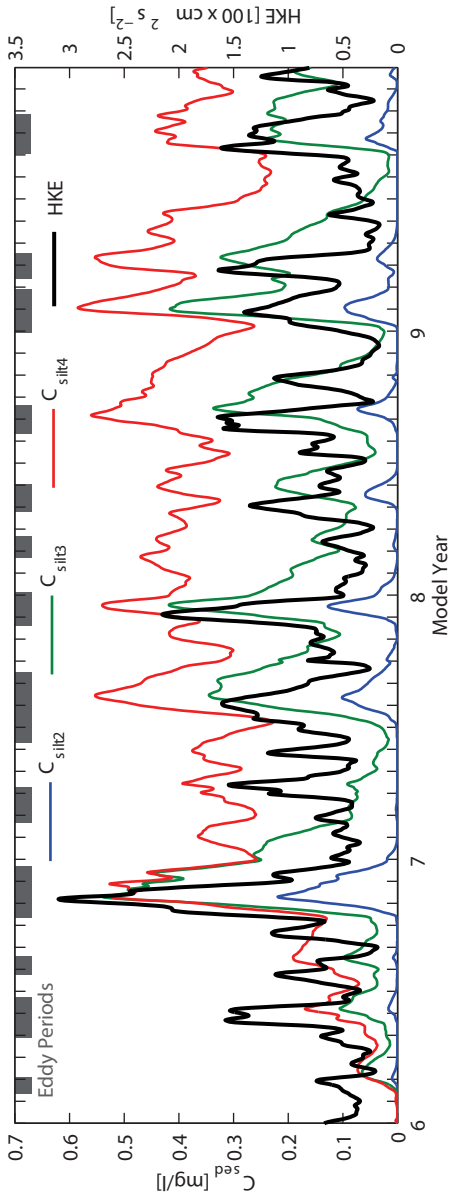

Figure 6.10.: Mean sediment concentration and averaged horizontal kinetic energy (HKE) at the Agulhas Drift over four model years. The thick grey blocks on the upper axis mark the eddy periods.

upwards to 4100 m depth in vertical direction. The highest silt3 concentration of about 0.7 mg l^{-1} is shown at the same position as that of silt2 over the hump of the Agulhas Drift (Figure 6.11a). We can further observe silt3 concentrations of up to 0.4 mg l^{-1} in the southern Transkei Basin (Figure 6.11a). The distribution of silt4 concentrations in the area of the Agulhas Drift is similar to those of silt2

and silt3, but the values of silt4 concentration there are lower than those observed in the southern Transkei Basin (Figure 6.11a, 36.5 °S – −36.8 °S).

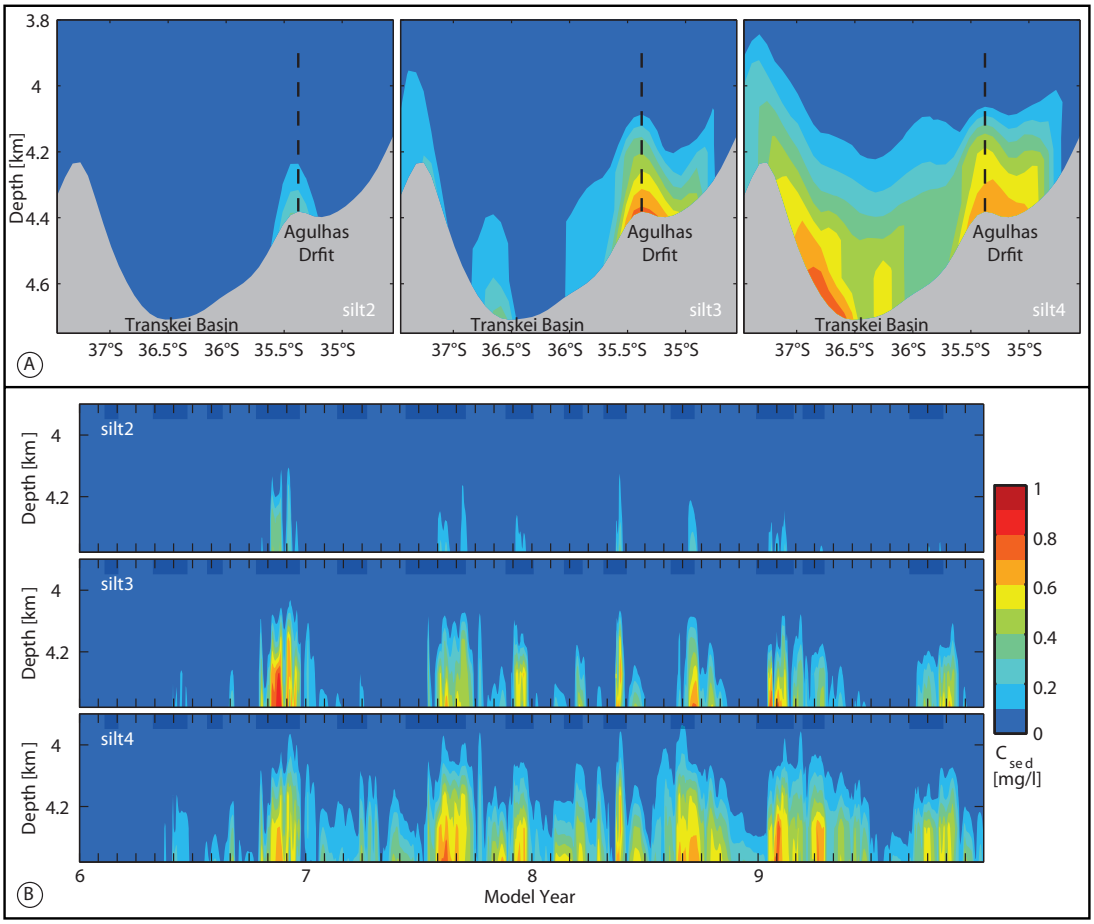

Figure 6.11.: Vertical sediment concentration sections along 29.25 °E (P1 in Figure 6.1) on 28 May in the 7th model year. The black dashed lines label the section position of Figure 6.11b. (b) Hovmöller diagrams for the vertical concentration section at 29.25 °E, 35.38 °S (intersection of two sections P1 and P2 in Figure 6.1). The thick grey transparent lines on the upper axis mark the eddy periods.

Additionally to variations in sediment concentrations in the bottom layer (Figures 6.9b–c), we have analyzed variations of concentrations over the same period (4 model years) over the whole water column at a representative location (35.38 °S/29.25 °E, Figure 6.11a). The suspended silt extends to different water depths depending on the silt class. Silt4 can be carried upwards into water depths around 4000 m (Figure 6.11b), while silt2 and silt3 can only reach water depths of about 4100 m and 4150 m, respectively. Concentrations for all these classes

change almost simultaneously, even if at different depths (Figure 6.11). At this example location, the concentrations increase sharply. While concentrations of silt2 rise only up to $0.5\,\mathrm{mg\,l^{-1}}$, the maxima of silt3 and silt4 are about $0.9\,\mathrm{mg\,l^{-1}}$. The concentrations of both silt2 and silt3 decrease quickly from their maximum values to zero. In comparison, silt4 concentrations decline at a much slower rate (Figure 6.11a).

6.4 Discussion

6.4.1 The Role of Eddies on Sediment Transport Patterns in the Transkei Basin

We have seen that suspended sediments are found in water depths where AABW is active (Figure 5.5 and 6.11). Individual eddy events have been identified via our numerical simulations to be the important hydrodynamic processes in those depths (Figures 5.2 and 5.5). We thus conclude that eddies entraining AABW strongly influence sediment erosion and transport within the Transkei Basin (Figures 6.6–6.11). Fine silt is transported parallel to the hump of the Agulhas Drift by the northern segments of these eddies, which set eastwards across the southern flank of the Agulhas Drift (Figures 6.6–6.11). This is in agreement with seismostratigraphic analyses presented by *Schlüter and Uenzelmann-Neben* (2007, 2008). They interpreted that the Agulhas Drift has been built up by an eastward setting branch of AABW. The seismostratigraphic observations do not reveal the presence of cyclonic eddies because of their short–term variability. The influence of eddies on sediment transport has been analyzed by a number of authors for other locations (*Hollister and McCave*, 1984; *Hollister and Nowell*, 1991b; *Washburn et al.*, 1993; *Ogston et al.*, 2004; *Keylock et al.*, 2005). These studies suggest that benthic storms occur in the deep ocean generate anomalously strong currents, which then are capable of moving vast quantities of sediment. Unfortunately, these analyses were carried out in other regions. Further local measurements are necessary to confirm the presence of these eddies in Transkei Basin.

6.4.2 Grain Size classes of the Agulhas Drift

Our experiments with sediment grain sizes indicate that the eddies simulated in the Transkei Basin have different transport capabilities for different silt classes (Figures 6.6–6.11). In particular, silt1 (coarse silt) cannot be brought into the region of the Agulhas Drift by the eddies over the studied four model years, both means and standard deviations of the suspension concentrations are zero (Figure 6.2). In contrast, large amounts of silt2 (medium silt) and silt3 (fine silt) are transported into the drift area. The eddy currents carry silt3 further eastward than silt2 (Figure 6.6, 6.7 and 6.9). The concentrations of both silt2 and silt3 begin to decrease during the last phases of the eddies (Figures 6.6–6.7 and 6.9–6.11). The decline in silt3 concentrations continues even after the eddy event is over (Figure 6.7 and 6.9–6.11). These trends in decrease of suspension concentrations indicate that the bottom current is not strong enough to further transport silt2 and silt3 once the eddies begin to weaken. Instead of transportation, deposition of silt2 and silt3 will occur. Silt4 (very fine silt) is widely distributed in the Agulhas Drift region, and we observe no obvious reductions in concentration for silt4 in this area. Silt4 can obviously be transported much further by the strong eddy currents into the southern Transkei Basin (Figures 6.8–6.9). With coarse silt (silt1) not being mobilized and transported and very fine silt (silt4) showing no substantial decrease in suspension concentration thus indicating continued transport, we suggest that medium silt (silt2) and fine silt (silt3) are probable components of the Agulhas Drift deposits, with medium silt being only in the western part of the Agulhas Drift.

Although the drilling data is lacking in the Transkei Basin, grain size analyses were carried out at material from ODP Leg 178 Sites 1095 and 1096 drilled at another xontourite drift–Drift 7, west of the Antarctic Peninsula. 70% of the sediment retrieved showed grain sizes smaller than 4μm (*Pudsey*, 2001a,b; *Wolf-Welling et al.*, 2001). However, for the rest components of the Drift 7, medium and fine silt were found to increase during the drift growth stage, while coarser silt

was deposited during the drift maintenance stage. Transferring this result to the Agulhas Drift we suggest that the Agulhas Drift is still within the growth stage. This is supported by seismic observations (*Schlüter and Uenzelmann-Neben*, 2007, 2008).

Our simulations further indicate that all different size classes of silt are resuspended by the strong velocities within eddies north–east of the Agulhas Plateau (Figures 6.6–6.11). Such an event is also reported by *Hollister and McCave* (1984) based on sedimentological and stratigraphic investigations and by *Gross and Dade* (1991) with their simulations. As we mentioned before, strong turbulences in the ocean are interpreted to be a major source of suspended materials to abyssal flows (*Gross and Dade*, 1991). We thus suggest that sediment resuspended along the north–eastern flank of the Agulhas Plateau during eddy events represents an important sediment source for the Agulhas Drift. Silt2 cannot be identified for all eddy events. It only appears in the drift region, when the kinematic bottom stresses are large enough (Figure 6.9). So, we interpret medium silt to compose the drift deposits to a lesser extent.

7

Conclusions and Outlook

A simulations study is presented in this thesis. The numerical model simulates the current system and the suspended sediment transport patterns in the region south of southern Africa. The simulations are carried out under the present conditions (topographic, forcing, boundary and climatological datasets).

The approach of our ocean circulation model is examined by comparison with observations both at the sea surface and along the vertical cross sections. The hydrographic features from our simulation agree well with hydrographic observations from satellite images of SST and SSH, computed EKE from SSH, project AUCE, and the literature (e.g. *Lutjeharms*, 2006). These Comparisons indicate that the approach of our simulations to the reality is achieved.

This circulation model is further integrated with the sediment transport model. Four different grain size classes ranging from the coarse silt to very fine silt are applied as non–cohesive sediments in the model.

The model results in the region of the Agulhas Drift and vicinity are analyzed in more detail. A basic knowledge about the influence of short–term hydrodynamic processes on the local sediment transport patterns is obtained. In the following, the conclusions of our simulations are described according to the questions mentioned in Chapter 1:

(1) Which hydrodynamic processes strongly influence sediment transport patterns over relatively short–term periods at the Agulhas Drift and in its vicinity and how?

- Mesoscale cyclonic eddies are identified as individual events in the central

Transkei Basin. The major water masses involved within these eddies are AABW, NADW, AAIW and the Agulhas Current system. We suggest that these eddies are formed due to high variability of EKE caused by perturbations in the STC. It transformed a large amount of energy from the sea surface to the ocean bottom.

- The north segments of these eddies are located in the region of the Agulhas Drift. An eastward flow within the eddies is observed along the southern flank of the Agulhas Drift. The eddy events are thus interpreted to have an important influence on the sediment distribution in the region of the Agulhas Drift.

- The mesoscale eddies involving AABW have significant influences on sediment transport, resuspension and deposition in the Transkei Basin under present current conditions.

- The south–western part of these eddies exhibit strongest velocities along the northeastern flank of the Agulhas Plateau. Here, eddy currents have the capacity to resuspend silts of different grain sizes. The resuspension capability is shown to be inversely proportional to the grain size.

- Only sediment finer than coarse silt can further be transported into the region of the Agulhas Drift. Medium and fine silts are interpreted to be deposited in the region of the Agulhas Drift, after the intensities of the eddy bottom current begin to decrease. Very fine silt appears to be further transported by the eddies into the southern Transkei Basin.

(2) What are the potential components of the Agulhas Drift and their corresponding erosion, transport and depositional processes under the local current condition?

Potential components of the Agulhas Drift range from medium silt to fine silt. Since the coarse silt cannot be transported into the region of the Agulhas Drift

in our simulations. On the hand side, the very fine silt is hard to be deposited. They have usually high suspended sediment concentrations in the whole Transkei Basin. The sediments ranging from medium silt to fine silt can be deposited in the region of the Agulhas Drift after the intensities of the eddy bottom current begin to decrease.

(3) Where is the region for sediment resuspension that might act as a potential source of the Agulhas Drift?

Erosion along the northeastern flank of the Agulhas Plateau is an important sediment source for the Agulhas Drift. Under the conditions of active current of AABW during eddy events, the strong resuspension can take place in this region. The suspensions increase with finer sediment grain sizes.

Outlook

For the future projects, long term hydrographic and hydrodynamic observations are required, so that the features of these eddies revealed in our simulations can be confirmed. Drilling data are also necessary to prove the potential grain size range suggested by the numerical experiments.

Moreover, only the suspended sediment concentrations are observed in this study. The sedimentation rate should be considered in the further studies. Additionally, cohesive finer sediment (i.e. clay) should be taken into account to further examine the whole grain size spectrum of the Agulhas Drift. As we have known, the erosion along the northeast flank of the Agulhas Plateau is an import source for the Agulhas Drift. A subsequent numerical study could be carried out to observe the sediment source at the Agulhas Plateau.

Additionally, the ROMS with sediment transport model can be applied in the other region to obtain further understanding of other sediment drifts. For instance, it could be used to simulate the sediment transport patterns at the Drift 7, west of the Antarctic Peninsula. The grain size spectrum of the Drift 7 is known.

The model results for this region could be compared with sediment transport patterns simulated in this thesis in order to obtain further information about the components of the Agulhas Drift.

Bibliography

Ariathurai, R., and K. Arulanandan (1978), Erosion rates of cohesive soils, *Journal of Hydraulic Division ASCE*, *104*(2), 279–282.

Beckmann, A., and D. Haidvogel (1993), Numerical simulation of flow around a tall isolated seamount. part i: Problem formulation and model accuracy, *J. Phys. Oceanogr.*, *23*(8), 1736–1753, doi:10.1175/1520-0485(1993)023<1736:NSOFAA>2.0.CO;2.

Ben-Avraham, Z., T. Niemi, and C. Hartnady (1994), Mid-tertiary changes in deep ocean circulation patterns in the natal valley and transkei basin, southwest indian ocean, *Earth and Planetary Science Letters*, *121*, 639–646.

Biastoch, A., C. Böing, and J. Lutjeharms (2008a), Agulhas leakage dynamics affects decadal variability in atlantic overturning circulation, *Nature*, *456*, 489–492, doi:10.1038/nature07426.

Biastoch, A., J. Lutjeharms, C. Böing, and M. Scheinert (2008b), Mesoscale perturbations control inter-ocean exchange south of africa, *Geophys. Res. Lett.*, *35*(20), L20602, doi:10.1029/2008GL035132.

Blaas, M., C. Dong, P. Marchesiello, J. McWilliams, and K. Stolzenbach (2007), Sediment-transport modeling on southern californian shelves: A ROMS case study, *Continental Shelf Research*, *27*(6), 832–853, doi:10.1016/j.csr.2006.12.003.

Blayo, E., and L. Debreu (1999), Adaptive mesh refinement for finite difference ocean models: first experiments, *J. Phys. Oceanogr.*, *29*, 1239–1250.

Bleck, R., and D. Boudra (1986), Wind-driven spin-up in eddy-resolving ocean models formulated in isopycnic and isobaric coordinates, *J. Geophys. Res.*, *91*((C6)), 7611–7621.

Boebel, O., and C. Barron (2003), A comparison of in-situ float velocities with altimeter derived geostrophic velocities, *Deep-Sea Res. II*, *50*(19), 119–139, doi:10.1016/S0967-0645(02)00381-8.

Boebel, O., C. Barron, J. Lutjeharm, W. Zenkd, and C. Barron (2003), Path and variability of the agulhas return current, *Deep-Sea Res. II*, *50*(1), 35–56, doi:10.1016/S0967-0645(02)00377-6.

Boswell, S., and D. Smythe-Wright (2002), The tracer signature of antarctic bottom water and its spread in the southwest indian ocean: Part i–cfc-derived translation rate and topographic control around the southwest indian ridge and the conrad rise, *Deep-Sea Res. I*, *49*(3), 555–573, doi:10.1016/S0967-0637(01)00066-8.

Boswell, S., D. Smythe-Wright, S. Holley, and D. Kirkwood (2002), The tracer signature of antarctic bottom water and its spread in the southwest indian ocean: Part ii–dissolution fluxes of dissolved silicate and their impact on its use as a chemical tracer, *Deep-Sea Res. I*, *49*(3), 575–590, doi:10.1016/S0967-0637(01)00067-X.

Bröcker, W. (1987), The biggest chill. natural history magazine, *Natural History Magazine*, *97*, 74–82.

Bryden, H., L. Beal, and L. Duncan (2005), Structure and transport of the agulhas current and its temporal variability, *Journal of Oceanography*, *61*(3), 479–492, doi:10.1007/s10872-005-0057-8.

Budgell, W. (2005), Numerical simulation of ice-ocean variability in the barents sea region, *Ocean Dynamics*, *55*, 370–387, doi:10.1007/s10236-005-0008-3.

Camden-Smith, F., L.-A. Perrins, R. Dingle, and G. Brundrit (1981), A preliminary report on long-term bottom-current measurements and sediment transport/erosion in the agulhas passage, southwest indian ocean, *Marine Geology*, *39*(3-4), M81–M88, doi:10.1016/0025-3227(81)90069-4.

Casal, T., L. Beal, and R. Lumpkin (2006), A north atlantic deep-water eddy in the agulhas current system, *Deep-Sea Res. I*, *53*(10), 1718–1728, doi:10.1016/j.dsr.2006.08.007.

Chassignet, E., and D. Boudra (1988), Dynamics of agulhas retroflection and ring formation in a numerical model. part ii. energetics and ring formation, *J. Phys. Oceanogr.*, *18*(2), 304–319, doi:10.1175/1520-0485(1988)018<0304:DOARAR>2.0.CO;2.

da Silva, A., C. Young, and S. Levitus (1994), Atlas of surface marine data 1994, *Tech. rep.*, NOAA Atlas NESDIS, Washington DC. USA.

de Ruijter, W., A. Biastoch, S. Drijfhout, J. Lutjeharms, R. Matano, T. Pichevin, P. van Leeuwen, and W. Weijer (1999), Indian-atlantic interocean exchange: Dynamics, estimation and impact, *J. Geophys. Res.*, *104*(C9), 20,885–20,910.

Debreu, L., C. Vouland, and E. Blayo (2008), Agrif: Adaptive grid refinement in fortran, *Computers and Geosciences*, *34*(1), 8–13, doi:10.1016/j.cageo.2007.01.009.

Dengler, M., F. Schott, C. Eden, P. Brandt, J. Fischer, and R. Zantopp (2004), Break-up of the atlantic deep western boundary current into eddies at 8° S, *Nature*, *432*, 1018–1020, doi:10.1038/nature03134.

Dingle, R., and F. Camden-Smith (1979), Acoustic stratigraphy and current-generated bedforms in deep ocean basins off southeastern africa, *Marine Geol-*

ogy, *33*(3-4), 239–260, doi:10.1016/0025-3227(79)90083-5.

Dingle, R., and S. Robson (1985), Slumps, canyons and related features on the continental margin off east london, se africa (sw indian ocean), *Marine Geology*, *67*(1-2), 37–54, doi:10.1016/0025-3227(85)90147-1.

Donners, J., and S. Drijfhout (2004), The lagrangian view of south atlantic interocean exchange in a global ocean model compared with inverse model results, *J. Phys. Oceanogr.*, *34*(5), 1019–1035, doi:10.1175/1520-0485(2004)034<1019:TLVOSA>2.0.CO;2.

Drijfhout, S., and W. Hazeleger (2007), Detecting atlantic moc changes in an ensemble of climate change simulations, *J. Climate*, *20*(8), 1571–1582, doi:10.1175/JCLI4104.1.

Ducet, N., P. L. Traon, and G. Reverdin (2000), Global high-resolution mapping of ocean circulation from topex/poseidon and ers-1 and -2, *J. Geophys. Res.*, *105*(C8), 19,477–19,498.

Duncombe Rae, C. (1991), Agulhas retroflection rings in the south atlantic ocean: an overview, *South African Journal of Marine Science*, *11*, 327–344.

Ezer, T., and G. Weatherly (1991), Small-scale spatial structure and long-term variability of near-bottom layers in the hebble area, *Marine Geology*, *99*(3-4), 319–328, doi:10.1016/0025-3227(91)90047-8.

Faugères, J.-C., M. Mézerais, and D. Stow (1993), Contourite drift types and their distribution in the north and south atlantic ocean basins, *Sedimentary Geology*, *82*(1-4), 189–203, doi:10.1016/0037-0738(93)90121-K.

Faugères, J.-C., D. Stow, P. Imbert, and A. Viana (1999), Seismic features diagnostic of contourite drifts, *Marine Geology*, *162*(1), 1–38, doi:10.1016/S0025-3227(99)00068-7.

Fennel, K., J. Wilkin, J. Levin, J. Moisan, J. OŔeilly, and D. Haidvogel (2006), Nitrogen cycling in the middle atlantic bight: Results from a three-dimensional model and implications for the north atlantic nitrogen budget, *Global Biogeochemical Cycles*, *162*(1), GB3007, doi:10.1029/2005GB002456.

Ganopolski, A., V. Petoukhov, S. Rahmstorf, V. Brovkin, M. Claussen, A. Eliseev, and C. Kubatzki (2001), Climber-2: a climate system model of intermediate complexity. part ii: model sensitivity, *Journal Climate Dynamics*, *17*(10), 735–751, doi:10.1007/s003820000144.

Garcia, M., and G. Parker (1991), Entrainment of bed sediment into suspension, *Journal of Hydraulic Engineering*, *117*(4), 414–435, doi:10.1061/(ASCE)0733-9429(1991)117:4(414).

Gordon, A. (1985), Indian-atlantic transfer of thermocline water at the agulhas retroflection, *Science*, *227*(4690), 1030–1033, doi:10.1126/science.227.4690.1030.

Gordon, A. (1986), Interocean exchange of thermocline water, *J. Geophys. Res.*, *91*(C4), 5037–5046.

Gordon, A. (1991), The role of thermohaline circulation in global climate change, in *Lamont-Doherty Geological Observatory 1990 & 1991 Report*, pp. 44–51, Lamont-Doherty Geological Observatory of Columbia University, Palisades, New York.

Gordon, A. (2003), Oceanography: The brawniest retroflection, *Nature*, *421*, 904–905, doi:10.1038/421904a.

Gross, T., and W. Dade (1991), Suspended sediment storm modeling, *Marine Geology*, *99*(3-4), 343–360, doi:10.1016/0025-3227(91)90049-A.

Haidvogel, D., H. Arango, K. Hedstrom, A. Beckmannb, P. Malanotte-Rizzolic, and A. Shchepetkind (2000), Model evaluation experiments in the north at-

lantic basin: simulations in nonlinear terrain-following coordinates, *Dynam. Atmos. Oceans*, *32*(3-4), 239–281, doi:10.1016/S0377-0265(00)00049-X.

Heezen, B., and C. Hollister (1964), Deep sea current evidence from abyssal sediments, *Marine Geology*, *1*, 141–174.

Heezen, B., and C. Hollister (Eds.) (1971), *The Face of the Deep*, 659 pp., Oxford University Press, New York.

Hollister, C. (1993), The concept of deep-sea contourites, *Sedimentary Geology*, *82*, 5–11.

Hollister, C., and I. McCave (1984), Sedimentation under deep-sea storms, *Nature*, *309*, 220–225, doi:10.1038/309220a0.

Hollister, C., and A. Nowell (1991a), Prologue: Abyssal storms as a global geologic process, *Marine Geology*, *99*(3-4), 275–280, doi:10.1016/0025-3227(91)90044-5.

Hollister, C., and A. Nowell (1991b), Hebble epilogue, *Marine Geology*, *99*(3-4), 445–460, doi:10.1016/0025-3227(91)90055-9.

Jordi, A., and D.-P. Wang (2009), Mean dynamic topography and eddy kinetic energy in the mediterranean sea: Comparison between altimetry and a 1/16 degree ocean circulation model, *Ocean Modelling*, *29*(2), 137–146, doi:10.1016/j.ocemod.2009.04.001.

Karakas, G., N. Nowald, M. Blaas, P. Marchesiello, S. Frickenhaus, and R. Schlitzer (2006), High-resolution modeling of sediment erosion and particle transport across the northwest african shelf, *J. Geophys. Res.*, *111*(C06025), doi:10.1029/2005JC003296.

Keylock, C., R. Hardy, D. Parsons, R. Ferguson, S. Lane, and K. Richards (2005), The theoretical foundations and potential for large-eddy simulation (les) in fluvial geomorphic and sedimentological research, *Earth-Science Reviews*, *71*(3-4), doi:10.1016/j.earscirev.2005.03.001.

Kliem, N., and J. Pietrzak (1999), On the pressure gradient error in sigma coordinate ocean models: A comparison with a laboratory experiment, *J. Geophys. Res.*, *104*(C12), 29,781–29,799.

Knorr, G., and G. Lohmann (2003), Southern ocean origin for the resumption of atlantic thermohaline circulation during deglaciation, *Nature*, *424*, 532–536, doi:10.1038/nature01855.

Kontar, E., and A. Sokov (1994), A benthic storm in the northeastern tropical pacific over the fields of manganese nodules, *Deep-Sea Res. I*, *41*(7), 1069–1089, doi:10.1016/0967-0637(94)90019-1.

Locarnini, R., A. Mishonov, J. Antonov, T. Boyer, and H. Garcia (2006), World ocean atlas 2005, *Tech. rep.*, NOAA Atlas NESDIS, Washington DC. USA.

Lumpkin, R., and K. Speer (2007), Global ocean meridional overturning, *J. Phys. Oceanogr.*, *37*, 2550–2562, doi:10.1175/JPO3130.1.

Lutjeharms, J. (1996), The exchange of water between the south indian and south atlantic oceans, in *The South Atlantic: Present and Past Circulation*, edited by G. Wefer, W. Berger, G. Siedler, and D. Webb, pp. 125–162, Springer-Verlag, Berlin, Heidelberg.

Lutjeharms, J. (Ed.) (2006), *The Agulhas Current*, Springer, Berlin.

Lutjeharms, J., and A. Gordon (1987), Shedding of an agulhas ring observed at sea, *Nature*, *325*, 138–140, doi:10.1038/325138a0.

Lutjeharms, J., and R. van Ballegooyen (1988), The retroflection of the agulhas current, *J. Phys. Oceanogr.*, *18*(11), 1570–1583.

Lutjeharms, J., F. Shillington, and C. Duncombe-Rae (1991), Observations of extreme upwelling filaments in the southeast atlantic ocean, *Science*, *253*(5021), 774–776, doi:10.1126/science.253.5021.774.

Lutjeharms, J., P. Penven, and C. Roy (2003), Modelling the shear edge eddies of the southern agulhas current, *Continental Shelf Research*, *23*(11-13), 1099–1115, doi:10.1016/S0278-4343(03)00106-7.

Mantyla, A., and J. Reid (1995), On the origins of deep and bottom waters of the indian ocean, *J. Geophys. Res.*, *100*(C2), 2417–2439.

Marchesiello, P., J. McWilliams, and A. Shchepetkin (2001), Open boundary conditions for long-term integration of regional oceanic models, *Ocean Modelling*, *3*(1-2), 1–20, doi:10.1016/S1463-5003(00)00013-5.

Martínez-Méndez, G., R. Zahn, I. R. Hall, L. D. Pena, and I. Cacho (2008), 345,000-year-long multi-proxy records off south africa document variable contributions of northern versus southern component water to the deep south atlantic, *Earth and Planetary Science Letters*, *267*(1-2), 309–321, doi:10.1016/j.epsl.2007.11.050.

Mellor, G., S. Häkkinen, T. Ezer, and R. Patchen (2002), A generalization of a sigma coordinate ocean model and an intercomparison of model vertical grids, in *Ocean Forecasting: Conceptual Basis and Applications*, edited by N. Pinardi and J. Woods, pp. 55–72, Springer, Berlin, Germany.

Naeije, M., K. Wakker, R. Scharroo, and B. Ambrosius (1992), Observation of mesoscale ocean currents from GEOSAT altimeter data, *ISPRS Journal of Photogrammetry and Remote Sensing*, *47*(5-6), 347–368, doi:10.1016/0924-2716(92)90038-B.

Niemi, T., Z. Ben-Avraham, C. Hartnady, and M. Reznikov (2000), Post-eocene seismic stratigraphy of the deep ocean basin adjacent to the southeast african continental margin: a record of geostrophic bottom current systems, *Marine Geology*, *162*(2-4), 237–258, doi:10.1016/S0025-3227(99)00062-6.

Ogston, A., J. Guerra, and R. Sternberg (2004), Interannual variability of nearbed

sediment flux on the eel river shelf, northern california, *Continental Shelf Research*, *24*(1), 117–136, doi:10.1016/j.csr.2003.08.007.

Olson, D., and R. Evans (1986), Rings of the agulhas current, *Deep Sea Research Part A*, *33*(1), 27–42, doi:10.1016/0198-0149(86)90106-8.

Peeters, F. J. C., R. Acheson, G.-J. A. Brummer, W. P. M. de Ruijter, R. R. Schneider, G. M. Ganssen, E. Ufkes, and D. Kroon (2004), Vigorous exchange between the indian and atlantic oceans at the end of the past five glacial periods, *Nature*, *430*, 661–665, doi:10.1038/nature02785.

Penven, P., J. Lutjeharms, P. Marchesiello, C. Roy, and S. Weeks (2001), Generation of cyclonic eddies by the agulhas current in the lee of the agulhas bank, *Geophys. Res. Lett.*, *28*(6), 1055–1058.

Penven, P., J. Lutjeharms, and P. Florenchie (2006a), Madagascar: A pacemaker for the agulhas current system?, *Geophys. Res. Lett.*, *33*, L17609, doi:10.1029/2006GL026854.

Penven, P., P. Marchesiello, and J. McWilliams (2006b), Evaluation and application of the roms 1-way embedding procedure to the central california upwelling system, *Ocean Modelling*, *12*(1-2), 157–187, doi:10.1016/j.ocemod.2005.05.002.

Penven, P., P. Marchesiello, L. Debreu, and J. Lefèvre (2008), Software tools for pre- and post-processing of oceanic regional simulations, *Environmental Modelling and Software*, *23*(5), 660–662, doi:10.1016/j.envsoft.2007.07.004.

Powell, T., C. Lewis, E. Curchitser, D. Haidvogel, A. Hermann, and E. Dobbins (2006), Results from a three-dimensional, nested biological-physical model of the california current system and comparisons with statistics from satellite imagery, *J. Geophys. Res.*, *111*, C07018, doi:10.1029/2004JC002506.

Pudsey, C. (2001a), Data report: Grain-size data, sites 1095, 1096, and 1101, antarctic peninsula continental rise, in *Proceedings of the Ocean Drilling Pro-*

gram Scientific Results, vol. 178, edited by P. Barker and C. Pudsey, Ocean Drilling Program, Texas A&M University, College Station, TX, U.S.A, doi: 10.2973/odp.proc.sr.178.213.2001.

Pudsey, C. (2001b), Neogene record of antarctic peninsula glaciation in continental rise sediments: Odp leg 178, site 1095, in *Proceedings of the Ocean Drilling Program Scientific Results*, vol. 178, edited by P. Barker and C. Pudsey, Ocean Drilling Program, Texas A&M University, College Station, TX, U.S.A, doi: 10.2973/odp.proc.sr.178.214.2001.

Quartly, G., and M. Srokosz (1993), Seasonal variations in the region of the agulhas retroflection: Studies with geosat and fram, *Journal of Physical Oceanography*, *23*(9), 2107–2124.

Rahmstorf, S. (1995), Bifurcations of the atlantic thermohaline circulation in response to changes in the hydrological cycle, *Nature*, *378*, 145–149, doi:10.1038/378145a0.

Rahmstorf, S. (2002), Ocean circulation and climate during the past 120,000 years, *Nature*, *419*, 207–214, doi:10.1038/nature01090.

Rau, A. J., J. Rogers, J. R. E. Lutjeharms, J. Giraudeau, J. A. Lee-Thorp, M. T. Chen, and C. Waelbroeck (2002), A 450-kyr record of hydrological conditions on the western agulhas bank slope, south of africa, *Marine Geology*, *180*(1-4), 183–201, doi:10.1016/S0025-3227(01)00213-.

Rebesco, M. (2005), Contourites, in *Encyclopedia of Geology*, edited by R. Selley, L. Cocks, and I. Plimer, pp. 513–527, Elsevier, Oxford.

Rebesco, M., and D. Stow (2001), Seismic expression of contourites and related deposits: a preface, *Marine Geophysical Researches*, *22*, 303–308.

Rebesco, M., C. Pudsey, M. Canals, A. Camerlenghi, P. Barker, F. Estrada, and A. Giorgetti (2002), Sediment drifts and deep-sea channel systems, antarctic

peninsula pacific margin, in *Deep-Water Conturite Systems: Modern Drifts and Ancient Series, Seismic and Sedimentary Characteristics*, edited by D. Stow, J.-C. Faugères, J. Howe, C. Pudsey, and A. Viana, pp. 353–371, Geological Society, London, doi:10.1144/GSL.MEM.2002.022.01.25.

Rebesco, M., A. Camerlenghi, and A. V. Loon (2008), Contourite research: a field in full development, in *Contourites, Developments in Sedimentology*, edited by M. Rebesco, A. Camerlenghi, and A. V. Loon, pp. 3–10, Elsevier.

Richardson, P. (2008), On the history of meridional overturning circulation schematic diagrams, *Progress in Oceanography*, *76*(4), 466–486, doi:10.1016/j.pocean.2008.01.005.

Rio, M.-H., and F. Hernandez (2004), A mean dynamic topography computed over the world ocean from altimetry, in situ measurements, and a geoid model, *J. Geophys. Res.*, *109*, C12032, doi:10.1029/2003JC002226.

Sarnthein, M., K. Winn, S. Jung, J.-C. Duplessy, L. Labeyrie, H. Erlenkeuser, and G. Ganssen (1994), Changes in east atlantic deepwater circulation over the last 30,000 years: eight time slice reconstructions, *Paleoceanography*, *9*(2), 209–267.

Schlüter, P., and G. Uenzelmann-Neben (2007), Seismostratigraphic analysis of the transkei basin: A history of deep sea current controlled sedimentation, *Marine Geology*, *240*(1-4), 99–111, doi:10.1016/j.margeo.2007.02.015.

Schlüter, P., and G. Uenzelmann-Neben (2008), Indications for bottom current activity since eocene times: The climate and ocean gateway archive of the transkei basin, south africa, *Global and Planetary Change*, *60*(3-4), 416–428, doi:10.1016/j.gloplacha.2007.07.002.

Schmitz, W. (1996a), On the world ocean circulation: Volume i, some global features/north atlantic circulation, *Technical report*, Woods Hole Oceanographic Institution.

Schmitz, W. (1996b), On the world ocean circulation: Volume ii, the pacific and indian oceans/a global update, *Technical report*, Woods Hole Oceanographic Institution.

Shanmugam, G. (Ed.) (2006), *Deep-Water Processes and Facies Models: Implications for Sandstone Petroleum*, Elsevier, Amsterdam.

Shanmugam, G. (2008), Deep-water bottom currents and their deposits, in *Contourites*, edited by M. Rebesco and A. Camerlenghi, pp. 59–81, Elsevier.

Shchepetkin, A., and J. McWilliams (2003), A method for computing horizontal pressure-gradient force in an oceanic model with a nonaligned vertical coordinate, *J. Geophys. Res.*, *108*(C3), 3090, doi:10.1029/2001JC001047.

Shchepetkin, A., and J. McWilliams (2005), The regional oceanic modeling system (ROMS): a split-explicit, free-surface, topography-following-coordinate oceanic model, *Ocean Modelling*, *9*(4), 347–404, doi:10.1016/j.ocemod.2004.08.002.

Siedler, G., J. Church, and J. Gould (Eds.) (2001), . *Ocean Circulation and Climate: Observing and Modelling the Global Ocean*, 715 pp., Academic Press, New York.

Smith, W., and D. Sandwell (1997), Global sea floor topography from satellite altimetry and ship depth soundings, *Science*, *277*(5334), 1956–1962, doi:10.1126/science.277.5334.1956.

Song, Y. (1998), A general pressure gradient formulation for ocean models. part i: Scheme design and diagnostic analysis, *Mon. Weather Rev.*, *126*(12), 3213–3230, doi:10.1175/1520-0493(1998)126<3213:AGPGFF>2.0.CO;2.

Song, Y., and D. Haidvogel (1994), A semi-implicit ocean circulation model using a generalized topography-following coordinate system, *J. Comput. Phys.*, *115*(1), 228–244, doi:10.1006/jcph.1994.1189.

Soulsby, R. (1995), Bed shear stresses due to combined waves and currents, in *Advances in Coastal Morphodynamics*, edited by M. Stive, H. de Vriend, J. Fredsoe, L. Hamm, R. Soulsby, C.Tesson, and J. Winterwrep, pp. 4–20, Delft Hydraulics, Netherlands.

Soulsby, R. (Ed.) (1997), *Dynamics of Marine Sands. A manual for practical applications*, Thomas Telford Publications, London, U.K.

Soulsby, R., and R. Whitehouse (1997), Threshold of sediment motion in coastal environments, in *Pacific Coasts and Ports 1997, 13th Australasian Coastal and Engineering Conference and 6th Australasian Port and Harbour Conference*, pp. 149–154, HR Wallingford, Oxon, Christchurch, New Zealand.

Stow, D., and M. Mayall (2000), Deep-water sedimentary systems: New models for the 21st century, *Marine and Petroleum Geology*, *17*(2), 125–135, doi:10.1016/S0264-8172(99)00064-1.

Stow, D., J.-C. Faugères, J. Howe, C. Pudsey, and A. Viana (2002), Bottom currents, contourites and deep-sea sediment drifts: current state-of-the-art, in *Deep-water contourite systems: modern drifts and ancient series, seismic and sedimentary characteristics*, edited by D. Stow, J.-C. Faugères, J. Howe, and C. Pudsey, pp. 7–20, Geological Society of London, London, UK.

Stramma, L., and J. Lutjeharms (1997), The flow field of the subtropical gyre of the south indian ocea, *J. Geophys. Res.*, *102*(C3), 5513–5530.

Sudre, J., and R. Morrow (2007), Global surface currents: a high-resolution product for investigating ocean dynamics, *Ocean Dynamics*, *5829*(2), 101–118, doi:10.1007/s10236-008-0134-9.

Toole, J., and B. Warren (1993), A hydrographic section across the subtropical south indian ocean, *Deep-Sea Res. I*, *40*(10), 1973–2019, doi:10.1016/0967-0637(93)90042-2.

Uenzelmann-Neben, G. (2002), Contourites on the agulhas plateau, sw indian ocean: Indications for the evolutions of currents since paleogene times, in *Deep-water Contourite Systems : Modern Drifts and Ancient Series, Seismic and Sedimentary Characteristics*, vol. 22, edited by D. Stow, J.-C. Faugères, J. Howe, C. Pudsey, and A. Viana, pp. 271–288, Memoirs of the Geological Society of London.

van Aken, H. (2000), The hydrography of the mid-latitude northeast atlantic ocean ii: The intermediate water masses, *Deep-Sea Res. I*, *47*(5), 789–824, doi: 10.1016/S0967-0637(99)00112-0.

van Aken, H., H. Ridderinkhof, and W. de Ruijter (2004), North atlantic deep water in the south-western indian ocean, *Deep-Sea Res. I*, *51*(6), 755–766, doi: 10.1016/j.dsr.2004.01.008.

Vellinga, M., and R. Wood (2002), Global climatic impacts of a collapse of the atlantic thermohaline circulation, *Clim. Change*, *54*(3), 251–267, doi:10.1023/A:1016168827653.

Warner, J., C. Sherwood, H. Arangob, and R. Signell (2005), Performance of four turbulence closure models implemented using a generic length scale method, *Ocean Modelling*, *8*(1-2), 81–113, doi:10.1016/j.ocemod.2003.12.003.

Warner, J., C. Sherwood, R. Signell, C. Harris, and H. Arango (2008a), Development of a three-dimensional, regional, coupled wave, current, and sediment-transport model, *Computers and Geosciences*, *34*(10), 1284–1306, doi:10.1016/j.cageo.2008.02.012.

Warner, J., B. Butman, and P. Dalyander (2008b), Storm-driven sediment transport in massachusetts bay, *Continental Shelf Research*, *28*(2), 257–282, doi: 10.1016/j.csr.2007.08.008.

Washburn, L., M. Swenson, J. Largier, P. Kosro, and S. Ramp (1993), Cross-shelf

sediment transport by an anticyclonic eddy off northern california, *Science*, *261*(5128), 1560–1564, doi:10.1126/science.261.5128.1560.

Weatherly, G., M. Arhan, H. Mercier, and W. S. Jr. (2002), Evidence of abyssal eddies in the brazil basin, *J. Geophys. Res.*, *107*(C4), 3027, doi:10.1029/2000JC000648.

Webb, D., A. Coward, B. de Cuevas, and C. Gwilliam (1997a), A multiprocessor ocean general circulation model using message passing, *Journal of Atmospheric and Oceanic Technology*, *14*(1), 175–183, doi:10.1175/1520-0426(1997)014<0175:AMOGCM>2.0.CO;2.

Webb, D., B. de Cuevas, and A. Coward (1998), The first main run of the occam global ocean model, in *internal report of James Rennell Div.*, Southampton Oceanog. Cent., Southampton, England, U.K.

Webb, R., D. Rind, S. Lehman, R. Healy, and D. Sigman (1997b), Influence of ocean heat transport on the climate of the last glacial maximum, *Nature*, *385*, 695 – 699, doi:doi:10.1038/385695a0.

Wentworth, C. (1922), A scale of grade and class terms for clastic sediments, *The Journal of Geology*, *30*, 377–392.

Wolf-Welling, T., T. Mörz, C.-D. Hillenbrand, C. Pudsey, and E. Cowan (2001), Data report: Bulk sediment parameters (caco3, toc, and $\geq 63\,\mu$m of sites 1095, 1096, and 1101, and coarse-fraction analysis of site 1095 (odp leg 178, western antarctic peninsula), in *Proceedings of the Ocean Drilling Program Scientific Results*, vol. 178, edited by P. Barker, C. Pudsey, C.-D. Hillenbrand, and C. Pudsey, Ocean Drilling Program, Texas A&M University, College Station, TX, U.S.A, doi:110.2973/odp.proc.sr.178.223.2001.

Wust, G. (1936), Schichtung und zirkulation des atlantischen oceans: Schnitte und karten von temperatur, salzgehalt und dichte, *Wiss. Ergeb. Dtsch. Atlant. Exped. 6*, Atlas.

You, Y., J. Lutjeharms, O. Boebel, and W. de Ruijter (2003), Quantification of the interocean exchange of intermediate water masses around southern africa, *Deep-Sea Res. II*, *50*(1), 197–228, doi:10.1016/S0967-0645(02)00384-3.

A

Root Mean Square Error

The root mean square error (RMSE) is a frequently-used measure of the differences between values predicted by a model or an estimator and the values actually observed from the phenomenon being modeled or estimated. RMSE is used in this thesis in order to justify the simulation approach and the improvement of the child model performance.

Written mathematically, root mean square error is

$$\mathrm{RMSE} = \sqrt{\frac{\sum_{i=1}^{n}(o_i - s_i)^2}{n}}$$

Where o_i is observation data, s_i is simulated values from the model, and n is the size of the sample.

B

Eddy Kinetic Energy

The eddy kinetic energy (EKE) refers to the energy associated with the turbulent part of the flow of a fluid. It is the kinetic energy of that component of fluid flow which represents a departure from the average kinetic energy of the fluid.

In this thesis sea surface hight (SSH) is used to obtain the EKE. Altimetric studies of the ocean turbulent eddy field usually assume isotropy. The resulting EKE is then given by the square of the cross-track geostrophic velocity component as:

$$\mathrm{EKE} = \frac{1}{2}\left(\left\langle {U'_{\mathrm{g}}}^2 \right\rangle + \left\langle {V'_{\mathrm{g}}}^2 \right\rangle\right)$$

$$U'_{\mathrm{g}} = -\frac{g}{f}\frac{\Delta\xi'}{\Delta y}$$

$$V'_{\mathrm{g}} = \frac{g}{f}\frac{\Delta\xi'}{\Delta x}$$

where U'_{g} and V'_{g} denote the zonal and meridional geostrophic velocity anomalies, ξ' is the SSH anomalies, f is the Coriolis parameter, g is the acceleration of gravity, x and y are the distances in longitude and latitude, respectively, and $\langle\,\rangle$ denotes the time average.

Acknowledgments

First and foremost, I want to thank my advisors, Prof. Dr. Heinrich Miller, Prof. Dr. Katrin Huhn and Dr. Gabriele Uenzelmann–Neben, for the opportunity to work on such a challenging topic. Together they make sure that I stay on the right track with this thesis and finally come to an end. Thank you for numerous discussions that lead to considerable improvements of the thesis.

Many thanks are addressed to my colleagues at the Geography Department of the Alfred Wegener Institute for Polar and Marine Research and at the Ocean Modeling Group in the University of Bremen. They always have an open ear for me and my problems, are always good for a relaxing chat in between.

Thanks also to the graduate school GLOMAR. It provided funding for a research residence at the University of Cape Town. I want to thank Prof. Dierk Hebbeln, Uta Brathauer, Carmen Murken and Gabi Ratmeyer for their support.

Furthermore, I want to thank Prof. Dr. Johann Lutjeharms, Dr. Gökay Karakas and Dr. Pierrick Penven for their help in understanding ROMS and the regional oceanography as well as fruitful discussions.

Finally, I would like to thank my family and my friends for their continuous encouragements.